TINY PIEZOELECTRIC ENERGY-HARVESTING CMOS CHARGER

A Dissertation
Presented to
The Academic Faculty

by

Siyu Yang

In Partial Fulfillment
of the Requirements for the Degree
Doctor of Philosophy in the
School of Electrical and Computer Engineering

Georgia Institute of Technology
December 2020

TINY PIEZOELECTRIC ENERGY-HARVESTING CMOS CHARGER

Approved by:

Dr. Gabriel A. Rincón-Mora, Advisor
School of Electrical and Computer Engineering
Georgia Institute of Technology

Dr. Deepakraj Divan
School of Electrical and Computer Engineering
Georgia Institute of Technology

Dr. William D. Hunt
School of Electrical and Computer Engineering
Georgia Institute of Technology

Dr. Josephine Yu
School of Mathematics
Georgia Institute of Technology

Dr. Farrokh Ayazi
School of Electrical and Computer Engineering
Georgia Institute of Technology

Date Approved: October 15, 2020

[To 2020]

ACKNOWLEDGEMENTS

First of all, I would like to thank my advisor, Dr. Gabriel A. Rincón-Mora, for his insightful guidance, timely encouragement, and unwavering support throughout my program. He has taught me, in addition to circuit designs, leadership, attention to detail, and professionalism that I will make use of throughout the rest of my career.

I would like to thank my parents, Dr. Ning Yang and Shuhui Jin, for their unconditional love and support throughout my life, and for their inspiration that helped me achieve my goal of pursuing a Ph. D degree.

I would like to thank Texas Instruments, for financially supporting my research, and giving me an internship opportunity for my first experience in the industry. I would like to thank my mentors at Texas Instruments, Dr. Orlando Lazaro and Dr. Andres Blanco, for their support and advice during my program.

I would like to thank all my colleagues at the Georgia Tech Analog, Power, and Energy ICs Labs, for their support, understanding, encouragement, and the countless discussions.

Lastly, I would like to my fiancée, Wanqing Xin, for her love, support, and perseverance throughout my Ph. D program, without which none of my accomplishment would have been possible.

TABLE OF CONTENTS

LIST OF TABLES

LIST OF FIGURES

SUMMARY

Wireless microsystems have widespread applications in smart homes, industrial automation, self-driving vehicles and traffic control, and healthcare that save money, energy, and lives. While the demand for their functionality keeps increasing, their footprint requirement is becoming stringent. With the lack of breakthrough in battery technology in recent years, the onboard battery drains quickly, and needs recharging or replacing frequently, which increases cost and, in some cases, is dangerous or even impossible. Fortunately, piezoelectric transducer can harvest ambient kinect energy from vibration to indefinitely replenish the tiny on-board battery and output moderate power. However, piezoelectric transducers energy harvesting chargers face challenges that comes with the miniaturization. With small transducers, the power is reduced, and the charger would need to be optimized to output the maximum power possible to power the microsystem. It would also require a maximum power-point controller that can adjust to the environment and output the maximum power at all times. The miniaturized charger is under strict breakdown limits. The objective of this research is to study, evaluate, design, build, test, and assess energy-harvesting CMOS battery chargers that draw and output the most power possible from ambient motion with centimeter-scale piezoelectric transducers that fit on wireless microsensors.

Such small transducers draw little power, the vibration strength can vary, and the CMOS chargers are lossy. Because small transducers have low electromechanical coupling, raising drawn power by pre-charging their parasitic capacitance, which further

damps the transducer, is possible. That is why in the state of the art, synchronous discharges and recycling bridges can increase drawn power from the piezoelectric transducers.

Using switched-inductor to transfer power is efficient, and symmetrical pre-charging can draw more power from the transducer under the same breakdown limit, and losses less ohmic loss because of lower inductor current than the asymmetrical pre-charging in the state of the art. Measurement from the same power stage further validates the conclusion, as symmetrical pre-charge can draw 30–80% more power than the asymmetrical case. Symmetrical pre-charge schemes should be considered to power piezoelectric microsystems for longer lifetime and broader functionality.

On the other hand, direct transfers can allow the inductor to transfer more power than it carries. As a result, the transfer time, and more importantly, peak inductor current, are lower than the indirect counterpart, reducing ohmic loss. Depending on the input and output conditions, either direct–indirect transfers or indirect–direct transfers should be utilized to reduce ohmic loss. Direct transfers scheme can also achieve pre-charging. As a result, the symmetrical pre-charging with direct transfers is the best synchronous discharge charger.

Two piezoelectric chargers have been proposed, designed, fabricated, tested, and assessed. The prototypes also verify the theories that direct transfers losses up to 73% less ohmic loss than indirect transfers, and that symmetrical pre-charging can output more power than asymmetric pre-charging. The series switched-inductor bridge charger can output 6.8× more than what an ideal bridge can draw, and the recycling switched-inductor charger further increase that to 12×. Moreover, the recycling switched-inductor can output

76% of the theoretically maximum power a piezoelectric transducer can output, outperforming the state of the art.

With higher drawn power, less restraining breakdown limits, and lower losses, the proposed chargers output the highest power possible across a wide vibration strength range to expand functionality, prolong life, and widen application space of wireless microsensors.

CHAPTER 1. PIEZOELECTRIC-POWERED MICROSYSTEMS

1.1. **Wireless Microsystems**

1.1.1. Applications

Rapid advances in integrated circuits (IC), micro-electro-mechanical-system (MEMS), and wireless communications in the past half century have enabled wireless microsystems to become smaller while packing more functionality than ever imagined. Wireless microsystems embedded in homes, factories, bridges, vehicles, and human bodies can monitor their surrounding environment, process the data, and transmit to a center location to save money, energy, and lives [1]–[50]. They have had success in internet of things (IoT), biomedical implants, industry, and other fields of study that will enhance the quality of life.

1.1.1.A. Internet of Things

One of the most promising and fastest growing applications of the wireless microsystems is the IoT [2]–[19]. The integration of sensors/actuators, radio frequency identification (RFID) tags, and communication technologies serves as the foundation of IoT and explains how a variety of physical objects and devices around us can be associated to the Internet and allow these objects and devices to cooperate and communicate with one another to reach common goals. IoT was first termed in 1999 [5], and it is been defined as a dynamic global network infrastructure with self-configuring capabilities based on standard and interoperable communication protocols where physical and virtual 'Things' have identities, physical attributes, and virtual personalities and use intelligent interfaces, and are

seamlessly integrated into the information network. In the past decade, IoT has seen exponential growth due to its wide application in smart homes [6]–[10], health care [11]–[14], industry [15]–[18], and even smart cities [19].

Automated homes allow sensors placed at different locations inside a house and appliances to communicate through RFID or near field communication. The microsystems collect data, and either send them to other microsystems directly, or to a center location to process the data. The collected data then controls the various aspects of the house automatically, such as air conditioning, lighting, entertainment systems, ovens, and even wireless vacuum cleaners, as shown in Figure 1-1. It can also monitor the temperature, smoke, or toxic gas in the case of an emergency. The sensors on the doors and windows can also prevent break-ins. All of these are made available and economical if the sensors on microsystems can operate without access to wall outlet for years at a time, since some of the sensors are placed at inaccessible locations and it adds to the cost significantly if the battery needs replacing frequently.

Another emerging application for the IoT is in an industrial setting, such as manufacturing, food processing industry, environmental monitoring, and security surveillance [15]. Reference [16] details the locations and functions of sensors placed in farms, warehouses, trucks, supermarkets and farmers' markets, and consumers' fridges to make food supply chain faster, more economical, more efficient, and more environmentally friendly. The authors in [17] demonstrate that leveraging sensors monitoring the forests and the wireless networks surrounding it, the authorities can detect wildfire at the earliest possible stage and pinpoint the location of the fire to save an enormous amount of money and even lives.

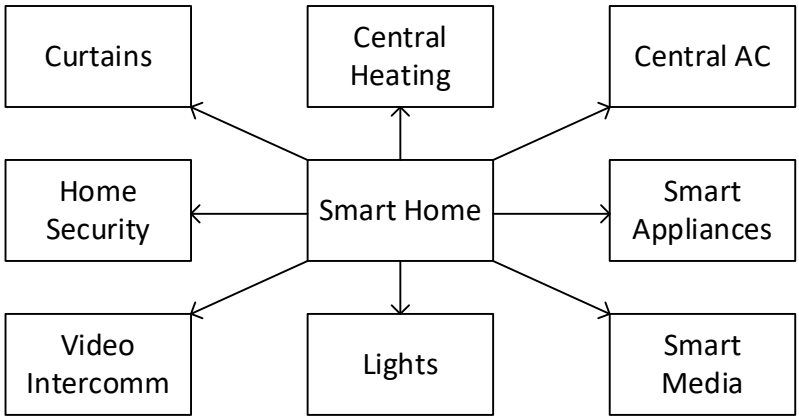

Figure 1-1. Typical configuration of Internet of Things in smart homes.

1.1.1.B. Biomedical Implants

Biomedical implants in human beings and wearable sensors for healthcare and wellness are also common applications for wireless microsystems [11]–[14], [20]–[32], and they require even more robustness and more intricate design. An integrated pacemaker has been proposed in [22]. As shown in Fig. 1-2, it senses and monitors the heartrate, and could provide stimulation when the heartrate is abnormal. Medically implanted immunoisolation devices [23] and drug delivery systems [24]–[26] have also been proposed, for potential cures for diabetes, and to accurately and timely deliver drugs directly into the blood. Wearable sensors can monitor electrocardiogram, blood pressure, respiration rate, blood glucose, and body movement to continuously monitor a person's health without interceding with normal daily life [29].

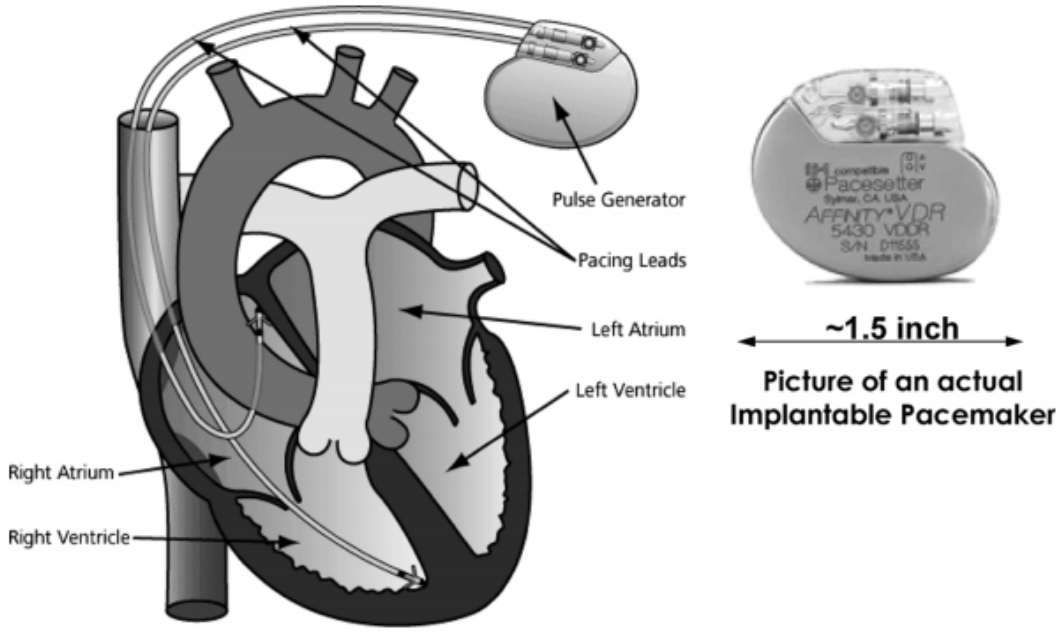

Figure 1-2. Implanted pacemaker [22].

1.1.1.C. Other Applications

Embedded microsystems in other applications have also drawn some research interests. Sensors embedded in vehicles can sense and monitor the tire pressure, gas level, and engine health. Self-driving cars require sensing the road, other vehicles, pedestrians, and traffic lights [33]. Different types of sensors therefore need to be places around the vehicle, shown in Fig. 1-3, with some of them out of reach of the car's main power line. In addition to the sensors on vehicles, microsystems placed on traffic lights and major highways can help smart cities manage traffic effectively and efficiently [36]. Microsystems can also be placed in large farms to monitor temperature, moist level, and plants' health to control the watering sequence and temperature [37]. Biomimetic micro-robots [38], can perform military surveillance and reconnaissance missions in critical situations or over dangerous and difficult to access terrain.

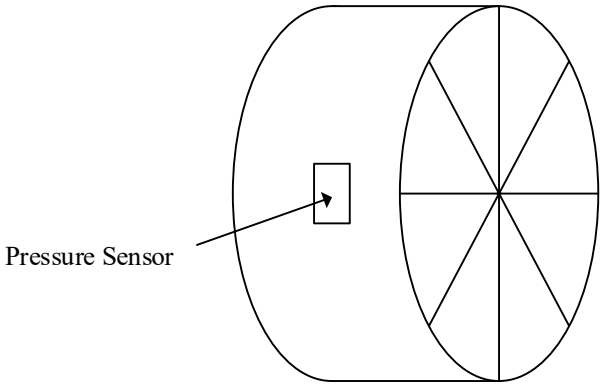

Figure 1-3. Embedded tire pressure sensor.

1.1.2. Requirements

The common challenges facing these applications comes with increasing demand for functionality with smaller footprint. In addition to the lack of breakthrough in battery technology since the lithium-ion became the mainstream choice in the early 2000s, the on board battery drains more quickly. Since most of the sensors are embedded or placed in difficult-to-access spots, replacing or recharging battery adds to the overall cost, and in some cases, i.e. medical implants, is dangerous and nearly impossible. Researchers have recently proposed to harvest ambient energy from the surroundings to constantly replenish the battery to prolong the lifetime of the microsystems.

The microsystems also require sensing, data processing, and transmitting functions, and each function has different voltage and power requirement. For example, a transmitter may require 1 mW to 1 W [51]–[53] over a few microseconds, and then remain idle until the next transmission is required. Sensors and processers can both consume microwatts, and they could also be duty cycled. However, ambient energy sources in a compact setting cannot provide 1 W to directly power the transmitter. Therefore, the battery is still

necessary to store the energy harvested from the ambient energy source when the microsystem is idle, and provide the instant power when it turns on. The ambient energy source only needs to provide the average power, which is much lower than the peak power, that a microsystem requires over a long time for it to be sustainable.

1.2. **Piezoelectric Transducers**

1.2.1. Kinetic Energy Harvesting

Kinetic energy in motion and vibration is very common in most of the aforementioned applications. A study in [54] lists the vibrations strength and frequency, which ranges from 1 Hz to 200 Hz. The finding has been summarized in Table 1-1. Recent advances in MEMS technology have allowed three different mechanisms to harvest energy to emerge: electrostatic, electromagnetic, and piezoelectric. All three mechanisms, while physically different, essentially exerts an electrical damping force in addition to its mechanical damping force (e.g. friction) that limits the vibration. The electrical damping force creates electrical charge, and the harvester collects the charge to replenish the battery.

Electrostatic transducers utilize variable capacitance devices to create and consume electrical charge or increase and decrease the energy held in the charge across a vibration cycle [55]–[62]. Electrostatic transducers are classified into two categories: voltage constraint or charge constraint. In the charge constraint case, shown Fig. 1-4(a), the capacitor is open-circuit when the capacitance of the transducer decreases. Since the charge now has nowhere to flow, the voltage across the capacitor increases, and the energy stored in the devices increases. In the voltage constraint case, the capacitor is clamped by a constant voltage source. As Fig. 1-4(b) shows, when external force moves the plates away

from each other and the capacitance of the transducer decreases, the electrical field across the capacitor falls, and charge flows from the capacitor plates into the voltage source. Another way to look at this is from the relationship between charge and voltage for a capacitor:

Table 1-1. Vibration sources with their acceleration and frequency [54].

Vibration Source	Acceleration [m/s^2]	Frequency [Hz]
Car engine compartment	12	200
Base of 3-axis machine tool	10	70
Blender casing	6.4	121
Clothes dryer	3.5	121
Person nervously tapping their heel	3	1
Car instrument panel	3	13
Door frame just after door closes	3	125
Small microwave oven	2.5	121
HVAC vents in office building	1.5	60
Windows next to a busy road	0.7	100
CD on notebook computer	0.6	75
Second story floor of busy office	0.2	100

$$q_{ES} = C_{ES}v_{ES}. \quad (1)$$

As capacitance C_{ES} drops, charge across the device q_{ES} drops with it because v_{ES} is clamped to a voltage source. Therefore, charge, and energy along with it, is flowing into the voltage source.

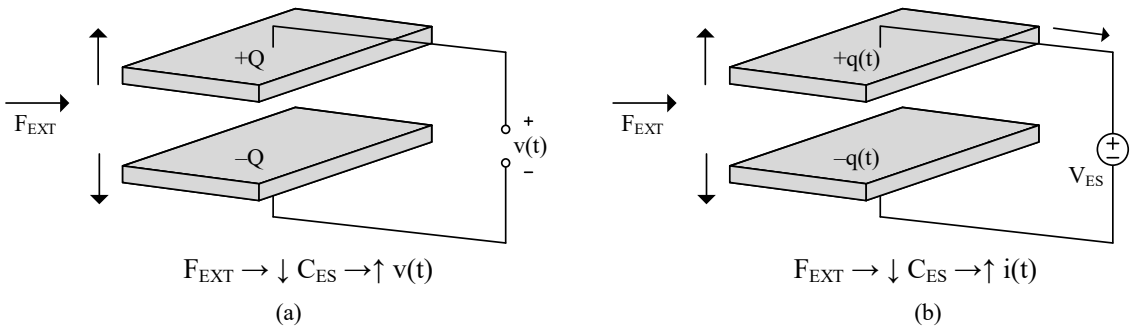

Figure 1-4. Electrostatic transduction concepts for (a) charge constraint case and (b) voltage constraint case.

For both the charge constraint transducers and voltage constraint devices, the critical parameter that sets the drawn power is the difference between the maximum capacitance and the minimum capacitance,

$$\Delta C_{ES} = C_{ES(MAX)} - C_{ES(MIN)}. \quad (2)$$

Although centimeter scale devices can achieve relatively high ΔC_{ES}, the reported integrated transducers all struggle to accomplish that [55]–[62]. Adding to the breakdown voltage constraint that integration brings, MEMS electrostatic transducers fail to output high enough power to support wireless microsystems.

Electromagnet transducers, on the other hand, contains a magnet and a coil. As either the magnet or the coil moves, an electromotive force that produces an electrical potential across the coil is induced [63]–[70]. Figure 1-5 shows three configurations of electromagnetic transducers [63]. The first one is a stationary coil around a moving magnet. As the external force moves the magnet towards the coil, the magnetic flux linking through the coil increases, thereby inducing a current that opposes the relative motion of the magnet and the coil, as explained by Lenz's Law. Conversely, when the magnet moves away from

the coil, the resulting voltage and the current change their polarity, which explains why the outputs of the electromagnetic transducers are alternative-current (AC) when vibrations are the energy source. The second and third configurations both consist of a rotating magnet on top of several stationary coils. The magnetic flux rotates with the magnet, and alternatingly cutting across different parts of the coil. The changing magnetic flux therefore induces alternating electromotive force.

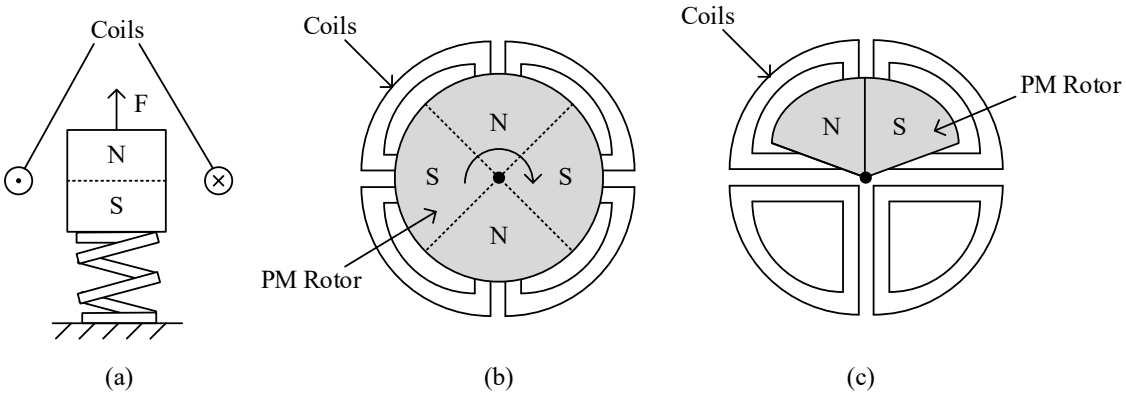

Figure 1-5. Three different types of electromagnetic transducers [63].

Electromagnetic transducers can produce enough power to supply the wireless microsensors. However, they contain at least two bulky components in the magnet and the coil, which makes it difficult to fit into a tiny wireless microsystem.

1.2.2. Piezoelectric transducers

Piezoelectric transducers, on the other hand, has a simpler physical design, with a cantilever, coated with piezoelectric material, and a mass, which vibrates under external force, at the end [71]–[98]. When unstrained, piezoelectric material is electrically neutral because, as Fig. 1-6 illustrates, positive and negative charge centers align and balance. The atomic arrangement is such, however, that charge centers shift away from one another

when the material strains [71]. This shift produces a surface potential that changes continuously with variations in mechanical deformation. The charger then collects the charges that is created with the surface potential change to replenish the battery. This mechanism to tap the energy created by the vibration directly without extra mechanical requirement (variable capacitor with high ΔC_{ES} for electrostatic) or addition component (magnet and coil for electromagnetic) makes piezoelectric transducers appealing for MEMS integration.

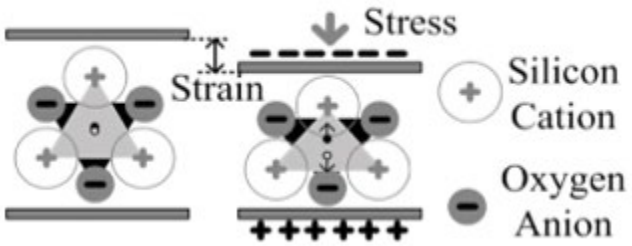

Figure 1-6. Piezoelectric material and its charge center with and without stress.

The typical piezoelectric transducer utilizes a flexible beam with one end fixed, the other end attached to a mass, and with piezoelectric material coated on the surfaces, as shown in Fig. 1-7. The most explored and used forms of piezoelectric material include single crystals (e.g. quartz), piezoelectric ceramic (e.g. lead zirconate titanate, or PVT), thin films (e.g. zinc oxide), and polymeric (e.g. polyvinylidene fluoride, or PVDF) [72] – [98]. Most of these materials have been successfully implemented in MEMS for microscale transducers. The authors in [72] built a microgenerator with PVT to achieve 2.1 μW with 1.2 V load and 80 Hz vibration. Reference [73] has a four beam design, shown in Fig. 1-8, using PVT to generate 50 μW with a power density of 2 mW/mm^3 while also extending

the bandwidth of the resonance frequency. Reference [74] used zinc oxide nanogenerator with an aluminum nitride interlayer to generate up to 1.4 V across a 159 nm layer of cantilever. Researchers in [75] built a membrane based transducer, shown in Fig. 1-9, using PVDF to achieve 270 nW/mm^3. All these advances make using piezoelectric transducers to power microsystems promising.

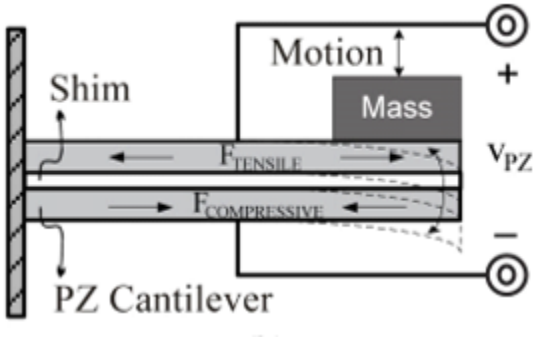

Figure 1-7. Typical piezoelectric transducer.

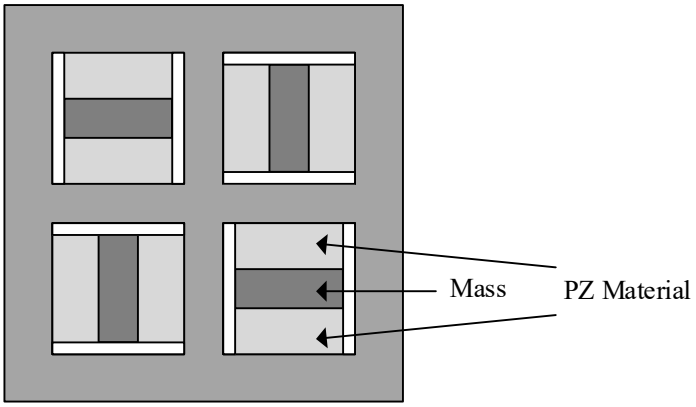

Figure 1-8. Structure of the four-beam wide bandwidth piezoelectric transducer [74].

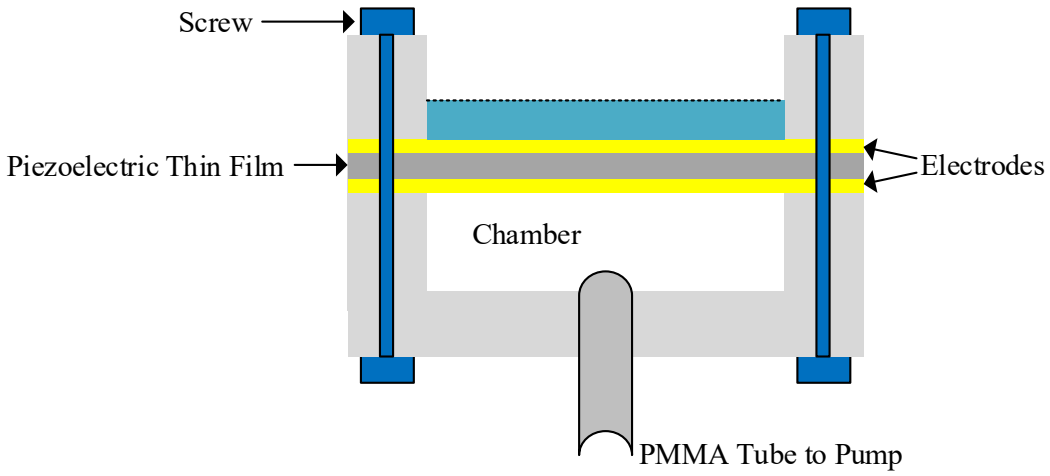

Figure 1-9. Membrane structure of piezoelectric transducer excited by air or liquid [75].

1.2.3. Electrical Model

When the cantilever shown in Fig. 1-7 bends upward under outside force, the piezoelectric material on top plate is under compressive force, while that on the bottom plate is under tensile force. The positive charge center and negative charge center shifts away from each other, creating positive charge at the top plate, and negative charge at the bottom plate. When the cantilever bends downward, on the other hand, vice versa, positive charge appears at the bottom plate, while negative accumulates at the top plate. As the vibration bends the cantilever up and down continuously, the charge alternates between the plates. We can model the phenomena with an alternating current source in parallel with the cantilever's parasitic capacitance, as shown in Fig. 1-10(b). When the cantilever goes up, the current i_{PZ} is positive, and when it goes down, i_{PZ} is negative. Because most of the vibrations found in nature is sinusoidal, the current source i_{PZ} is also a sinusoidal.

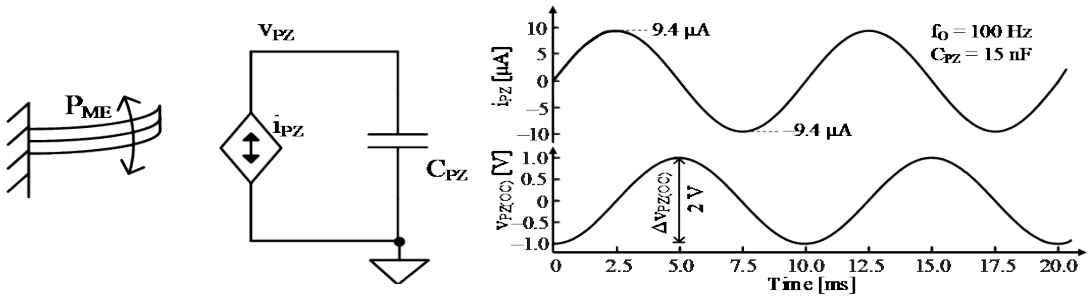

Figure 1-10. Piezoelectric transducer with its (a) mechanical model, (b) electrical model, and (c) electrical behavior.

Figure 1-10(c) illustrates the open circuit operation of the electrical model. Across the positive half cycle for i_{PZ}, the open circuit voltage $v_{PZ(OC)}$ rises from negative peak –1.0 V to positive peak 1.0 V. Similarly across the negative half cycle, $v_{PZ(OC)}$ drops back to negative peak –1.0 V. This electrical model will be used for the rest of this dissertation.

1.3. **Challenges for Piezoelectric-Powered Systems**

Unfortunately the transducers themselves cannot power the microsystems directly. The transducers and the various blocks on the microsystems have different voltage requirement and power profile, which calls for a power management circuits to make all the blocks run smoothly while consuming the least power. Figure shows the block level diagram of a piezoelectric-powered system. It senses the voltage created by the vibration on the transducer and charges the battery, while supplying the load on the sensors. In the meantime, it faces the following challenges.

1.3.1. Miniaturization

Wireless microsystems are usually placed at non-intrusive locations. Their small footprint also limits the dimension of the energy-harvesting unit. The tiny piezoelectric transducers

have reduced strain and surface area, lowing the amount of charge induced by the vibration, which in turn lowers the transduced power. The smaller cantilever also results in higher resonance frequency, and it is further away from the vibration frequencies most common in the environment and human motion, further reducing power. The size restriction also significantly limits the capability of the circuitry that conditions the transducer and manages the power flow. However, it is a fundamental restriction that all potential solutions must comply with.

1.3.2. Power management

The transducers and the various loads have very different power profile across time. The input power provided by the transducer is heavily dependent on the vibration it receives. In the case of a bridge, the air ventilation systems, or a heart monitor, the vibrations constantly exist, but the vibration frequency and amplitude vary throughout a day. In the case of a vehicle, a home, or inside a human's leg or shoe, the vibration is intermittent, and there could be long droughts where the input power is completely gone. Most applications still would like to have the microsensors to at least maintain some level of functionalities. Therefore, the transducers cannot be the only source to power the microsystems.

On the other hand, the microsystems also do not consume constant power. The majority of the time, the core circuitry is idle to save energy, and only the timing circuits or a comparator that senses a trigger event is left on. The sensors are only active if it is triggered by an activating event. The amplifiers and digital components then turn on to preliminarily process the data. After enough data is collected by a sensor, the transmitter transmits it to a central location for further processing and monitoring. Therefore, even

though the core blocks consume milliwatts (sensors) to 1 watt (transmitter) when they are on, they are all duty-cycled such that the average power of a microsensor can be 1–100 microwatt. That matches well with what MEMS piezoelectric transducers can on average produce, and therefore makes piezoelectric-powered microsystems viable.

Since the transducer cannot be the only energy or power source in a microsystem, a lithium-ion battery [99]–[100], supercapacitor [101]–[106], or ceramic capacitor [107] can become the additional energy storage unit that stores the energy from the vibration whenever they are present, and meet the instant high power demand that the loads require. Figure 1-11 shows the schematic of the power management system. The charger collects the charges from the transducer to charge the battery, and the battery, with the help with another power management supply block, supplies the loads of the microsystem.

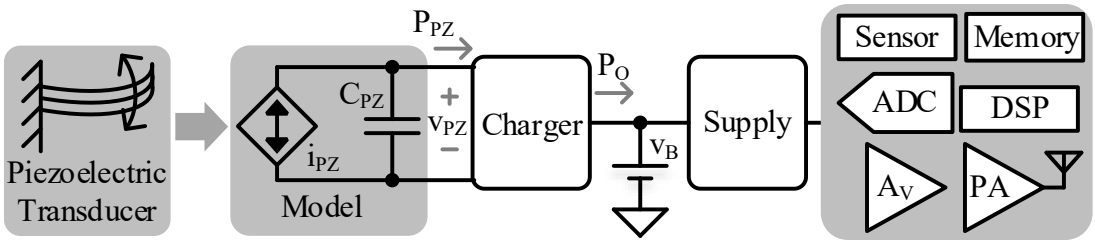

Figure 1-11. Piezoelectric-powered systems.

1.3.3. Maximum Power Point

The power produced by the transducer is heavily dependent on the strength and frequency of the vibration. However, the electrical conditions, i.e. voltage across the transducer and charges extracted from the plates, also affect the power that reaches the charger. Since the power level of the transducer is already low, and it can disappear for a long period of time, it is important to draw as much power as possible whenever the vibration is available. That

is why the system includes a maximum power point tracking (MPPT) block. It senses the vibration strength and, in some cases, the battery voltage, and configures the charger such that the charger outputs the most power into the battery. However, the MPPT block adds power consumption and silicon area to the overall solution. Therefore, when designing a charger, how to achieve maximum power point (MPP) is an important consideration.

1.3.4. Circuit Implementations and Limitations

The circuit that interact with the transducer also adds some constraint to the operation of the charger. As complimentary metal-oxide-silicon (CMOS) circuits reach smaller dimension, they also can only withstand lower voltages. In order to maintain safe functionality for a long time, the transducer voltage must be at or below the breakdown voltage of the CMOS circuitry. On another hand, any circuitry that conducts current consumes ohmic power loss. To turn a switch on or off requires charge, which is another form of power loss. The MPPT and controller requires quiescent power, and the switches and the transducer all have leakages. All these types of power consumption are subtracted from the power drawn from the transducer, and only the difference can reach the battery. Therefore, how to build a charger with the most drawn power, least losses on the charger, least area occupied by the MPPT, and least constraints is the ultimate challenge for the power management part of the piezoelectric-powered microsystems.

1.4. **Summary**

Wireless microsystems have widespread applications in smart homes, industrial automation, self-driving vehicles and traffic control, and healthcare that save money, energy, and lives. While the demand for their functionality keeps increasing, their footprint

requirement is becoming stringent. With the lack of breakthrough in battery technology in recent years, the onboard battery drains quickly, and needs recharging or replacing frequently, which increases cost and, in some cases, is dangerous or even impossible. Academia and industry have therefore looked elsewhere to prolong lifetime of the microsystems without sacrificing functionality. Fortunately, vibration exist omnipotently, and piezoelectric transducers can be integrated onto the microsensors to constantly replenish the battery.

Tiny piezoelectric transducers, however, have different power profile and voltage requirements from the various loads on the microsensors. Specifically, vibration can be intermittent, and the vibration level can vary across time. Therefore, to maximize the energy whenever they are available, the power management block needs to condition the voltage and power drawn from the transducer to operate at MPP. On the other hand, the blocks on the microsystems are duty cycled to reduce quiescent power consumption. The power management circuits need to supply the load whenever it needs to turn on, and shut it down as soon as their duty cycle is over. In addition, miniaturized circuits consume power loss, and it adds breakdown limits to the transducer. As a result, a charger that could draw the most power from the piezoelectric transducer while consuming the least power loss and inflict the least restriction on the sensor is needed to prolong lifetime and further expand functionality of wireless microsystems.

CHAPTER 2. STATE OF THE ART

Researchers have been developing and exploring ways harvest energy from piezoelectric transducers to power wireless microsystems since the early 2000s. Several generations later, new technology is still emerging with more extracted power and more efficient and less limiting interface circuitry. This chapter surveys, compares, and derives from the state of the art how tiny piezoelectric harvesters can generate power. The state of the art falls into three main categories: bridge-based rectifiers, synchronized discharges, and recycling-based chargers. The basic operation, features, limits, and variations for each category are summarized.

2.1. **Bridge-Based Rectifiers**

2.1.1. Operation

The first piezoelectric energy-harvesting charger was proposed in 2002 [108].The basic diode bridge in Fig. 2-1 consists of because the diodes rectify and steer i_{PZ} into a receiving capacitor C_{REC} [108]–[115]. When assuming diode voltages are zero, for example, i_{PZ}'s positive half cycle in Fig. 2-2 charges C_{PZ} until v_{PZ} overcomes C_{REC}'s rectified output voltage v_{REC}. Past that point and through the end of the positive half cycle, diodes D_{PG} and D_{PO} steer i_{PZ} into C_{REC}. Similarly, i_{PZ} across negative half cycles discharges C_{PZ} until D_{NG} and D_{NO} clamp v_{PZ} to $-v_{REC}$, past which point i_{PZ} flows, again, into C_{REC}.

Interestingly, raising v_{REC} increases the power i_{PZ} delivers into C_{REC} at v_{REC} as well as the charge lost to C_{PZ} when swinging v_{PZ} between v_{REC} and $-v_{REC}$. So for maximum power, the system should raise v_{REC} until the incremental loss cancels the additional gain,

which happens at a particular v_{REC}. This is why a charger in Fig. 2-1 draws just enough power from C_{REC} to keep v_{REC} near its maximum power point.

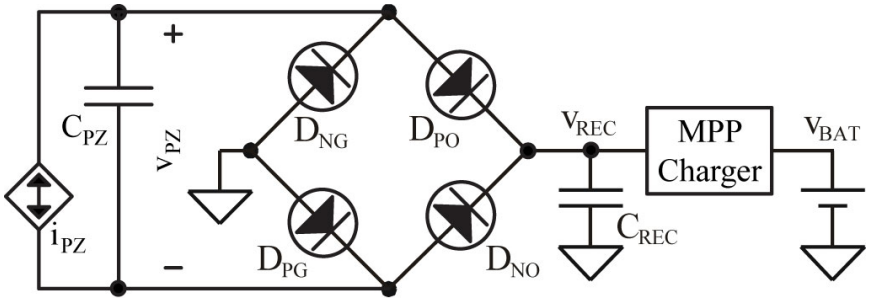

Figure 2-1. Diode-bridge charger.

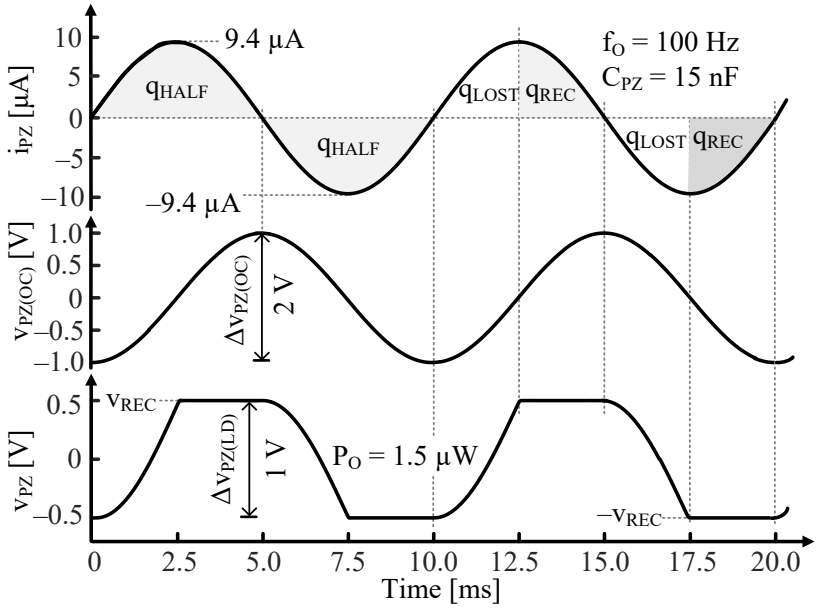

Figure 2-2. Ideal diode-bridge waveforms.

To quantify this point, consider that, without the bridge, i_{PZ}'s half-cycle charge q_{HALF} would charge C_{PZ} across peak–peak open-circuit voltage $\Delta v_{PZ(OC)}$, so

$$q_{HALF} = C_{PZ}\Delta v_{PZ(OC)}. \quad (3)$$

But since C_{PZ} absorbs some of q_{HALF} when charging across $2v_{REC}$, C_{REC} loses charge q_{LOST} to C_{PZ}:

$$q_{LOST} = C_{PZ}(2v_{REC}). \tag{4}$$

C_{REC} therefore collects with q_{REC} the difference every half cycle to harness with E_H twice q_{REC}'s energy per cycle:

$$E_H = 2(q_{HALF} - q_{LOST})v_{REC} = 2C_{PZ}\left(\Delta v_{PZ(OC)}v_{REC} - {v_{REC}}^2\right). \tag{5}$$

The maximum power point results when the incremental loss in q_{LOST} balances the additional gain in q_{HALF}, which happens when the combined derivative is zero and v_{REC} is $0.25\Delta v_{PZ(OC)}$:

$$\frac{dE_H}{dv_{REC}} = 2C_{PZ}\left(\Delta v_{PZ(OC)} - 4v_{REC}\right)|_{\Delta v_{PZ(LD)}=2v_{REC}=0.5\Delta v_{PZ(OC)}} \equiv 0. \tag{6}$$

In other words, E_H peaks to $0.25C_{PZ}\Delta v_{PZ(OC)}^2$ when the loaded swing $\Delta v_{PZ(LD)}$ is half the open-circuit counterpart $\Delta v_{PZ(OC)}$:

$$E_{H(MAX)} = 0.25C_{PZ}{v_{PZ(OC)}}^2. \tag{7}$$

Output power P_O can therefore be $0.25C_{PZ}\Delta v_{PZ(OC)}^2 f_O$.

2.1.2. Features

The diodes can steer charge from C_{PZ} to C_{REC} whenever the voltage on C_{PZ} is 2 diode voltages above v_{REC}. Therefore, no further controller is required to charge C_{REC}. Also the

solution is compact. However, this is the extent of the feature that the basic bridge has, and with the simplicity comes the low power and other limits that will be discussed next.

2.1.3. Limits

As discussed in its operation and shown in Fig. 2-2, part of the charge created by the vibration is lost to charge the capacitor C_{PZ} between $+v_{REC}$ and $-v_{REC}$. As a result, only a portion of the charge reaches the C_{REC}, and the rest is wasted. Equation (5) shows that at the maximum power point, half of the charge is lost to charging C_{PZ}. Since the charge produced by the transducer is already low, we cannot afford to lose half of it.

As for the portion of the charge that reaches C_{REC}, the power that it produces is low, and varies with other conditions. As (5) shows, harvested power P_{PZ} is a function of the rectified voltage v_{REC} The transducer outputs the maximum power $0.25C_{PZ}\Delta v_{PZ(OC)}^2 f_O$ only when $v_{REC} = 0.25\Delta v_{PZ(OC)}$, and it quickly falls when it drifts away from the maximum power point, and will not draw any power when C_{REC} is charged above $0.5\Delta v_{PZ(OC)}$. Since the power drawn from the piezoelectric transducer is already low, we need to maximize the drawn power whenever vibration is available. That is why in Fig. 2-1. there is a maximum power point (MPP) block between the rectifying capacitor and the battery v_B. The MPP block regulates v_{REC} at its maximum power point, and charges the battery. That means another stage of dc-dc converter is required, and it would either require a switched inductor stage [116]–[118], which is bulky for wireless microsystem applications, or a switched capacitor stage, which is less efficient [119]–[120].

Another limit of the basic diode is that the diode drop, which ranges from 0.6 – 0.8 V, would significantly lower the already low drawn power. Fig. 2-3 in [110] used cross-

coupled metal-oxide-semiconductor (MOS) devices to implement one pair of diode. They have only drop 10s of millivolt, so that in each half cycle v_{PZ} only needs to go approximately one diode voltage above v_{REC} to steer charge into C_{REC}. Fig. 2-4 in [111] used cross-coupled MOS pairs to implement both pairs of diodes, but an additional diode is needed to block reverse current from C_{REC} back into the transducer.

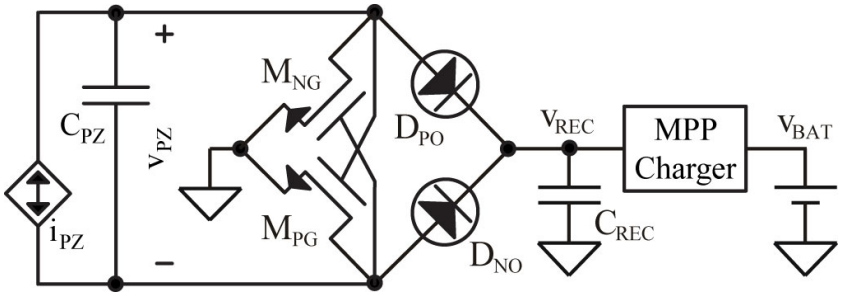

Figure 2-3. Cross-coupled diode-bridge rectifier.

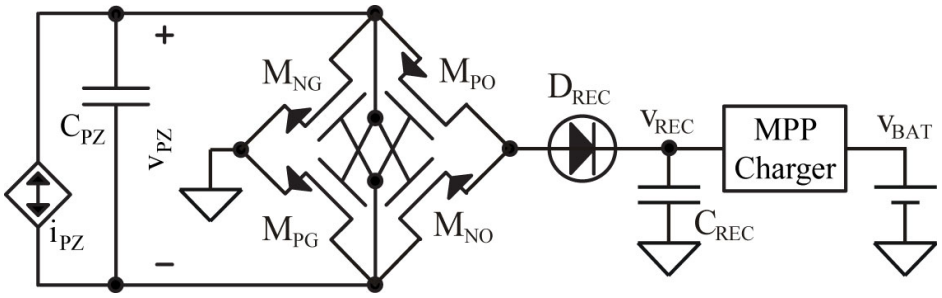

Figure 2-4. Cross-coupled diode-bridge charger (negative voltage converter NVC).

Although replacing two diodes in the full bridge with cross-coupled FETs is possible when v_{REC} is greater than a MOS threshold voltage, the same is not true for all diodes in the full bridge or diodes in the half bridge. And if v_{REC} is less than 0.6–0.8 V, like in Fig. 2-2, replacing two diodes is not even possible.

Ideally, a diode should drop 0 V, lose 0 A, and respond instantly. Although on-chip Schottky and P–N junction diodes drop 0.4–0.6 V and 0.6–0.8 V, they lose no ground

current and respond almost instantly. Similarly, the diode-connected FET in Fig. 2-5(b) drops a gate–source voltage v_{GS} that can be 0.6–0.9 V, loses 0 A, and although not to the same extent, responds very quickly.

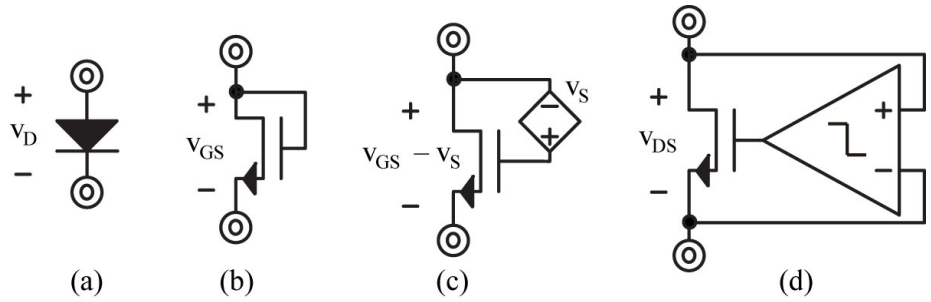

Figure 2-5. Diode options.

The voltage source v_S in Fig. 2-5(c) shifts the FET's v_{GS} by v_S so the switch can drop $v_{GS} - v_S$, which can be 100–200 mV [121] and correspond to a 70%–90% reduction in conduction power. The voltage is not lower because the tolerance of MOS threshold voltages is high on the order of ±75–±100 mV [122], so margin must exist to ensure the FET does not conduct reverse current. Irrespective, the tradeoffs for this reduction in conduction power are quiescent power and response time, because v_S is a circuit that requires power and time to react.

The FET in Fig. 2-5(d) drops an even lower voltage because the comparator can overdrive the FET into triode when terminal voltages are only millivolts apart [123]. This way, the drain–source voltage v_{DS} can be 25–100 mV and the corresponding conduction loss 80%–97% lower than a diode. Like before, though, the tradeoffs are quiescent power and response time. But since conduction losses and tolerance are lower, this option is often preferable over the shifted counterpart.

Adding an input offset to the comparator so it transitions early can offset the delay of the circuit to reduce its effective response time [124]. Too much offset, however, can trip the comparator before it should. A more important consideration is how saved conduction power stacks against quiescent power and the power lost because of the comparator's delay. In other words, if saved power does not outweigh losses, which can be the case when i_{PZ} is low, a diode can be a lower-loss option.

2.1.4. Variations: Half Bridge

The half bridge in Fig. 2-6 also rectifies and steers i_{PZ} into C_{REC} [125]–[128]. Similar to the ideal full bridge, i_{PZ}'s positive half-cycle charge in Fig. 2-7 charges C_{PZ} until v_{PZ} overcomes v_{REC}, past which point D_{REC} conducts i_{PZ} into C_{REC}. i_{PZ}'s negative half-cycle charge then drains C_{PZ} until D_G clamps v_{PZ} to 0 V and steers the rest of i_{PZ}'s negative half-cycle charge to ground. This means, C_{REC} only harnesses positive charge.

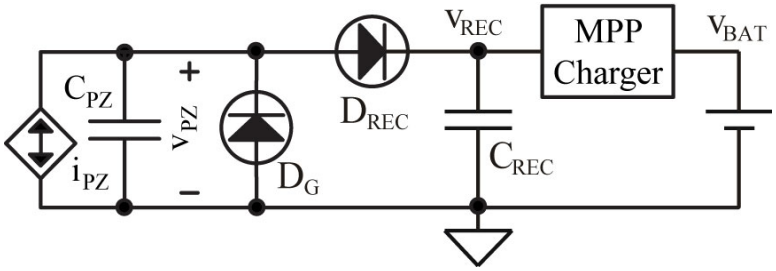

Figure 2-6. Half-bridge charger.

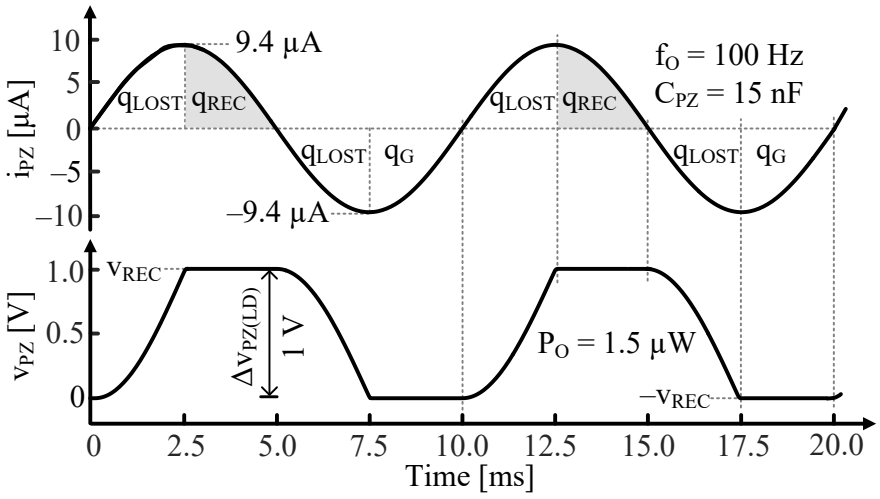

Figure 2-7. Ideal half-bridge waveforms.

Ultimately, C_{REC} collects the positive charge that i_{PZ} does not lose to C_{PZ} when swinging v_{PZ} across v_{REC}. But like before, i_{PZ} delivers more power to C_{REC} with a higher v_{REC} and C_{PZ} loses more charge when swinging across a wider v_{REC}. So maximum power results at the v_{REC} that balances this tradeoff. This is why Fig. 2-6 includes a MPP charger, to draw just enough power from C_{REC} to keep v_{REC} near its maximum power point.

To derive this maximum power point, first recall that i_{PZ}'s positive charge q_{HALF} is still $C_{PZ}\Delta v_{PZ(OC)}$. But since i_{PZ} loses positive charge q_{LOST} to C_{PZ} when charging to v_{REC}:

$$q_{LOST} = C_{PZ}v_{REC}. \tag{8}$$

C_{REC} collects with q_{REC} and E_H the difference at

$$E_H = 2(q_{HALF} - q_{LOST})v_{REC} = C_{PZ}\left(\Delta v_{PZ(OC)}v_{REC} - {v_{REC}}^2\right). \tag{9}$$

Maximum power results when the incremental loss cancels the additional gain, or when the combined derivative is zero and v_{REC} is twice that of the full bridge at $0.5\Delta v_{PZ(OC)}$:

$$\frac{dE_H}{dv_{REC}} = 2C_{PZ}\left(\Delta v_{PZ(OC)} - 2v_{REC}\right)\Big|_{\Delta v_{PZ(LD)}=v_{REC}=0.5\Delta v_{PZ(OC)}} \equiv 0. \quad (10)$$

In other words, C_{REC} collects half the charge of the full bridge at twice the voltage, so E_H can be the same: $0.25C_{PZ}\Delta v_{PZ(OC)}^2$. Plus, the optimum loaded swing $\Delta v_{PZ(LD)}$ is still $0.5\Delta v_{PZ(OC)}$.

Similar to the full bridge, half bridge also charges CREC asynchronously, without additional circuit to sense half cycles. It is even more compact than the full bridge, and consumes lower diode loss because in each direction the current only goes through one diode.

However, also similar to the full bridge, the half bridge has the same limits. Only a quarter of the charge reaches the rectifying capacitor at the maximum power point, resulting in low power. The maximum power point is also dependent on the rectifying voltage vREC, and falls off quickly when it shifts away from the optimum point, eventually drawing no power at $\Delta v_{PZ(OC)}$. This also calls for an additional MPP block to regulate vREC. Since the diodes do not come in pairs, half bridges cannot utilize cross-coupled pairs to lower the diode drop. However, synchronized diodes in Fig. 2-5(c) and (d) can still be used to implement half bridge.

2.2. **Synchronous Discharges**

The next category of piezoelectric harvesters uses synchronous discharges to collect all the charge generated by the vibration to charge the battery, with the help of switched inductors. The fundamental aim of inductors in energy harvesters is to transfer energy. When

connected across a battery v_{BAT}, for example, an inductor L_X draws current and energy from v_{BAT}. In this case, L_X's energizing voltage v_E is v_{BAT}, and since v_{BAT} is fairly constant, L_X's current i_L rises linearly with time at the rate of v_E/L_X like Fig. 2-8(a) shows. So when L_X collects with i_L the desired amount of energy $0.5L_Xi_{L(PK)}^2$ from v_{BAT} across energizing time t_E, the system disconnects L_X from v_{BAT}.

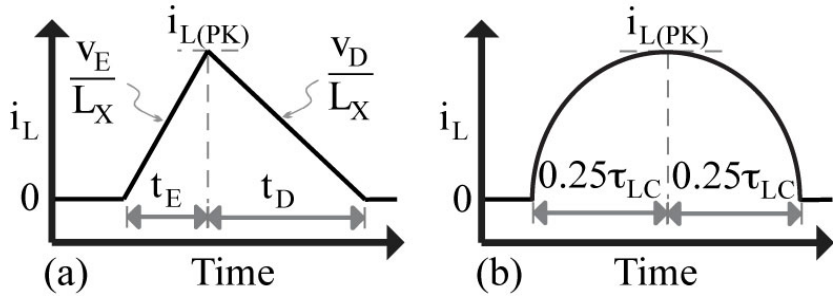

Figure 2-8. Energy transfers with (a) batteries and (b) capacitors.

Draining L_X into a battery is similar, but in reverse. Here, once L_X has energy in the form of i_L, the system connects v_{BAT} across L_X such that L_X's voltage is negative. With such a de-energizing voltage v_D, i_L falls linearly with time to drain into v_{BAT} at the rate of v_D/L_X. When L_X depletes, which happens when i_L is zero, the system disconnects L_X from v_{BAT}.

Drawing and supplying energy to a capacitor C_X is basically the same. When connecting an empty L_X across a charged C_X, for example, C_X discharges into L_X. But since C_X's voltage falls as C_X drains, i_L's rising rate decreases with time to produce the quarter sinusoid shown in Fig. 2-8(b). Irrespective of C_X's initial energy, C_X drains completely into L_X after a quarter resonance period $0.25\tau_{LC}$. Supplying a capacitor is the same, but in reverse. When connecting an energized L_X across an empty C_X, L_X's i_L charges C_X, i_L drops more quickly as C_X's voltage rises, and L_X fully depletes after $0.25\tau_{LC}$.

Since peak currents $i_{L(PK)}$, inductances L_X, and piezoelectric capacitances C_{PZ} in small commercially available transducers are usually below 100 mA, 300 µH, and 50 nF and battery voltages v_{BAT} are above 1 V [124], transfers complete within 4 µs. So of the 3 ms to 1 s that a typical cycle can last [54], each transfer normally requires less than 0.2% of the vibration period. This means, transfers are practically instantaneous.

To carry energy without consuming much power, inductor currents and resistances should be low. For low currents, inductances should be high, and for low resistances, coils should be large. This is why many implementations use 100-µH to 10-mH inductors that occupy more than $6 \times 6 \times 3$ mm^3.

2.2.1. No Pre-Charge

2.2.1.A. Operation

Basic switched-inductor harvesters use an inductor L_X to drain between cycles the charge that C_{PZ} collects across half cycles [129]. This way, with synchronous electric charge extraction (SECE), i_{PZ}'s positive half-cycle charge charges the unloaded C_{PZ} to $\Delta v_{PZ(OC)}$ in Fig. 2-9. At the end of i_{PZ}'s positive half cycle, L_X drains C_{PZ} into the battery v_{BAT}. i_{PZ}'s negative half-cycle charge then charges C_{PZ} to $-\Delta v_{PZ(OC)}$ and L_X drains C_{PZ} into v_{BAT} at the end of the half cycle.

One way to synchronize discharges into v_{BAT} is to rectify v_{PZ} across half cycles with a bridge and drain C_{PZ} into v_{BAT} between half cycles with L_X like Fig. 2-10 shows [130]. This way, v_{REC} in Fig. 2-11 follows v_{PZ} across i_{PZ}'s positive half cycles to peak at $\Delta v_{PZ(OC)}$. When half cycles end, switch S_G closes long enough to drain C_{PZ} into L_X. When S_G opens,

S_O closes and D_G conducts to deplete L_X into v_{BAT}. v_{REC} then mirrors v_{PZ} across i_{PZ}'s negative half cycles to peak at $\Delta v_{PZ(OC)}$, at which points S_G, D_G, and S_O drain C_{PZ} into L_X and L_X into v_{BAT}.

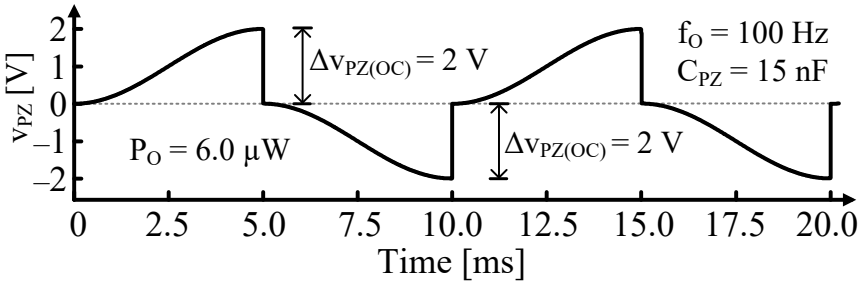

Figure 2-9. Synchronized switched-inductor discharges.

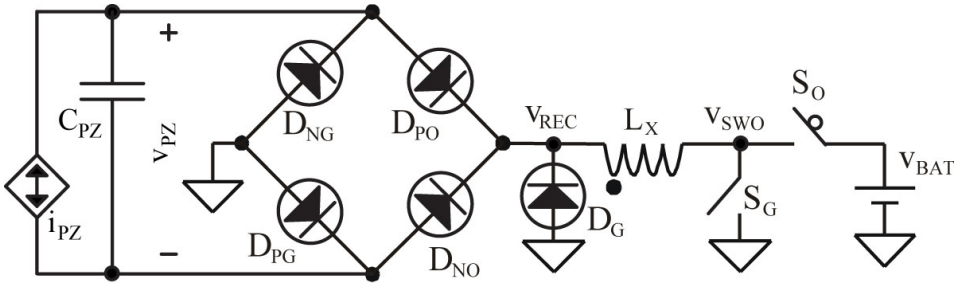

Figure 2-10. Bridged switched inductor.

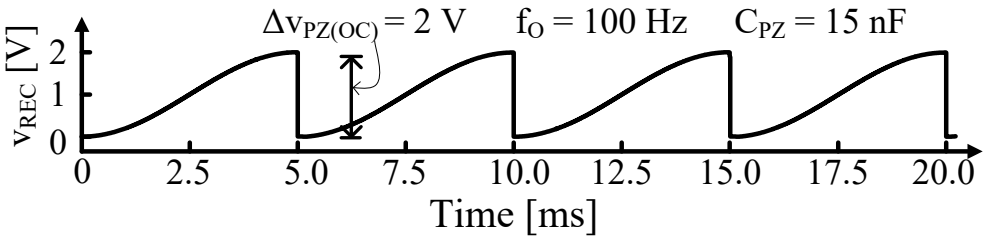

Figure 2-11. Rectified piezoelectric voltage in the bridged switched inductor.

L_X in Fig. 2-12 discharges C_{PZ} directly without a bridge [131]. Here, i_{PZ} charges C_{PZ} across half cycles like Fig. 2-9 shows. At v_{PZ}'s positive peak $\Delta v_{PZ(OC)}$, S_N and S_P close long enough to drain C_{PZ} into L_X. Then, S_P opens and L_X's i_L flows through D_P into v_{BAT} until L_X

depletes. At the end of the negative half cycle, when v_{PZ} peaks at $-\Delta v_{PZ(OC)}$, S_N and S_P again close to drain C_{PZ} into L_X. Then, S_N opens and L_X's i_L, which is now flowing up toward v_{SW-}, flows through D_N into v_{BAT}.

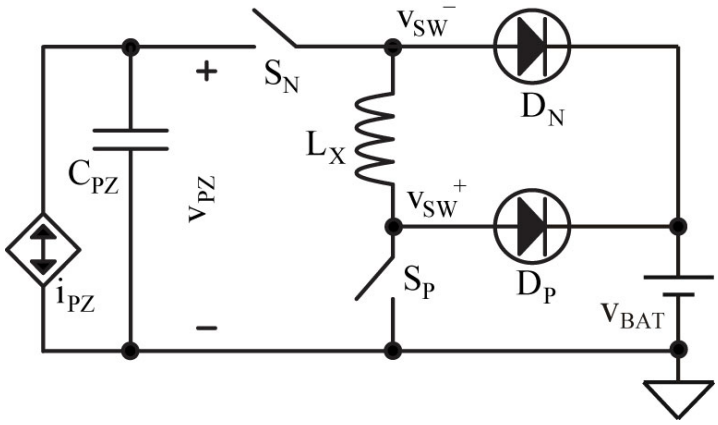

Figure 2-12. Bridgeless switched inductor.

2.2.1.B. Features

Since v_{BAT} receives between half cycles the energy C_{PZ} collects across half cycles, v_{BAT} in one cycle harnesses with E_H twice the energy C_{PZ} collects with $\Delta v_{PZ(OC)}$:

$$E_H = E_{C(+)} + E_{C(-)} = 2\left(0.5 C_{PZ} \Delta v_{PZ(OC)}{}^2\right) = C_{PZ} \Delta v_{PZ(OC)}{}^2. \quad (11)$$

Note this energy is 4× higher than that of basic diode bridges. One reason for this is basic bridges lose i_{PZ} charge to C_{PZ} when swinging v_{PZ} between rectified limits. Another reason is C_{PZ}'s energy rises quadratically with v_{PZ}, so the switched inductor collects more energy with 4× the loaded swing at $2\Delta v_{PZ(OC)}$ than the basic diode bridge does with $0.5\Delta v_{PZ(OC)}$.

Another feature for the synchronous discharge is that the power stage can directly connect to the battery without affecting drawn power. The synchronous discharge, because

of the use of switched inductor, divides the energy transfer into two parts: the transducer first transfer all the energy it collects across the half cycle into the inductor, and then the inductor charges the battery. The two steps have limited effect on each other. Therefore, the MPP block that the bridge-based rectifiers require is removed, saving volume and power loss for the system. Note that MPP function still exists by controlling the turn on time and sequence for the switches, but does not require an extra power stage.

2.2.1.C. Limits

Although L_X's series resistance (i.e., quality factor) and other losses limit some of these gains, a fundamental drawback and challenge with switched inductors is synchronizing switching events. Basic diode bridges draw piezoelectric power automatically whenever v_{PZ} overcomes its rectified output v_{REC}. Switched inductors, on the other hand, must synchronize energy transfers to i_{PZ}'s half-cycle points. This means, switched inductors require a power-consuming controller that basic bridges do not. Still, nanowatts for the controller is usually not enough to trump the microwatts that switched inductors gain over basic bridges.

For the bridgeless implementation in Fig. 2-9, fixing C_{PZ}'s bottom terminal to ground creates one subtle, though not insignificant disadvantage. The drawback is, C_{PZ}'s negative half-cycle voltage exposes S_N to negative voltages. This means, conventional CMOS switches must bias their P-type substrates to a voltage that is at least just as negative to isolate the switches from other devices in the die.

The circuit also suffers from one limitation worth noting. For D_N not to conduct when C_{PZ} drains into L_X at the end of i_{PZ}'s positive half cycle, v_{PZ}'s peak $\Delta v_{PZ(OC)}$ should not exceed v_{BAT}. This is usually not a problem for tiny transducers because they typically

capture a very small fraction of the mechanical energy available.

The last limit is that although the drawn power is 4× higher compared with an ideal bridge, it is still low when the vibration is low. Pre-charging can significantly increase drawn power, as will be discussed next.

2.2.2. Pre-Charge

Tiny piezoelectric transducers can only convert a small portion of the energy in the vibration into the electrical domain [132] – [150]. The attribute limits the power that the transducer avails to the charger, and subsequently, to the wireless microsystem. However, it also means that the power we do extract from the transducer does not affect the vibration. In other words, i_{PZ} is not affected by the drawn power, and it stays a constant sinusoid when the vibration is sinusoid. Therefore, applying an in-phase voltage that is as high as possible can increase drawn power. Pre-charging C_{PZ} between half cycles and allowing i_{PZ} to charge C_{PZ} above that level across half cycles, like Fig. 2-13 illustrates, draws more power from motion than without pre-charging C_{PZ} [38]. In other words, the system recovers much more than just the energy invested E_P to pre-damp C_{PZ} to v_P.

2.2.2.A. Operation

L_{P+} and L_{P-} in the bridged switched inductor of Fig. 2-14 pre-damp C_{PZ} to v_P between half cycles, like just described, to increase the voltage with which i_{PZ} sources power. Reference [134] does pretty much the same, but with more switches. In all, the bridge rectifies v_{PZ} across half cycles so L_X can drain C_{PZ} into v_{BAT} and L_{P+} and L_{P-} can pre-damp C_{PZ} between half cycles. So just before a positive half cycle, S_+ closes to energize both L_{P+} and C_{PZ}.

When v_{PZ} surpasses v_{BAT}, L_{P+} begins to drain into C_{PZ} what L_{P+} collected before v_{PZ} reached v_{BAT}. The controller then opens S_+ when L_{P+} depletes, at which point v_{PZ} is at v_P.

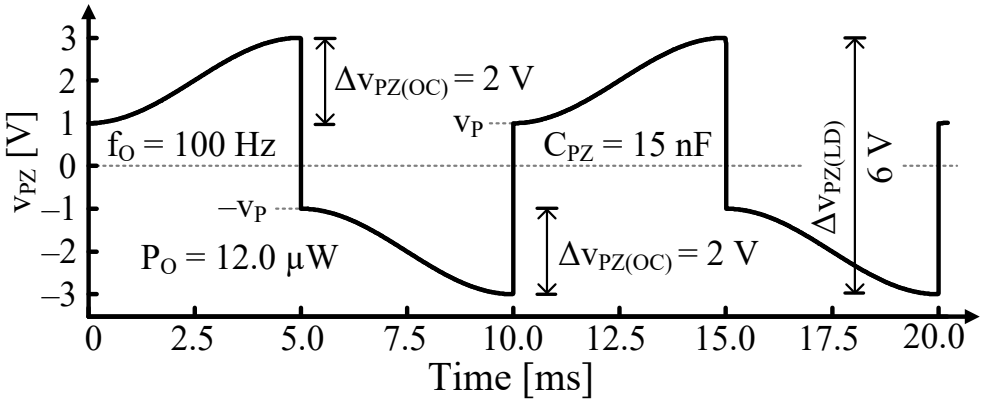

Figure 2-13. Synchronized and pre-damped discharges.

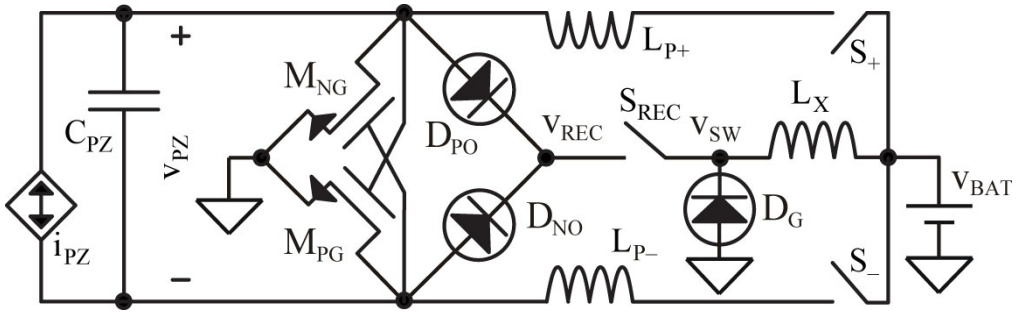

Figure 2-14. Bridged switched inductors.

When the positive half cycle ends, when v_{PZ} peaks to $v_P + \Delta v_{PZ(OC)}$, S_{REC} closes to drain C_{PZ} into L_X and v_{BAT}, and when v_{PZ} falls below v_{BAT}, C_{PZ} and L_X deplete into v_{BAT}. If L_X still has energy when v_{PZ} is zero, S_{REC} opens and D_G steers what remains in L_X into v_{BAT}. Also at this point, $S_–$ and $L_{P–}$ mirror the action of S_+ and L_{P+} to pre-charge C_{PZ} to $–v_P$. $S_–$ therefore closes to energize $L_{P–}$ and C_{PZ} in the negative direction, $L_{P–}$ begins to drain into C_{PZ} when $–v_{PZ}$ surpasses v_{BAT}, and when $L_{P–}$ depletes, $S_{N–}$ opens.

The switched inductors and bridge in Fig. 2-15 similarly pre-damp C_{PZ} after

synchronized discharges [135]. Here, the bridge rectifies across half cycles, L_X drains C_{PZ} partially into v_{BAT}, and L_R recycles what is left in C_{PZ} back into C_{PZ} to pre-damp C_{PZ} in the opposite direction. So when v_{PZ} peaks at $v_P + \Delta v_{PZ(OC)}$, S_{REC}, D_G, and L_X drain C_{PZ} partially to v_P. S_R then depletes C_{PZ} into L_R, and with S_R still closed, L_R returns C_{PZ}'s energy to pre-damp C_{PZ} to $-v_P$. At the next half cycle, S_{REC}, D_G, and L_X similarly drain C_{PZ} from $-(v_P + \Delta v_{PZ(OC)})$ to $-v_P$ and S_R and L_R recycle what is left to pre-charge C_{PZ} to v_P.

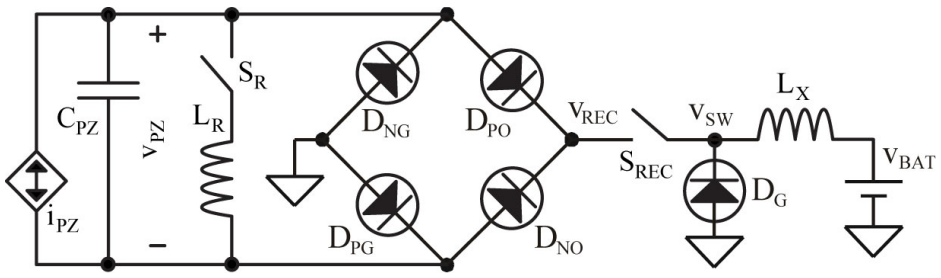

Figure 2-15. Recycling and bridged switched inductors.

To follow the flow of energy into v_{BAT} more closely, the bridge and S_{REC} first discharge C_{PZ} into L_X and v_{BAT} until v_{PZ} falls to v_P. S_{REC} then opens, so L_X's i_L flows from ground to v_{BAT} through D_G until L_X exhausts its energy into v_{BAT}. The same happens at the end of the negative half cycle: S_{REC} discharges C_{PZ} into L_X and v_{BAT} until v_{PZ} is $-v_P$ and D_G then depletes L_X into v_{BAT}. In other words, v_{BAT} receives part of the energy C_{PZ} collects across half cycles when S_{REC} closes and the rest when S_{REC} opens. And L_R recycles the energy required to pre-damp C_{PZ} to v_P and $-v_P$.

Interestingly, the bridgeless switched inductor in Fig. 2-16 pre-damps only i_{PZ}'s negative half cycle [140]. This is acceptable when under-damped to the extent that drawn power has negligible effects on cantilever displacement and velocity. This may also be desirable in applications that call for asymmetrical damping of the moving cantilever.

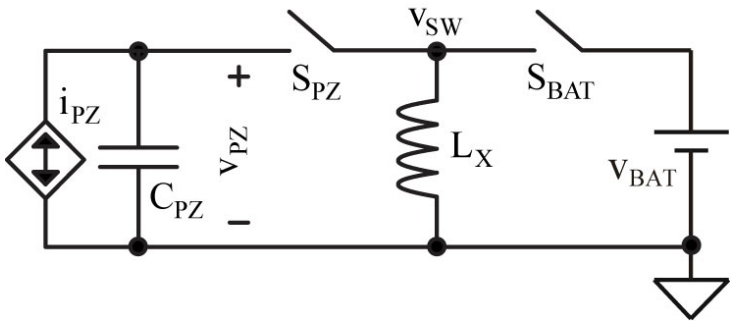

Figure 2-16. Pre-damping bridgeless switched inductor.

Operationally, i_{PZ} charges C_{PZ} across i_{PZ}'s positive half cycles to $\Delta v_{PZ(OC)}$. At that point, S_{BAT} closes to draw pre-damping energy from v_{BAT} into L_X. S_{BAT} then opens and S_{PZ} closes to deplete C_{PZ} into L_X. S_{PZ} remains closed long enough to cycle L_X's combined energy back to C_{PZ}. This way, C_{PZ} pre-damps to a level $-2v_P$ in Fig. 2-17 that v_{BAT}'s investment controls. i_{PZ} then charges C_{PZ} across i_{PZ}'s negative half cycle to $-(2v_P + \Delta v_{PZ(OC)})$. At that point, S_{PZ} first closes to deplete C_{PZ} into L_X. Once drained, when v_{PZ} is zero, S_{PZ} opens and S_{BAT} closes to drain L_X into v_{BAT}. This sequence then repeats.

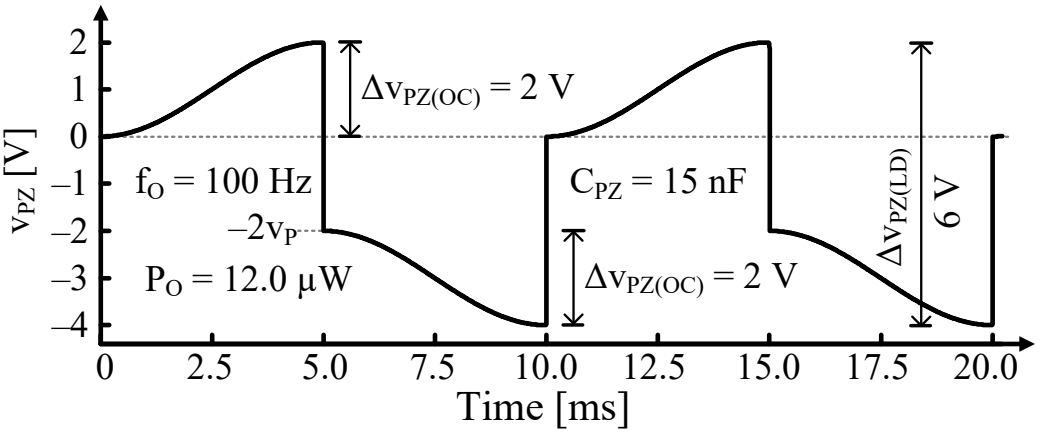

Figure 2-17. Bridgeless switched-inductor voltage.

2.2.2.B. Features

To pre-charge C_{PZ} to v_P between half cycles, the system must first deposit E_P, or $0.5C_{PZ}v_P^2$, into C_{PZ}. But since i_{PZ} charges C_{PZ} another $\Delta v_{PZ(OC)}$ across each half cycle, the system recovers $E_{C(PK)}$ or $0.5C_{PZ}(v_P + \Delta v_{PZ(OC)})^2$. So across an entire cycle, v_{BAT} invests and recovers twice these amounts to net E_H:

$$\begin{aligned} E_H &= 2\left(E_{C(+)} + E_{C(-)}\right) = 2\left[0.5C_{PZ}\left(v_P + \Delta v_{PZ(OC)}\right)^2 - 0.5C_{PZ}{v_P}^2\right] \\ &= C_{PZ}{\Delta v_{PZ(OC)}}^2 + 2C_{PZ}\Delta v_{PZ(OC)}v_{P)}. \end{aligned} \tag{12}$$

Not surprisingly, E_H here exceeds that of basic switched inductors, which already collects all the charge. Pre-charging enjoys the most benefit when the vibration strength, which translates to the open circuit voltage $\Delta v_{PZ(OC)}$, is low. It is therefore a critical technique to continue harvesting moderate to high power when vibration slowly dies down. Plus, E_H grows with v_P, so v_P should be as high as breakdown voltage V_{BD} and power losses allow. This means, $v_P + \Delta v_{PZ(OC)}$ should not surpass V_{BD}, which is equivalent to saying v_P should remain below $V_{BD} - \Delta v_{PZ(OC)}$.

The switches in pre-charge synchronous discharges are implemented with MOSFETs, which when turned fully on drop 10 to 150 mV, and consume low ohmic loss compared to diodes. Plus, the bridgeless switched-inductor power stage employs only two power switches, reducing the dimension of the system and further reduces losses. However, these features do not come without drawbacks, which are discussed next.

2.2.2.C. Limits

Even though pre-charging can increase drawn power, the reported power stages all have their limits. The circuits in Fig. 2-14 and Fig. 2-15 use multiple bulky inductors, significantly increase the volume of the system. Moreover, the three inductor power stage in Fig. 2-14, much like a buck or step-down converter, only works when the peak voltage on the transducer is higher than the battery voltage. On the other hand, the power stage in Fig. 2-15 only works when the battery voltage is high enough to discharge C_{PZ}, much like a boost or step-up converter. More switches are required to make either power stage to function in all conditions, with the drawbacks of more ohmic loss, switching loss, and higher volume.

The power stage in Fig. 2-16, on the other hand, works with all voltage conditions. However, as with its bridgeless predecessor from Fig. 2-12, C_{PZ}'s negative half-cycle voltage exposes S_{PZ} to negative voltages. Conventional CMOS switches must therefore bias their P-type substrates to a voltage that is at least just as negative to isolate the switches from other devices in the die. This is a subtle, though not insignificant requirement for this circuit. One other limits for this asymmetrical approach is that because of the negative supply present in the power stage, the peak to peak swing of the switching node v_{SW}, which is the same as the loaded peak to peak swing of v_{PZ}, much be lower than the breakdown voltage. With increasingly finer technology nodes and lower breakdown voltage for newer processes, this can be a significant limiting factor for the power stage.

2.3. **Recycling**

2.3.1. Operation

As explained in Section 2.2.2, the power that piezoelectric transducers produce rises with the voltage across it, provided that it is in phase with the current. Recycling power stages therefore takes the most advantage of that feature, and keeps v_{PZ} at the breakdown voltage across the half cycle. Between half cycles, when i_{PZ} is at 0, the power stage almost instantaneously extract all the charge from C_{PZ}, and put it back in the opposite direction.

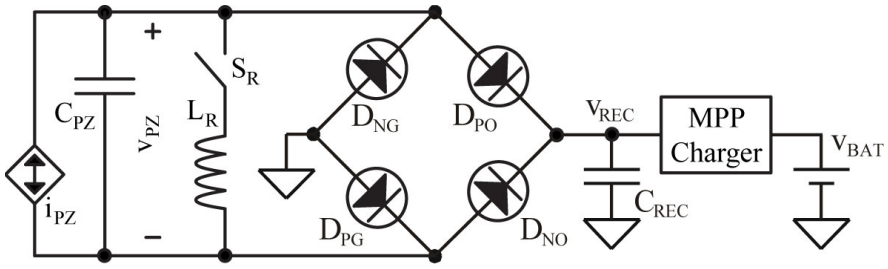

Figure 2-18. Recycling switched-inductor or parallel SSHI diode bridge.

The circuit in Fig. 2-18 achieves just that [132], [142] – [150]. Here, L_R recycles the charge that i_{PZ} loses the first time i_{PZ} charges C_{PZ} across the bridge's $2v_{REC}$ so C_{REC} can receive all of i_{PZ}'s charge after that. For this, S_R closes between half cycles to drain C_{PZ} into L_R and L_R back into C_{PZ} and swing v_{PZ} in Fig. 2-19 from v_{REC} to $-v_{REC}$ at the end of the positive half cycle and back from $-v_{REC}$ to v_{REC} at the end of the other half. Since v_{PZ} is already at v_{REC} before new half cycles begin, all of i_{PZ}'s charge flows into C_{REC}.

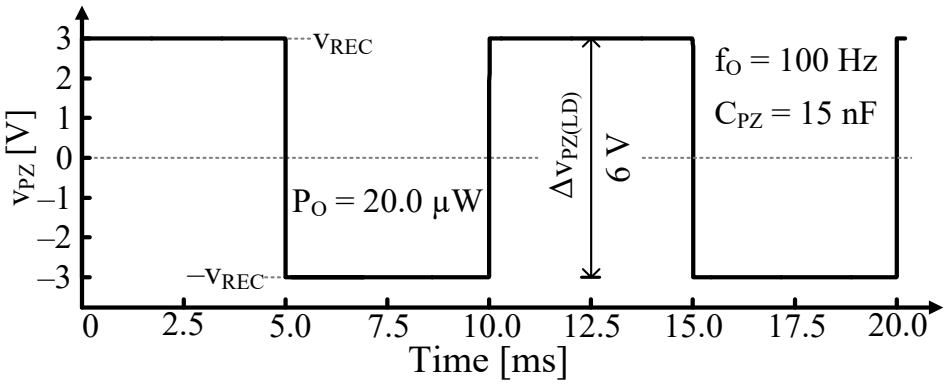

Figure 2-19. Recycled switched-inductor diode-bridge voltage waveform.

2.3.2. Features

This strategy features two important traits. First, C_{REC} collects all i_{PZ}'s charge. Second, since i_{PZ} no longer loses charge to C_{PZ}, v_{PZ}'s loaded swing $\Delta v_{PZ(LD)}$ need no longer halve v_{PZ}'s unloaded counterpart $\Delta v_{PZ(OC)}$. As a result, no tradeoff counters the rise in power that i_{PZ} produces at v_{REC} when v_{REC} is higher. C_{REC} can therefore collect twice i_{PZ}'s half-cycle charge q_{HALF} at the highest possible v_{REC} all the time:

$$E_H = 2q_{HALF}v_{REC} = 2C_{PZ}\Delta v_{PZ(OC)}v_{REC} \leq 2C_{PZ}\Delta v_{PZ(OC)}V_{BD}. \quad (13)$$

Not surprisingly, the harvested power is the highest among all the schemes. The high drawn power does not come without its limits, however, and that is discussed next.

2.3.3. Limits

Since v_{BAT}'s value is unpredictable, and therefore is seldom at the breakdown voltage V_{BD}, the recycling diode bridge cannot charge v_{BAT} directly. So like its predecessor, the circuit requires a maximum power-point charger. The basic aim of the charger is, like before, to draw just enough power to keep v_{REC} near V_{BD}. This again calls for an additional switched-

inductor stage, which is bulky and loses some power, or a switched-capacitor stage, which is even less efficient.

2.4. **Summary**

Over the years, researchers have developed three types of chargers for piezoelectric-powered wireless microsystems: bridge, synchronous discharges, and recycling. The bridge can draw power asynchronously, but some of the charge is lost to charging C_{PZ}, and as a result it can only draw little power. In addition, power level varies significantly with rectifying voltage, and therefore it requires a maximum power point stage to regulate v_{REC}. Its variations can save some diode power, but cannot overcome these fundamental limits. Synchronous discharge power stages collect all charge, and can draw 4× more power. It can also charge the battery directly, removing the MPP stage. However, the power is still low when the vibration is weak. It also requires the controller to synchronize with the half cycle of the vibration, require more complex design and quiescent power. Pre-charge can raise the voltage with which the charge is collected, thereby increasing drawn power even more. However, the solutions either require multiple bulky inductors, or need negative supply that impose stricter breakdown limit. Recycling power stage can keep the piezoelectric voltage at the highest across the half cycles, resulting in the highest possible drawn power. But it also needs to synchronize with the half cycles. In addition, it needs to regulate the rectifying voltage. Therefore, it needs an additional MPP stage that is bulky and consumes more power loss.

CHAPTER 3. SYNCHRONIZED DISCHARGE SYMMETRY

Synchronous discharging chargers can harvest ambient kinetic energy with a single inductor to constantly replenish the battery for wireless microsystems. Because of the low fraction of vibration power that piezoelectric transducer can convert into the electrical domain, the charger needs to maximize the power it can output to the battery to prolong lifetime and expand functionality for the microsystems. Among the state of the art, as summarized in Chapter 2, the bridgeless switched inductor in Fig. 2-16 that utilizes asymmetrical pre-charging is the only reported prototype that uses only one inductor and can achieve controllable pre-charging to increase drawn and output power. Despite its simple two-switch design, it has some limits, most notably the need of a negative supply, and that he peak to peak voltage needs to be below the breakdown voltage. There is a more subtle, yet still significant, drawback for the asymmetrical pre-charging, which will be examined in detail in this chapter. Specifically, this chapter will detail the operation of both asymmetrical pre-charging and symmetrical pre-charging, compare the drawn power, and output power.

3.1. **Synchronized Discharges**

In piezoelectric chargers with synchronized discharges, the transducer's i_{PZ} charges C_{PZ} across half cycles so that the switched inductor L_X can drain and deliver C_{PZ}'s energy to v_{BAT} between half cycles. As shown in Fig. 3-1, the charger draws P_{PZ} from the transducers i_{PZ} and C_{PZ}, and output P_B to the battery. This way i_{PZ} charges C_{PZ} to open-circuit voltage $\Delta v_{PZ(OC)}$ every half cycle. And between half cycles, L_X discharges C_{PZ} and delivers C_{PZ}'s energy $E_{C(PK)}$ at $\Delta v_{PZ(OC)}$ to v_{BAT}. Notice that the *microsecond* time L_X requires to transfer

these energy packets is so much shorter than t_{VIB}'s *millisecond* period that transfers are nearly instantaneous in the figure.

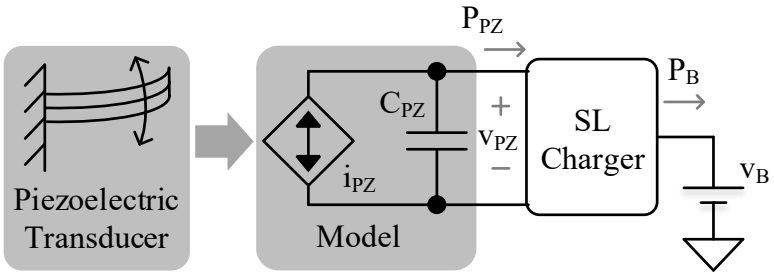

Figure 3-1. System schematic for piezoelectric synchronized discharges chargers.

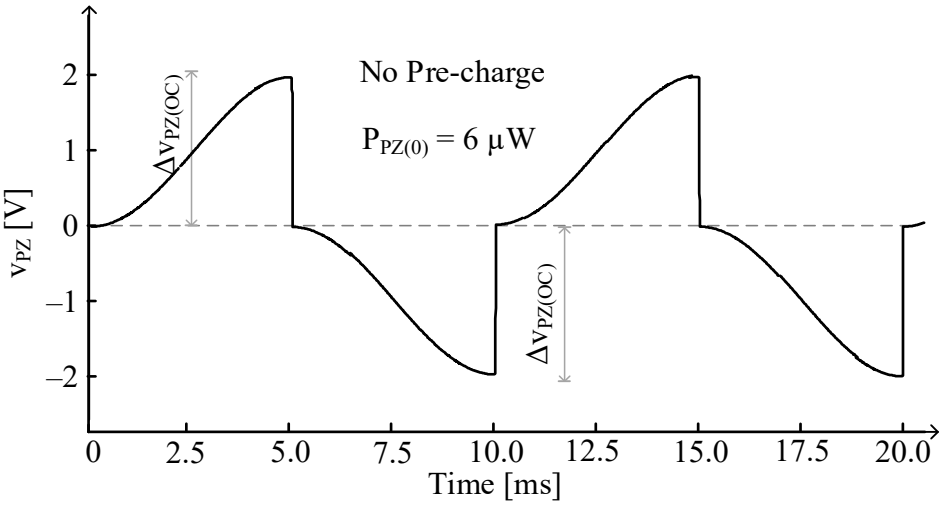

Figure 3-2. Piezoelectric voltage without pre-charging.

The synchronized discharge without pre-charging has a symmetrical operation, as shown in Fig. 3-2. The peak voltage in both the positive direction and the negative direction is the open-circuit voltage $\Delta v_{PZ(OC)}$. The peak-to-peak voltage, labeled $v_{PZ(PP)}$, is therefore $2\Delta v_{PZ(OC)}$.We call this the total damping the transducer is exposed to. This is an important parameter, because if a voltage node in the charger is exposed to the entire swing of the

piezoelectric transducer, $v_{PZ(PP)}$ has to be below the breakdown voltage of the system to avoid breakdown problems.

Pre-charging C_{PZ} to v_{PC} between half cycles allows v_{PZ} to both start and end at higher voltages. Since i_{PZ} is basically a current source, i_{PZ} delivers more energy this way, with a higher voltage. In other words, v_{PC} raises the piezoelectric damping force against which motion works to supply power.

3.1.1. Symmetrical Pre-Charge

The chargers in [134], [135]–[136] pre-charge C_{PZ} for both half cycles. Unfortunately, they either use multiple inductors, which occupy considerable space and consume substantial power, or v_{BAT} limits C_{PZ}'s pre-charging level. The charger in Fig. 2-12 [131], on the other hand, is flexible enough with one inductor to pre-charge C_{PZ} to almost any value. Although similar to [131], the operation of this circuit is vastly different because this topology pre-charges C_{PZ} and the one in [131] does not. Note, by the way, D_N is in practice a switch that operates like a diode, so D_N drops millivolts when conducting.

Here, S_{PZ} and S_G close at the end of the positive half cycle across a quarter resonance period $0.25\tau_{LC}$ to drain C_{PZ} into L_X plus a fraction of that to start pre-charging C_{PZ}. S_G then opens and D_N steers L_X's i_L to v_{BAT} so C_{PZ} pre-charges to $-v_{PC}$ and v_{BAT} receives whatever energy remains. C_{PZ}'s v_{PZ} in Fig. 3-3 at 5 ms therefore collapses to zero and pre-charges to $-v_{PC}$.

i_{PZ} then charges C_{PZ} by $\Delta v_{PZ(OC)}$ across i_{PZ}'s negative half cycle to $-(v_{PC} + \Delta v_{PZ(OC)})$. At that point, at 10 ms, S_{PZ} and S_G similarly close long enough to drain C_{PZ} into L_X, and at some point, S_{PZ} opens and S_P steers i_L to v_{BAT} to pre-charge C_{PZ} to $-v_{PC}$ and charge v_{BAT}

with whatever energy remains. v_{PZ} at 10 ms therefore collapses to zero and pre-charges to $+v_{PC}$. After this, i_{PZ} charges C_{PZ} another $\Delta v_{PZ(OC)}$ across i_{PZ}'s positive half cycle to $v_{PC} + \Delta v_{PZ(OC)}$, after which the sequence repeats.

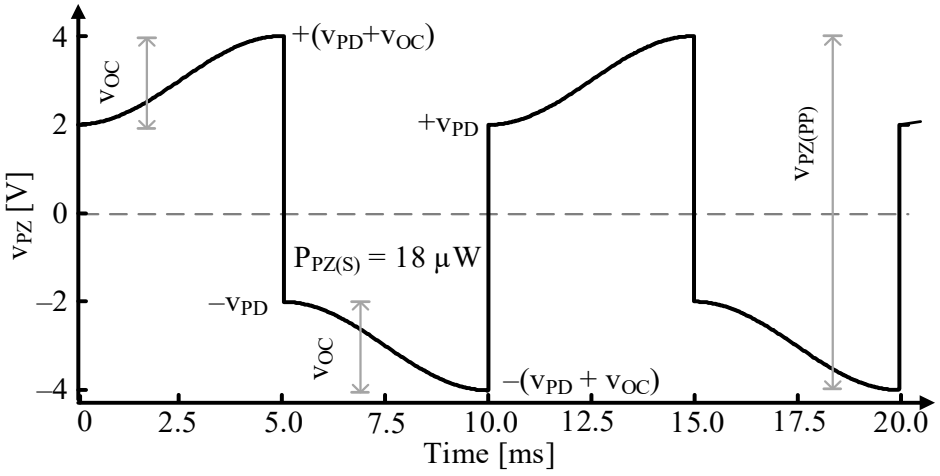

Figure 3-3. Symmetrically pre-charged piezoelectric voltage.

Since the operation is symmetrical, the peak voltage of the positive and negative direction is both $v_{PC} + \Delta v_{PZ(OC)}$. As a result, the peak-to-peak voltage $v_{PZ(PP)}$, or the total damping of the transducer, is $2(v_{PC} + \Delta v_{PZ(OC)})$.

3.1.2. Asymmetrical Pre-Charge

The bridgeless switched inductor charger in Fig. 2-16 pre-charges C_{PZ} for i_{PZ}'s negative half cycle, but not for i_{PZ}'s positive counterpart. In other words, like the dashed trace in Fig. 3-4 shows, i_{PZ} charges C_{PZ} across i_{PZ}'s positive half cycle to charge C_{PZ} to $\Delta v_{PZ(OC)}$. Battery switch S_B then closes to deposit some energy into L_X. After a short connection time, S_B opens and piezoelectric switch S_{PZ} closes for less than a quarter resonance period $0.25\tau_{LC}$ to drain C_{PZ} into L_X and another $0.25\tau_{LC}$ to deliver L_X's energy back to C_{PZ}, but in the

negative direction. This way, C_{PZ}'s v_{PZ} first collapses to zero and then pre-charges to pre-charging voltage $-v_{PC}$.

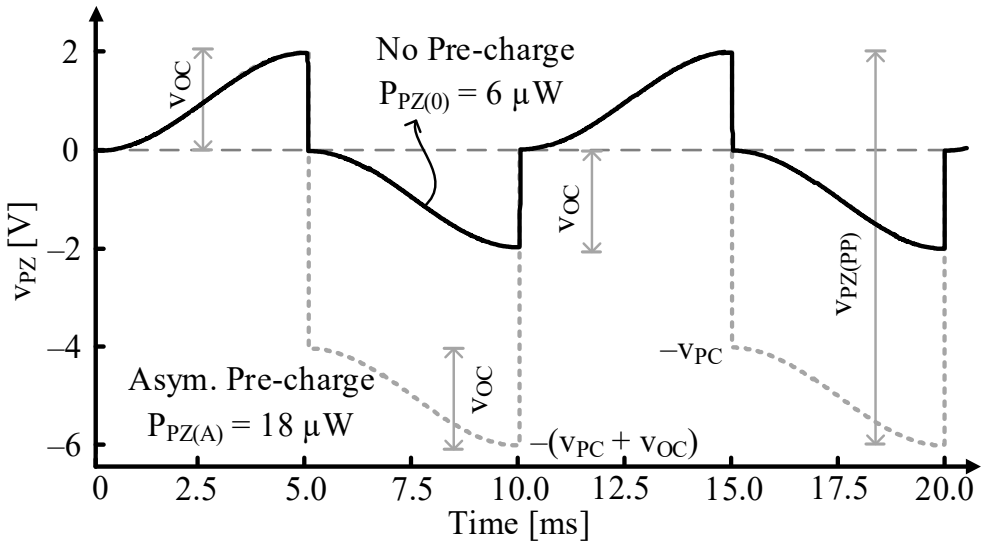

Figure 3-4. Asymmetrically pre-charged piezoelectric voltage.

Once at $-v_{PC}$, S_{PZ} opens and i_{PZ} charges C_{PZ} another $\Delta v_{PZ(OC)}$ in the negative direction to $-(v_{PC} + \Delta v_{PZ(OC)})$. S_{PZ} then closes across $0.25\tau_{LC}$ to drain C_{PZ} into L_X, and after S_{PZ} opens, S_B closes until L_X depletes into v_{BAT}.

Unlike the synchronous discharge without pre-charging or with symmetrical pre-charging, the operation here is asymmetrical. As a result, the peak voltage in the positive half cycle, $\Delta v_{PZ(OC)}$, is different from the peak voltage in the negative half cycle, $\Delta v_{PZ(OC)} + v_{PC}$. The peak-to-peak voltage $v_{PZ(PP)}$ is therefore $2\Delta v_{PZ(OC)} + v_{PC}$. Compared with the symmetrical case, the pre-charging voltage has to be twice for the asymmetrical pre-charging for the two to have the same total damping.

3.2. **Drawn Power**

3.2.1. Symmetrical Pre-charge

In synchronous discharge without pre-charge, i_{PZ} supplies $E_{PZ(1/2)}$ every half cycle:

$$E_{PZ(HALF)} = E_{C(PK)} = 0.5C_{PZ}\Delta v_{PZ(OC)}{}^2. \tag{14}$$

Pre-charging C_{PZ} to v_{PC} between half cycles allows v_{PZ} to both start and end at higher voltages. Since i_{PZ} is basically a current source, i_{PZ} delivers more energy this way, with a higher voltage. In other words, v_{PC} raises the piezoelectric damping force against which motion works to supply power. L_X therefore invests $E_{C(PC)}$ or $0.5C_{PZ}v_{PC}{}^2$ to later collect $E_{C(PK)}'$ at $0.5C_{PZ}(v_{PC} + \Delta v_{PZ(OC)})^2$, so across that half cycle, i_{PZ} delivers with $E_{PZ(1/2)}'$ the difference:

$$\begin{aligned} E_{PZ(HALF)}{}' &= E_{C(PK)}{}' - E_{C(PC)} \\ &= 0.5C_{PZ}\left[\left(v_{PC} + \Delta v_{PZ(OC)}\right)^2 - v_{PC}{}^2\right] \\ &= 0.5C_{PZ}\left(\Delta v_{PZ(OC)}{}^2 + 2\Delta v_{PZ(OC)}v_{PC}\right). \end{aligned} \tag{15}$$

This is $C_{PZ}\Delta v_{PZ(OC)}v_{PC}$ higher than its un-pre-charged counterpart. In other words, pre-charging C_{PZ} draws more energy from i_{PZ}.

In the symmetrical pre-charging scheme, before both the positive and negative half cycles, the system pre-charges the piezoelectric transducer to v_{PC}. The charger would then collect all the charge from C_{PZ} at $(v_{PC} + \Delta v_{PZ(OC)})$ at the end of the half cycles. In another word, the system invests $0.5C_{PZ}v_{PC}{}^2$ to pre-charge C_{PZ} to v_{PC} and collects $0.5C_{PZ}(v_{PC}$ +

$\Delta v_{PZ(OC)})^2$ after C_{PZ} peaks to ($v_{PC} + \Delta v_{PZ(OC)}$). As a result, $P_{PZ(S)}$ climbs with pre-charging voltage v_{PC},

$$P_{PZ(S)} = \left(E_{C(PK+)} - E_{C(PC-)} + E_{C(PK-)} - E_{C(PC+)}\right) f_{VIB}$$

$$= 0.5 C_{PZ} \left[\left(v_{PC} + \Delta v_{PZ(OC)}\right)^2 - {v_{PC}}^2 + \left(v_{PC} + \Delta v_{PZ(OC)}\right)^2 - {v_{PC}}^2\right] f_{VIB} \qquad (16)$$

$$= C_{PZ}\left({\Delta v_{PZ(OC)}}^2 + 2\Delta v_{PZ(OC)} v_{PC}\right) f_{VIB}.$$

Since the system draws more power with higher pre-charge voltages, $P_{PZ(S)}$ peaks when v_{PC} is as high as possible. In the symmetrical case, v_{PZ} swings across $v_{PZ(PP)}$ from ($v_{PC} + \Delta v_{PZ(OC)}$) to –($v_{PC} + \Delta v_{PZ(OC)}$), which means C_{PZ} exposes S_{PZ} to 2($v_{PC} + \Delta v_{PZ(OC)}$) and $P_{PZ(S)}$ maxes when $v_{PZ(PP)}$ is near S_{PZ}'s breakdown V_{BD}:

$$v_{PZ(PP)} = 2\left(v_{PC} + \Delta v_{PZ(OC)}\right) \leq V_{BD}. \qquad (17)$$

Rewrite (16) in in terms of $v_{PZ(PP)}$,

$$\begin{aligned} P_{PZ(S)} &= C_{PZ}\left({\Delta v_{PZ(OC)}}^2 + 2\Delta v_{PZ(OC)} v_{PC}\right) \\ &= C_{PZ}\left[{\Delta v_{PZ(OC)}}^2 + \Delta v_{PZ(OC)}\left(v_{PZ(PP)} - 2\Delta v_{PZ(OC)}\right)\right] \\ &= C_{PZ}\left(\Delta v_{PZ(OC)} v_{PZ(PP)} - {\Delta v_{PZ(OC)}}^2\right) \\ &\leq C_{PZ}\left(\Delta v_{PZ(OC)} V_{BD} - {\Delta v_{PZ(OC)}}^2\right). \end{aligned} \qquad (18)$$

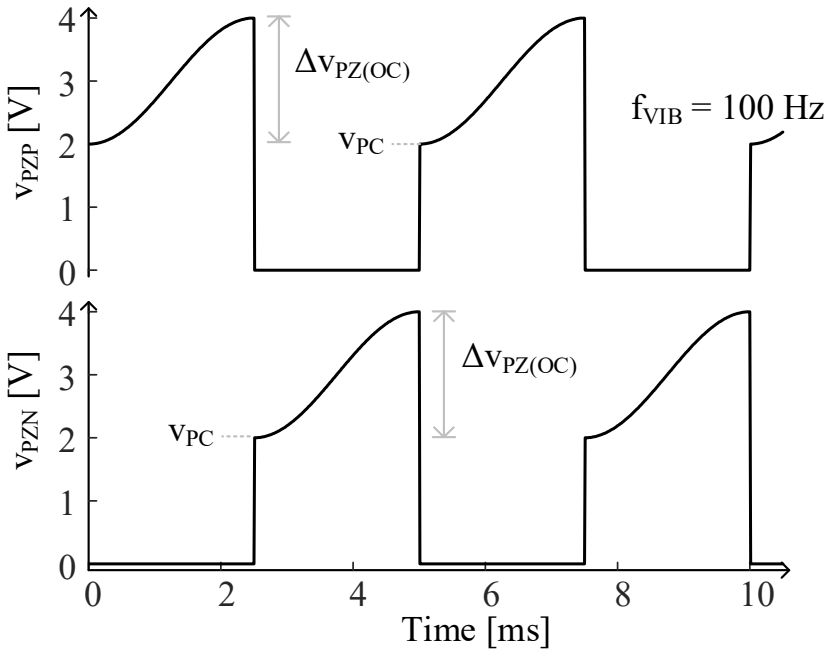

Figure 3-5. Piezoelectric voltage for the positive and negative plate with bridge-based charger.

Equation (17) would be the breakdown limit if one plate of the piezoelectric transducer is always connected to ground, and the other plate swings from the negative peak to the positive peak. However, if a bridge type rectifier is used to always connect the plate of the transducer with lower voltage potential to ground, there would not be a negative voltage in the system. As Fig. 3-5 depicts, the negative plate of the transducer, v_{PZN}, is connected to ground in the positive half cycle (0 – 2.5 ms), and the positive plate, v_{PZP}, is charged from the pre-charging voltage v_{PC} to the peak voltage $v_{PC} + \Delta v_{PZ(OC)}$. In the negative half cycle (2.5 – 5.0 ms), v_{PZP} is connected to ground, and v_{PZN} is charged from the pre-charging voltage v_{PC} to the peak voltage $v_{PC} + \Delta v_{PZ(OC)}$. With no negative voltage in the system, there is no need of the negative supply. More importantly, all the voltage nodes in the system only swing from 0 to $v_{PC} + \Delta v_{PZ(OC)}$. As a result, the breakdown voltage limit becomes

$$v_{PZ(P)} = v_{PC} + \Delta v_{PZ(OC)} \leq V_{BD}. \tag{19}$$

With the limit in (19), drawn power under breakdown limit becomes

$$\begin{aligned} P_{PZ(S)} &= C_{PZ}\left(\Delta v_{PZ(OC)}{}^2 + 2\Delta v_{PZ(OC)} v_{PC}\right) \\ &= C_{PZ}\left[\Delta v_{PZ(OC)}{}^2 + 2\Delta v_{PZ(OC)}\left(v_{PZ(P)} - \Delta v_{PZ(OC)}\right)\right] \\ &= C_{PZ}\left(2\Delta v_{PZ(OC)} v_{PZ(P)} - \Delta v_{PZ(OC)}{}^2\right) \\ &\leq C_{PZ}\left(2\Delta v_{PZ(OC)} V_{BD} - \Delta v_{PZ(OC)}{}^2\right). \end{aligned} \tag{20}$$

This is $0.5C_{PZ}\Delta v_{PZ(OC)}V_{BD}$ higher than the breakdown limit when the peak-to-peak voltage has to be below the breakdown in (18). When the vibration is low, which is the common for tiny piezoelectric transducers, the open circuit voltage $\Delta v_{PZ(OC)}$ is much less than the breakdown voltage, the difference is nearly 2×. Therefore, a bridge-based power stage that connects the piezoelectric plate with lower potential to ground can significantly improve drawn power in the symmetrical pre-charging scheme.

3.2.2. Asymmetrical Pre-Charge

In the asymmetrical pre-charging power stage, the charger pre-charges C_{PZ} to $-v_{PC}$ before the negative half cycle begins, and collect all the charge from C_{PZ} at $-(v_{PC} + \Delta v_{PZ(OC)})$ at the end. In other words, the system invests $0.5C_{PZ}v_{PC}{}^2$ to pre-charge C_{PZ} to v_{PC} and collects $0.5C_{PZ}(v_{PC} + \Delta v_{PZ(OC)})^2$ after C_{PZ} peaks to $-(v_{PC} + \Delta v_{PZ(OC)})$. In addition to the power $0.5C_{PZ}\Delta v_{PZ(OC)}{}^2$ that the charger collects after C_{PZ} peaks to $\Delta v_{PZ(OC)}$ at the end of the positive half cycle, it draws $P_{PZ(A)}$

$$P_{PZ(A)} = \left(E_{C(PK+)} - E_{C(PC)} + E_{C(PK-)}\right) f_{VIB}$$

$$= 0.5 C_{PZ} \left[\Delta v_{PZ(OC)}{}^2 - v_{PC}{}^2 + \left(v_{PC} + \Delta v_{PZ(OC)}\right)^2\right] f_{VIB} \quad (21)$$

$$= C_{PZ}\left(\Delta v_{PZ(OC)}{}^2 + \Delta v_{PZ(OC)} v_{PC}\right) f_{VIB}.$$

Since the system draws more power with higher pre-charging voltages, $P_{PZ(A)}$ peaks when v_{PC} is as high as possible. However, because the switching node v_{SW} is exposed to both the positive peak and the negative peak voltage of the piezoelectric transducer, which is another way of saying v_{SW} has a swing of $v_{PZ(PP)}$, the breakdown voltage V_{BD} has to be at least $v_{PZ(PP)}$. In a lossless charger, the breakdown voltage sets the maximum drawn power for the asymmetric pre-charging charger. $P_{PZ(A)}$ therefore maxes when $v_{PZ(PP)}$ is near S_{PZ}'s breakdown level V_{BD}:

$$v_{PZ(PP)} = \Delta v_{PZ(OC)} + \left(v_{PC} + \Delta v_{PZ(OC)}\right) = v_{PC} + 2\Delta v_{PZ(OC)} \leq V_{BD}. \quad (22)$$

Rewrite (19) in the terms of $v_{PZ(PP)}$,

$$\begin{aligned} P_{PZ(A)} &= C_{PZ}\left(\Delta v_{PZ(OC)}{}^2 + \Delta v_{PZ(OC)} v_{PC}\right) \\ &= C_{PZ}\left[\Delta v_{PZ(OC)}{}^2 + \Delta v_{PZ(OC)}\left(v_{PZ(PP)} - 2\Delta v_{PZ(OC)}\right)\right] \\ &= C_{PZ}\left(\Delta v_{PZ(OC)} v_{PZ(PP)} - \Delta v_{PZ(OC)}{}^2\right) \\ &\leq C_{PZ}\left(\Delta v_{PZ(OC)} V_{BD} - \Delta v_{PZ(OC)}{}^2\right). \end{aligned} \quad (23)$$

So when t_{VIB} is 10 ms, C_{PZ} is 15 nF, $\Delta v_{PZ(OC)}$ is 2 V, and V_{BD} is 20 V, v_{PC} should be 16 V for $P_{PZ(A)}$ to peak to 54 μW, which is 9× higher than $P_{PZ(0)}$'s 6 μW without pre-charging in Fig. 3-1.

Interestingly, Equation (23) is the same as (18). This means that if both symmetrical pre-charging power stage and its asymmetrical counterpart is subjected to the same peak to peak voltage, the maximum drawn power is the same. However, in a bridged symmetrical pre-charging power stages like the ones in Fig. 2-14 and Fig. 2-15, the bridge structure always connects the negative plate of the transducer to ground, and therefore not a single node sees the negative voltage. Therefore, the breakdown voltage only needs to be no less than the positive peak voltage, which is $v_{PC} + \Delta v_{PZ(OC)}$. If similar breakdown requirements is for the asymmetric scheme, the breakdown voltage has to be higher than the negative peak voltage

$$v_{PZ(NP)} = \left(v_{PC} + \Delta v_{PZ(OC)}\right) = v_{PC} + \Delta v_{PZ(OC)} \leq V_{BD}. \tag{24}$$

The drawn power from (21) becomes

$$\begin{aligned} P_{PZ(A)} &= C_{PZ}\left(\Delta v_{PZ(OC)}{}^2 + \Delta v_{PZ(OC)} v_{PC}\right) \\ &= C_{PZ}\left[\Delta v_{PZ(OC)}{}^2 + \Delta v_{PZ(OC)}\left(v_{PZ(NP)} - \Delta v_{PZ(OC)}\right)\right] \\ &= C_{PZ}\left(\Delta v_{PZ(OC)} v_{PZ(NP)}\right) \\ &\leq C_{PZ}\left(\Delta v_{PZ(OC)} V_{BD}\right). \end{aligned} \tag{25}$$

This is just slightly higher than the drawn voltage with peak-to-peak breakdown limit. This is understandable because the operation is asymmetrical, and the majority of the voltage is

in the negative direction. Only a small fraction of extra voltage becomes available to the charger when the breakdown limit is relaxed to only the negative direction, and the drawn power improvement is not as significant as the symmetrical case.

In conclusion, both symmetrical and asymmetrical pre-charging draws the same power when they have the same peak to peak voltage. However, symmetrical pre-charging can enjoy a nearly 2× improvement in drawn power if the charger adopts a bridge-based power stage and connects the lower voltage of the plate to the ground, by asymmetrical charger only sees incremental improvement. As a result, symmetrical pre-charging scheme with a bridge-based power stage can draw more power under the same breakdown voltage than the asymmetrical counterpart.

3.3. **Maximum Output Power**

Unfortunately not all the power that the charger draws from the transducer can reach the battery. The inductor' and power switches' equivalent series resistance consumes ohmic power. To turn the switches on and off requires gate charge loss, and the gate driver also suffers from shoot through loss. The controller consumes quiescent power. All these power losses need to be taken into consideration for the charger to output the maximum power to the battery.

3.3.1. Symmetric Pre-Charge

3.3.1.A. Ohmic Loss

Harvesting chargers use inductors to transfer energy because the mV's that their switches drop consume little power [145]. To keep these losses as low as possible, an inductor L_X

should carry more energy $0.5L_X i_L^2$ with less current i_L. For this, L_X should be high, and as a result, so should the number of turns and cross-sectional area of the winding [146].

For volts to induce no more than 100 mA within microseconds, L_X should be hundreds of μH. The winding must therefore incorporate many turns, which in small form factors only a thin coil can accommodate. Unfortunately, because thinner coils are more resistive, the equivalent series resistance R_{ESR} of tiny off-chip 100–500-μH inductors is typically high at 1–5 Ω.

For perspective, CMOS switches dissipate the least power when sized to balance ohmic and gate-drive losses. Modern switches balance these losses when their resistances R_{MOS} are less than 100 mΩ [147]. But since R_{ESR} is so much greater than R_{MOS}, R_{ESR} power overwhelms that of R_{MOS}, and by translation, that of gate drive. So R_{ESR} power P_R normally dominates all other losses to dictate what fraction of piezoelectric power P_{PZ} the battery v_{BAT} ultimately receives.

Capacitor Transfer: Before delivering energy, L_X holds energy $E_{L(PK)}$ with peak inductor current $i_{L(PK)}$. When connected to a capacitor C_X, L_X and C_X exchange $E_{L(PK)}$ every quarter cycle of their resonance period τ_{LC}

$$\tau_{LC} = 2\pi\sqrt{L_X C_X}\,. \tag{26}$$

Since L_X's i_L is nearly sinusoidal through this time, as the dashed trace in Fig. 3-6 shows, i_L's root–mean–square (RMS) current is

$$i_{L(RMS.SINE)} = \sqrt{\frac{1}{0.25\tau_{LC}} \int_{0}^{0.25\tau_{LC}} \left[i_{L(PK)} \sin\left(\frac{2\pi t}{\tau_{LC}}\right)\right]^2 dt} = \frac{i_{L(PK)}}{\sqrt{2}}. \quad (27)$$

So to transfer $E_{L(PK)}$, L_X's ohmic power $P_{R(C)}$ across vibration period t_{VIB} is a $0.25\tau_{LC}/t_{VIB}$ fraction of RMS power across τ_{LC}, where t_{VIB} is usually long at 1–1000 ms [10]:

$$P_{R(C)} \approx {i_{L(RMS)}}^2 R_{ESR} \left(\frac{0.25\tau_{LC}}{t_{VIB}}\right) = \left(\frac{i_{L(PK)}}{\sqrt{2}}\right)^2 R_{ESR} \left(\frac{0.5\pi\sqrt{L_X C_X}}{t_{VIB}}\right). \quad (28)$$

$P_{R(C)}$ therefore climbs with ${i_{L(PK)}}^2$, and since L_X transfers $0.5L_X{i_{L(PK)}}^2$, with L_X's peak energy packet $E_{L(PK)}$.

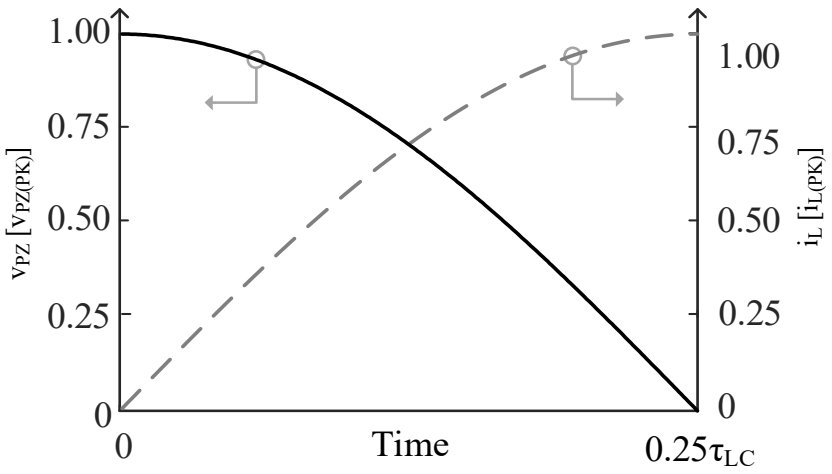

Figure 3-6. A quarter cycle of the sinusoidal transfer between C_{PZ} and L_X.

Partial Capacitor Transfer: C_X's voltage v_C is, like i_L, sinusoidal. So when transferring part of L_X's energy, time t_X, as shown in Fig. 3-7, lapses the sinusoidal fraction of the resonance period τ_{LC} that v_C requires to reach the $v_{C(X)}$ fraction of peak voltage $v_{C(PK)}$:

$$t_X \approx \left(\frac{\tau_{LC}}{2\pi}\right)\sin^{-1}\left(\frac{v_{C(X)}}{v_{C(PK)}}\right). \tag{29}$$

Since L_X's energy and i_L peak when C_X's energy and v_{PZ} are zero, i_L is the cosine counterpart of v_C:

$$i_L = i_{L(PK)}\cos\left[2\pi\left(\frac{t}{\tau_{LC}}\right)\right]. \tag{30}$$

So to transfer a t_X sinusoidal fraction of L_X's $E_{L(PK)}$ at $i_{L(PK)}$, L_X's ohmic power $P_{R(X)}$ across t_{VIB} is

$$\begin{aligned} P_{R(CX)} &\approx {i_{L(RMS)}}^2 R_{ESR}\left(\frac{t_X}{t_{VIB}}\right) = \left[\left(\frac{1}{t_X}\right)\int_0^{t_X} {i_L}^2 dt\right] R_{ESR}\left(\frac{t_X}{t_{VIB}}\right) \\ &= \left(\frac{{i_{L(PK)}}^2}{t_{VIB}}\right)\left\{\frac{t_X}{2} + \left(\frac{\tau_{LC}}{8\pi}\right)\sin\left[4\pi\left(\frac{t_X}{\tau_{LC}}\right)\right]\right\} R_{ESR}. \end{aligned} \tag{31}$$

So like $P_{R(C)}$, $P_{R(CX)}$ climbs with ${i_{L(PK)}}^2$ and L_X's $E_{L(PK)}$.

Battery Transfer: Since L_X's voltage is constant at v_{BAT} when transferring $E_{L(PK)}$ to v_{BAT}, i_L falls linearly to zero across t_{BAT} connection time $L_X i_{L(B)}/v_{BAT}$, as shown by the dashed trace after t_X in Fig 3-5. RMS current $i_{L(RMS)}$ across t_{BAT} is therefore $i_{L(B)}/\sqrt{3}$ and L_X's ohmic power $P_{R(B)}$ across vibration period t_{VIB} is a t_{BAT}/t_{VIB} fraction of RMS power across t_{BAT}:

$$P_{R(B)} \approx {i_{L(RMS)}}^2 R_{ESR}\left(\frac{t_{BAT}}{t_{VIB}}\right) = \left(\frac{i_{L(B)}}{\sqrt{3}}\right)^2 R_{ESR}\left(\frac{L_X i_{L(B)}}{v_{BAT} t_{VIB}}\right). \tag{32}$$

$P_{R(B)}$ therefore climbs with $i_{L(B)}^3$, which is faster than $P_{R(C)}$ and $P_{R(CX)}$ rise with L_X's peak energy $E_{L(PK)}$.

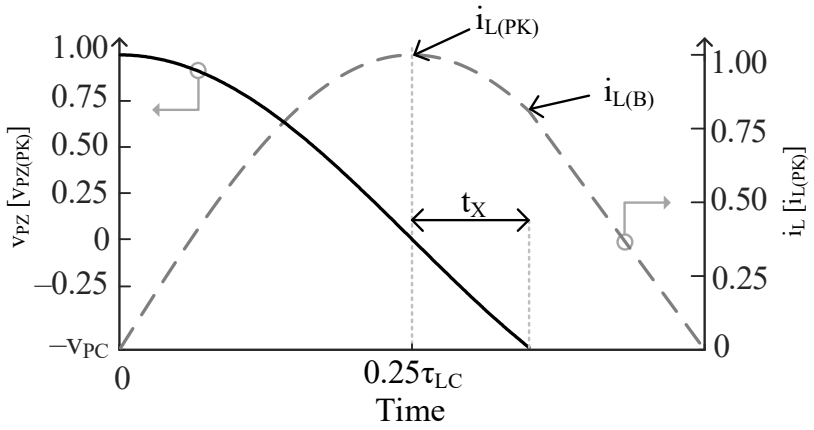

Figure 3-7. The capacitor voltage and inductor current of a quarter cycle transfer, a partial capacitor transfer, and battery transfer.

3.3.1.B. Other Losses

Aside from ohmic losses, the charger also consumes other types of losses. For example, the MOSFET switches require charge to switch them on and off. For a perfectly optimized MOSFET switch, however, the charge loss is the same as the ohmic loss. Combined with the fact that tiny inductors are more resistive than integrated MOSFET switches, the ohmic loss overwhelms the charge loss. The MOSFET switches also consumes leakage power when they are supposed to be turned off. However, the off resistance for MOSFET are in the range of GΩ under room temperature, and still in the order of 100 MΩ at 125°C, and the leakage power is in the order of nW. Since the piezoelectric charger generates and outputs 10s of microwatt, the leakage loss can be neglected.

Charger also requires quiescent power to control the switching sequence to draw and output power and to maintain maximum power point. From reported power stages, the

quiescent power can range from 100 nW to 5 μW, which can be higher than the ohmic loss. However, since the symmetrical and asymmetrical power stages all require the same synchronization and MPP logics, the quiescent power loss should be the same. Therefore, the rest of this chapter compares the ohmic loss only to determine the best charger.

3.3.1.C. Symmetric Pre-Charge Output Power

The symmetrical pre-charge charger loses power with every energy transaction, mostly to R_{ESR}. The piezoelectric voltage v_{PZ} and inductor current i_L for the symmetrical pre-charge charger is exactly the same as Fig. 3-7 every half cycle. The peak voltage is $v_{PC} + \Delta v_{PZ(OC)}$, and initially the capacitor holds energy $E_{PZ(PK)}$

$$E_{PZ(PK)} = 0.5C_{PZ}\left(v_{PC} + \Delta v_{PZ(OC)}\right)^2. \tag{33}$$

It has a quarter cycle LC transfer, a partial quarter cycle LC transfer, and a battery transfer. After the quarter cycle LC transfer, the inductor receives almost all of the energy from C_{PZ}

$$E_{L(PK)} = 0.5L_X i_{L(PK)}{}^2 \approx E_{PZ(PK)} = 0.5C_{PZ}\left(v_{PC} + \Delta v_{PZ(OC)}\right)^2. \tag{34}$$

Because from (24), the ohmic loss for the quarter LC transfer is proportional to $i_{L(PK)}{}^2$, the ohmic loss for the quarter LC transfer is also proportional to the energy transferred. As a result, the more pre-charging voltage we put into C_{PZ} before a half cycle, the more ohmic power is lost.

The partial quarter LC transfer recycles some of the energy from the previous half cycle to pre-charge the next half cycle. From (27), the ohmic loss on the partial LC transfer is also proportional to $i_{L(PK)}{}^2$. It also rises with partial transfer time tX, which from (25) also rises with pre-charging voltage v_{PC}. As result and similar to the quarter LC cycle, it also rises with pre-charging voltage, with a faster rate of change. Yet because it only a portion of the quarter cycle transfer, the ohmic loss is always lower than that in the quarter cycle transfer.

After the partial LC transfer, the inductor puts the pre-charging energy E_{PC} back into C_{PZ}, and with the remaining energy going into the battery

$$E_{L(B)} = 0.5 L_X i_{L(B)}{}^2$$

$$\approx E_{L(PK)} - E_{PC} = 0.5 C_{PZ}\left(v_{PC} + \Delta v_{PZ(OC)}\right)^2 - 0.5 C_{PZ} v_{PC}{}^2 \qquad (35)$$

$$= 0.5 C_{PZ}\left(\Delta v_{PZ(OC)}{}^2 + 2\Delta v_{PZ(OC)} v_{PC}\right).$$

As a result, $i_{L(B)}$ rises with v_{PC}. The battery transfer, on the other hand, rises with $i_{L(B)}{}^3$. Yet the energy that the battery receives rises with $i_{L(B)}{}^2$.Therefore, the battery transfer climbs faster than the total energy transferred.

So R_{ESR} burns power between every half cycle when L_X drains C_{PZ}, L_X pre-charges C_{PZ}, and L_X charges v_{BAT}. These losses climb with L_X's transfer energy $E_{L(PK)}$, and as a result, with L_X's $i_{L(PK)}$. Although P_R for battery transactions rises more quickly (with $i_{L(B)}{}^3$) than for capacitor transactions (with $i_{L(PK)}{}^2$), v_{BAT} does not invest energy to raise v_{PC}. And

because all three transfers take about the same transfer time, and with similar RMS current, all three losses are close to each other, as shown in Fig. 3-8.

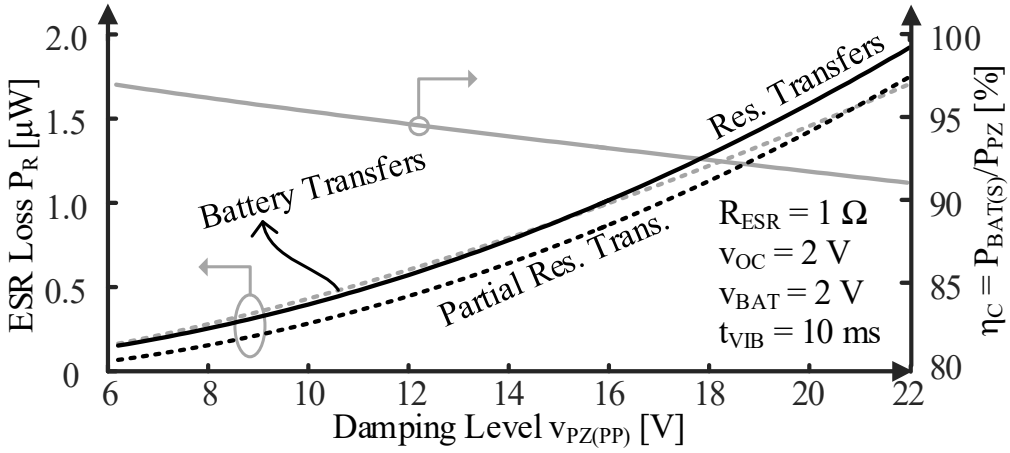

Figure 3-8. Simulated ohmic conduction losses and power-conversion efficiency.

Because the losses increase faster than the total energy transferred, eventually increasing v_{PC} further results in more additional losses than drawn power. The pre-charging voltage $v_{PC(MPP)}$, and the resulting $v_{PP(MPP)}$, corresponds to the point where the gain in drawn power is exactly the same as the gain in losses. This is where the charger can output the most power. Because it is the ohmic loss that limit how much the charger can output, it's called loss-limited. If the charger hits the breakdown before reaching the loss limited v_{PC}, the system would become breakdown limited. The maximum output power would therefore be determined by the drawn power, losses, and breakdown voltage.

The black solid trace in Fig. 3-9 shows that the symmetrical pre-charge's output power keeps rising under the 0 – 22 V peak-to-peak range. Simulation shows that output power peaks at 255 µW when the peak-to-peak voltage is 176 V, but that would be beyond the breakdown voltage of most CMOS and MEMS technology. Overall, the output power

is always higher than its asymmetrical counterpart, and should be favored whenever it's available.

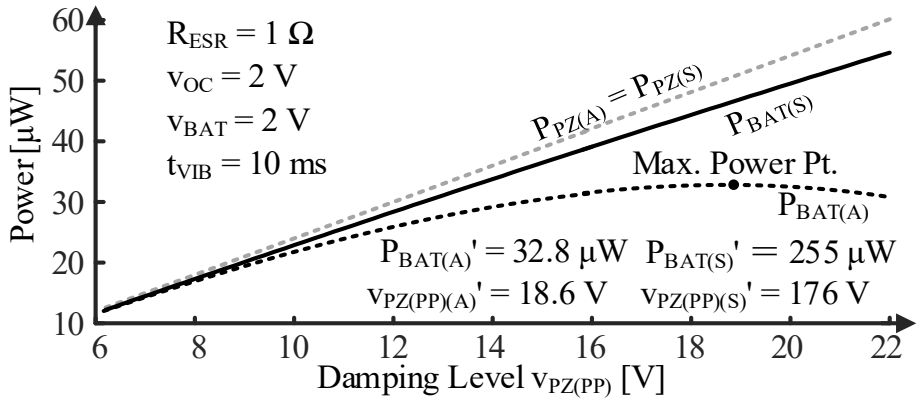

Figure 3-9. Simulated drawn piezoelectric and received battery power.

3.3.2. Asymmetrical Pre-Charge

The asymmetrical pre-charge power stage differs from the symmetrical one in that it needs assist from the battery to pre-charge in the negative half cycle. As Fig. 3-10 shows, across the investing time t_{INV}, the inductor receives energy from the battery.

$$E_{INV} = 0.5 L_X i_{L(INV)}^2. \quad (36)$$

This is equivalent to the battery transfer in the symmetrical case, and the ohmic power rises with $i_{L(INV)}^3$.

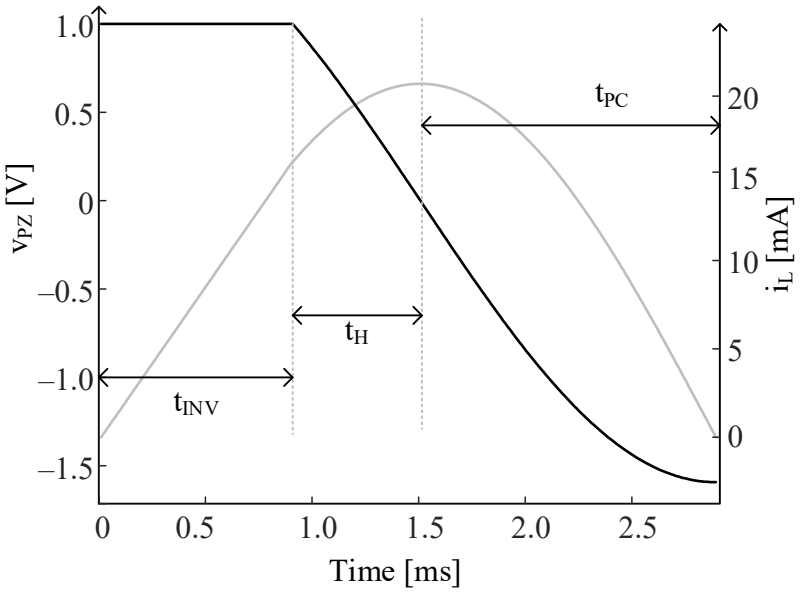

Figure 3-10. Piezoelectric voltage and inductor current at the end of the positive half cycle in an asymmetrical pre-charging power stage.

After the investment, the inductor collects the charge from C_{PZ} from the positive half cycle across t_H, and peaks at $E_{L(PK)}$

$$E_{L(PK)} = 0.5 L_X {i_{L(PK.P)}}^2 \approx E_{L(INV)} + E_{C(PK,P)} = 0.5 L_X {i_{L(INV)}}^2 + 0.5 C_{PZ} {\Delta v_{PZ(OC)}}^2. \quad (37)$$

This transfer is a partial LC transfer, and the ohmic loss is proportional to ${i_{L(PK.P)}}^2$, and also rises partial transfer time t_H. The next part of the transfer pre-charges the transducer to $-v_{PC}$. It is a quarter LC transfer across pre-charging time t_{PC}, and the ohmic loss is proportional to ${i_{L(PK)}}^2$.

Across the negative half cycle, the vibration charges C_{PZ} from $-v_{PC}$ to $-(v_{PC} + \Delta v_{PZ(OC)})$, with energy $0.5C_{PZ}(v_{PC} + \Delta v_{PZ(OC)})^2$. At the end of the negative half cycle, the inductor collector all the charge from the transducer

$$E_{L(PK.N)} = 0.5L_X i_{L(PK.N)}{}^2 \approx 0.5C_{PZ}\left(v_{PC} + \Delta v_{PZ(OC)}\right)^2 \tag{38}$$

The transaction takes a quarter LC cycle, and the ohmic loss is proportional to $i_{L(PK.N)}{}^2$, and as a result, proportional to $E_{L(PK.N)}$. The quarter LC cycle has larger peak inductor current because of the energy drawn from the negative half cycle, and with longer transfer time consumes more power than the partial cycle at the end of the positive half cycle. The inductor then drains into the battery, with the ohmic loss proportional to $i_{L(PK.N)}{}^3$.

To summarize, at the end of the positive half cycle, at 5 ms in Fig. 3-1, R_{ESR} burns power when v_{BAT} deposits energy into L_X, L_X drains C_{PZ}, and L_X pre-charges C_{PZ} to $-v_{PC}$. At the end of the other half cycle, at 10 ms, R_{ESR} similarly dissipates power when L_X drains C_{PZ} and then charges v_{BAT}. So in the end, v_{BAT} receives the difference between $P_{PZ(A)}$ and these R_{ESR} losses.

All these losses climb with L_X's transfer energy $E_{L(PK)}$, and more specifically, with L_X's $i_{L(PK)}$. But of these, P_R for battery transactions rises more quickly (with $i_{L(PK)}{}^3$) than for capacitor transactions (with $i_{L(PK)}{}^2$). And since v_{BAT}'s investment energy rises with pre-charging voltage v_{PC}, battery-transfer losses climb with $v_{PZ(PP)}$ in Fig. 3-11 more quickly than for capacitor transfers. More importantly, the net energy the battery receives is the difference between the piezoelectric energy at the end of the negative half cycle $E_{PZ(PK.N)}$ and the investment energy E_{INV}, but the battery transfer losses are the sum of the two. As

a result, battery transfer losses rises much faster than the other ones, and quickly catches up to the gain of the drawn power with increased pre-charging voltage. So much so that losses outpace $P_{PZ(PD)}$ gains in Fig. 3-9 when $v_{PZ(PP)}$ exceeds 18.6 V. In other words, output power into v_{BAT} peaks at $P_{BAT(A)}$' when $v_{PZ(PP)}$ is 18.6 V, at which point v_{BAT} receives 33 of $P_{PZ(A)}$'s 50 µW when R_{ESR} is 1 Ω.

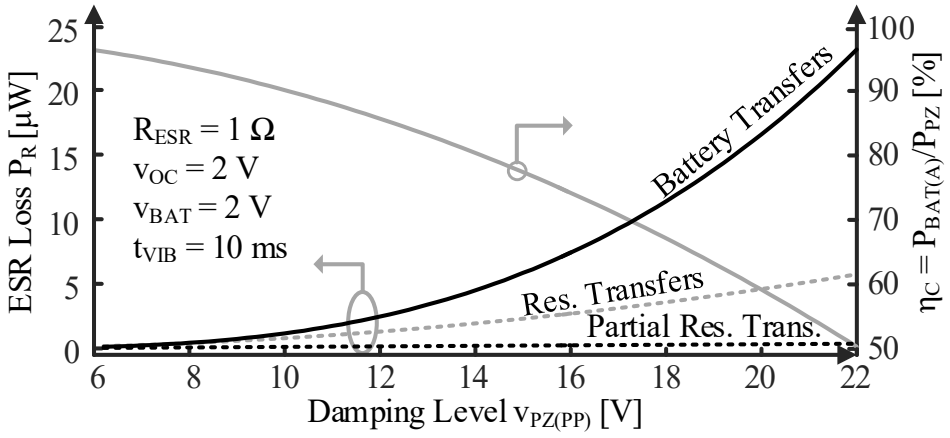

Figure 3-11. Simulated ohmic conduction losses and power-conversion efficiency.

3.4. Symmetry

The circuit in Fig. 12 is used to verify and compare symmetrical and asymmetrical pre-charges. For symmetrical pre-charges, switches S_{I+}, S_{I-}, and S_{GI-} first close after positive peak to energize L_X while draining C_{PZ} (0 to 2.1 µs in Fig.). Switches S_{I+}, S_{I-}, and S_{GI+} then closes to pre-charge v_{PZ} to $-v_{PC}$ (2.1 to 3.2 µs). The inductor would then charge the battery through switches S_{G+} and S_{O-} (3.5 to 4.5 µs). Since the circuit is fully symmetrical, the same sequence by replacing the switches in the top half by the bottom half repeats.

For asymmetrical pre-charges, the charger only recycles at the end of the positive half cycle, by closing switches S_{I+}, S_{I-}, and S_{GI-} to energize L_X while draining C_{PZ} (0 to 2.1 µs of the dotted line in Fig. 13), and by closing switches S_{I+}, S_{I-}, and S_{GI+} to drain L_X

while pre-charging C_{PZ} (2.1 to 4.2 µs of the dotted line in Fig.). At the end of the negative half cycle, switches S_{I+}, S_{I-}, and S_{GI+} close to energize L_X while draining C_{PZ} (0 to 2.1 µs of the dotted line in the right part of Fig. 13), and then the inductor charge the battery through switches S_{G-} and S_{O+} (3.5 to 4.5 µs). This asymmetrical pre-charge scheme differs from the state of the art in that it does not invest battery voltage to arbitrarily raise pre-charging voltage, and that each energy transfer would flow through multiple switches. However, because all the voltage nodes in the power stage is only exposed to positive voltage, the breakdown limit is relaxed.

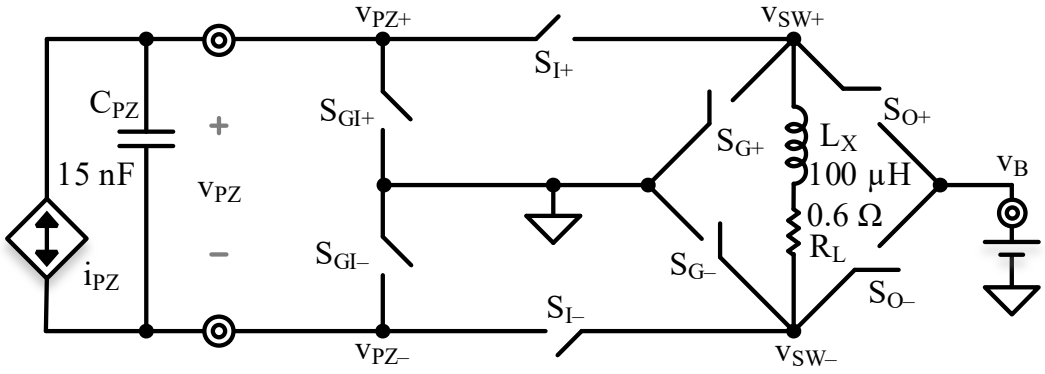

Figure 3-12. Circuit to compare symmetrical and asymmetrical pre-charging.

In the asymmetrical pre-charge case, the peak voltage in the negative half cycle $2\Delta v_{PZ(OC)}$ has to be below V_{BD}. If the vibration produces a $\Delta v_{PZ(OC)}$ stronger than $0.5V_{BD}$, the state-of-the-art charger cannot accommodate it. However, a reconfiguration of the switching sequence can keep the power stage from breaking down by putting some of the energy harvested in the positive half cycle to the battery, instead of back to C_{PZ} in the negative direction. This way, namely partial asymmetrical pre-charging, the charger can tolerate $\Delta v_{PZ(OC)}$ up to V_{BD}.

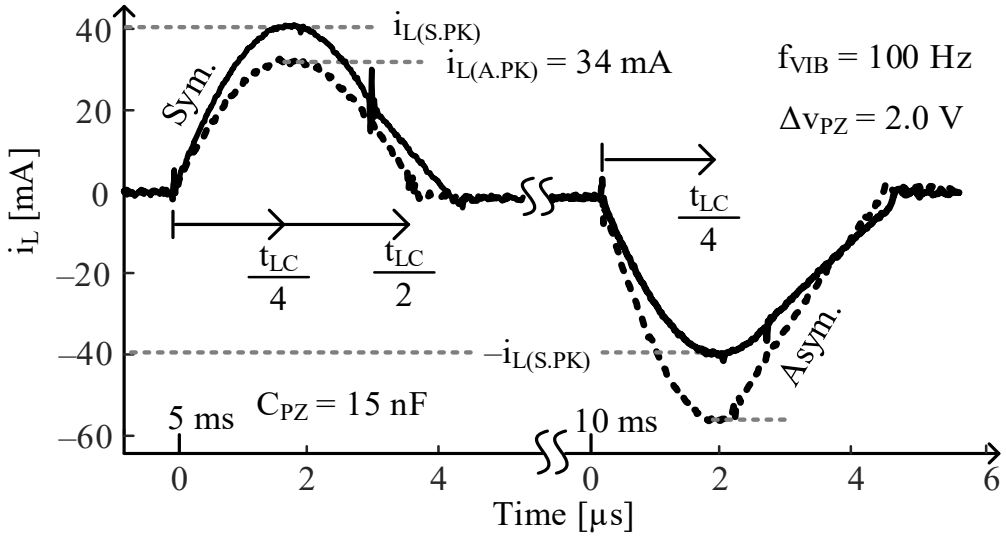

Figure 3-13. Inductor current for symmetrical pre-charge (solid trace) and asymmetrical pre-charge (dotted trace).

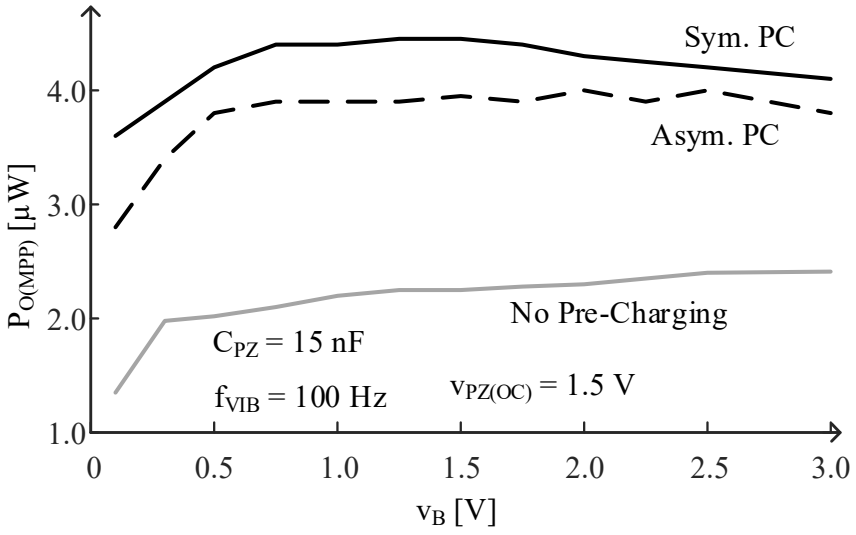

Figure 3-14. Output power for symmetry across v_B.

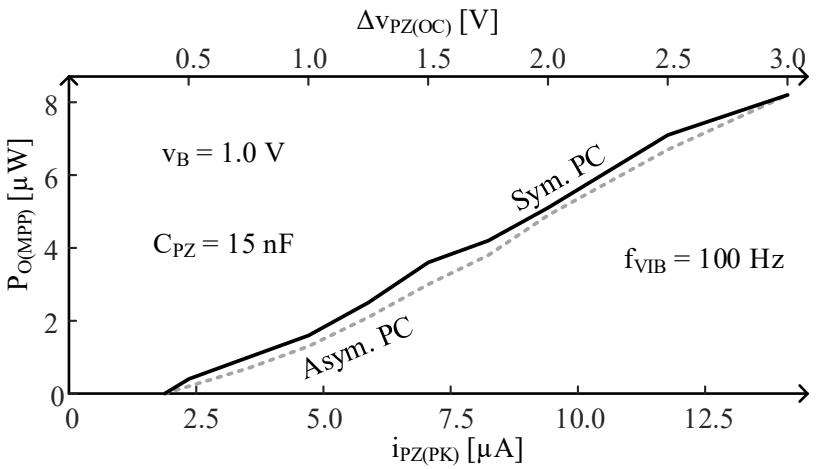

Figure 3-15 Output power for symmetry across vibration strength.

3.5. **Summary**

Piezoelectric chargers with synchronous discharges let the vibration charge the capacitor open-circuit across the half cycles, and collect all the charge between half cycles to raise drawn power. Pre-charging the transducer can further increase drawn power by charging the transducer intentionally before a half cycle starts. This way, the charge is generated at a higher voltage, resulting in higher drawn power. Symmetric and asymmetric pre-charge can both increase drawn power over non-pre-charge cases. Under the same peak to peak voltage constraint, both pre-charge schemes can draw the same maximum power. As a result, if a charger's peak-to-peak voltage has to be under the breakdown voltage, both pre-charge schemes draws the same maximum power. However, bridge-based symmetrical pre-charging can allow all nodes to be positive, relaxing the breakdown constraint by almost half. On the other hand, because ohmic loss in battery transfers rises faster than the overall power transferred, transferring two smaller energy packets every cycle loses less power than one large energy packet. Furthermore, the asymmetrical pre-charge outputs the

energy of the difference of two battery transfers, but the ohmic loss is the sum of the two, leading to much higher battery transfer loss. As a result, symmetrical pre-charge scheme is favored over its asymmetrical counterpart. Measurement from the same power stage further validates the conclusion, as symmetrical pre-charge can draw 30–80% more power than the asymmetrical case. Symmetrical pre-charge schemes should be considered to power piezoelectric microsystems for longer lifetime and broader functionality.

CHAPTER 4. ENERGY TRANSFERS

The previous chapter focuses on how to manage the piezoelectric transducer and its voltage to draw and output the most power. This chapter, on the other hand, shifts the focus on the switched-inductor. Specifically, how the inductor transfers the energy, and how to save the most power. The traditional way of transferring the energy by first energizing the inductor fully, then drain it completely is the simplest approach, but is it the best? Could there be some flaws in that scheme? Might some more carefully thought out approach save some power losses? This chapter dives deep into these issues.

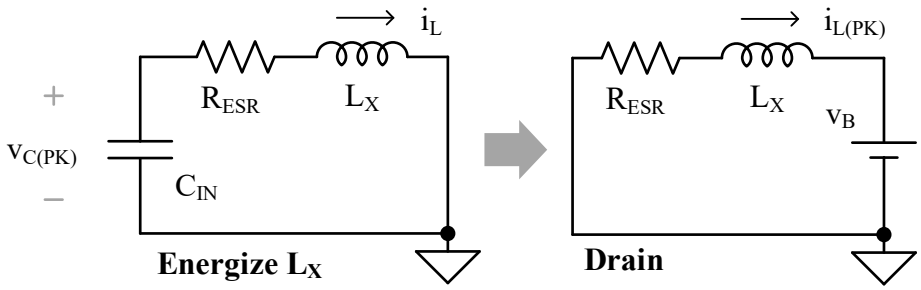

Figure 4-1. Switching configuration for energize and drain phase in an indirect-only transfer.

4.1. Indirect-Only Switched-Inductor Transfer

4.1.1. Operation

The most intuitive way to transfer energy from C_{PZ} to v_B is the indirect transfer, where the inductor L_X receives all the energy from C_{PZ}, and then transfers all the energy into v_B. Fig. 4-2 shows the inductor current in an indirect transfer with the solid gray trace. C_{PZ} is connected to L_X across 0.2 µs to 2.0 µs to transfer all its energy to L_X. L_X then is connected

to v_B from 2.0 µs to 3.1µs to charge v_B. It's called indirect because the C_{PZ} cannot directly transfer its energy to v_B.

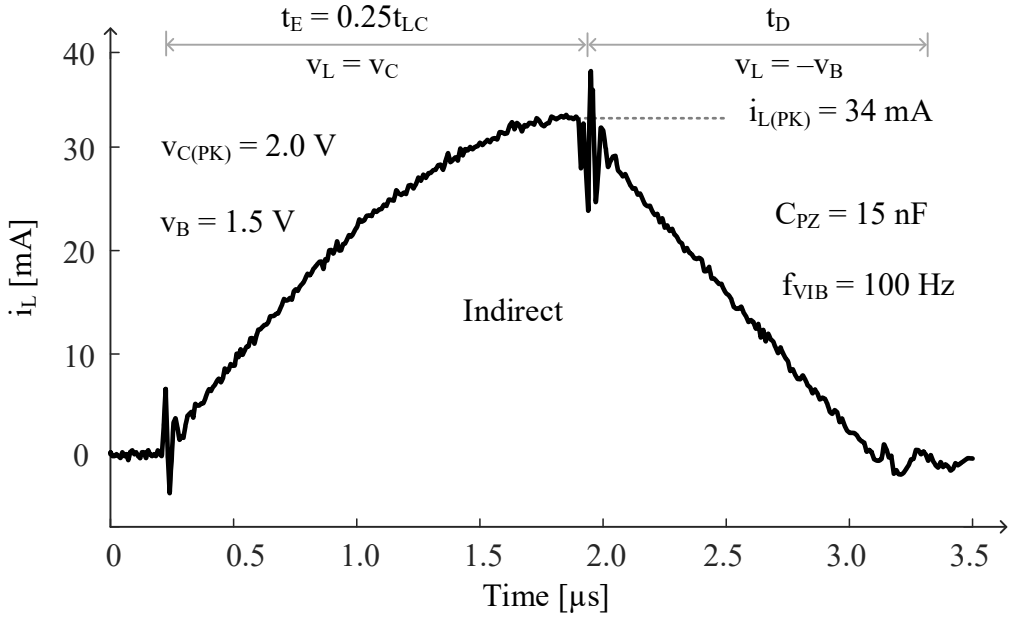

Figure 4-2. Inductor current for indirect transfers.

4.1.2. Ohmic Losses

As shown in the dashed trace in Fig. 4-2, the energizing part of the transfer is a quarter cycle of the oscillation between C_{PZ} and L_X, as i_L energizes to $i_{L(PK)}$ and v_C drains to 0:

$$E_L = 0.5L_X{i_{L(PK)}}^2 \approx E_C = 0.5C_{PZ}{v_{C(PK)}}^2 \tag{39}$$

$$i_{L(PK)} \approx \sqrt{\frac{C_{PZ}}{L_X}}v_{C(PK)}. \tag{40}$$

Therefore, the energizing time is

$$t_E = 0.25\tau_{LC} = 0.5\pi\sqrt{L_X C_{PZ}}. \quad (41)$$

Then the inductor drains linearly to the battery with a slope of v_B/L_X, and the draining time is

$$t_D = \left(\frac{L_X}{v_B}\right) i_{L(PK)}. \quad (42)$$

From the current waveform and the transfer time, we can calculate the ohmic loss on R_{ESR}:

$$E_R = R_{ESR} {i_{L(RMS)}}^2 t_X = R_{ESR}\left[\left(\frac{{i_{L(PK)}}^2}{2}\right) t_E + \left(\frac{{i_{L(PK)}}^2}{3}\right) t_D\right], \quad (43)$$

where $i_{L(RMS)}$ is the root-mean-square (RMS) current across the transfer, and t_X is the total transfer time.

4.1.3. Pre-Charge

As detailed in Chapter 3, pre-charging can significantly increase drawn and output power, which is important to power wireless microsystems. To pre-charge with indirect transfers, one simply needs to first drain C_{PZ} to charge the battery, and then invest some battery energy to pre-charge C_{PZ} in the opposite direction. As Fig. 4-3 shows, the pre-charge transfer is the complete reverse of the battery charge transfer, and therefore the transfer time and ohmic loss analysis is the same.

As explained in Chapter 3, because the piezoelectric capacitance has enough energy to pre-charge for the next cycle, the pre-charge does not require the battery assistance. After

C_{PZ} drains into L_X, L_X can energize into C_{PZ} in the opposite direction, as Fig. 4-4 shows. When C_{PZ} reaches the desired pre-charge voltage after a partial quarter LC cycle, L_X can disconnect from C_{PZ}, and the remaining current charges the battery. This way the battery does not receive energy and immediately putting part of it back into the charger, and saves a transaction. However, even though the total transaction time is shorter, the portion of the transfer during which the inductor current is high is larger. The inductor current in Fig. 4-4 stays above 8 mA for 1.72 ms after i_L peaks at 10 mA, while that in Fig. 4-3 only spends 0.61 ms in the high current region. Because ohmic loss rises quadratically with inductor current, the transfer scheme in Fig. 4-4 actually loses more ohmic power than that in Fig. 4-3. Therefore, the goal is to prioritize lower RMS current over transfer time to reduce ohmic losses.

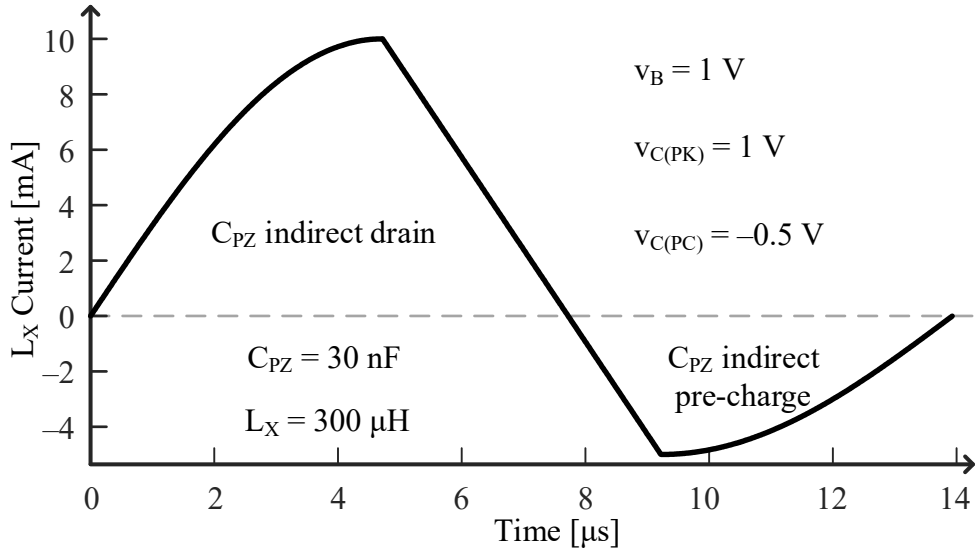

Figure 4-3. Simulated inductor current with C_{PZ} indirect drain and indirect pre-charge with battery investment.

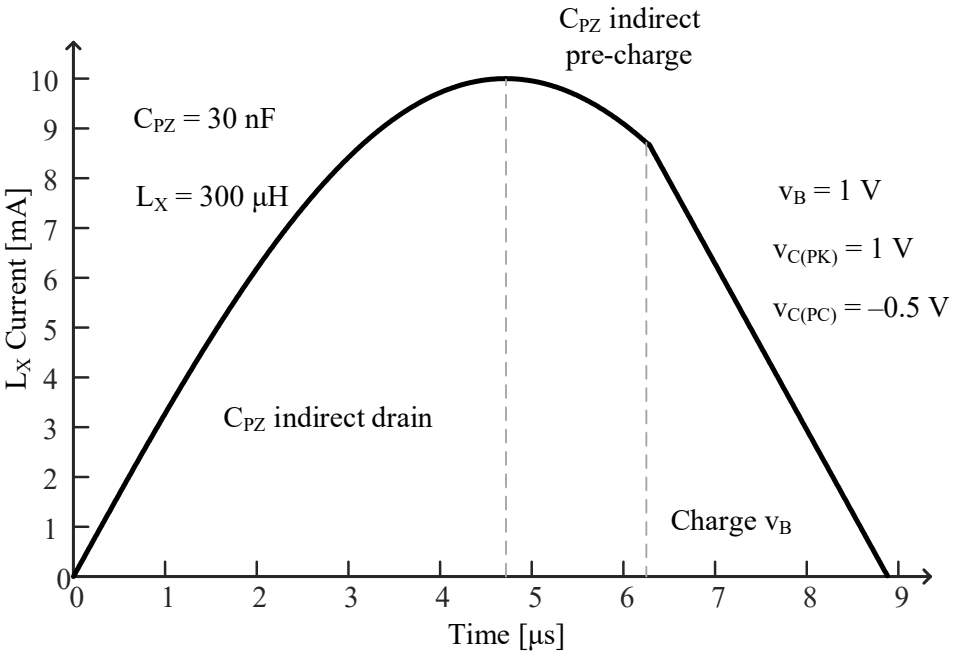

Figure 4-4. Inductor current for indirect C_{PZ} drain, pre-charge, and battery charge.

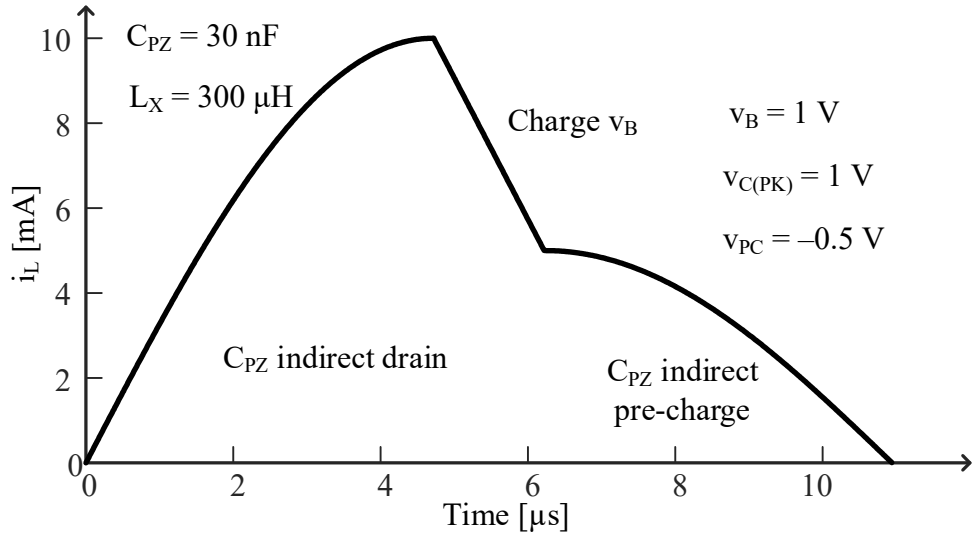

Figure 4-5. Inductor current for indirect C_{PZ} drain, battery charge, and pre-charge.

The indirect transfer shown in Fig. 4-5 does exactly that by swapping the charge v_B phase and pre-charge C_{PZ} phase. This way, inductor current quickly drops after it peaks, because the battery voltage is higher than the 0 V to v_{PC} for the piezoelectric voltage. As a

result, the inductor current only spends 0.61 ms above 8 mA after it peaks, same as that in Fig. 4-3. Even though the pre-charge now takes the entire quarter cycle, it takes place with a lower current. Overall, it loses the least ohmic power among the three ways to pre-charge with indirect transfers.

4.2. **Indirect–Direct Transfer**

4.2.1. Operation

An alternative way to transfer the energy from C_{PZ} to v_B is the indirect–direct transfer. With the switching configuration in Fig. 4-6, C_{PZ} energizes L_X indirectly, but the energizing stops before C_{PZ} is completely drained, as the solid black trace in Fig. 4-7 shows. Instead, it has initial drain voltage $v_{C(DI)}'$ when L_X starts to drain, and both C_{PZ} and L_X drain directly into the battery to finish the transfer. This portion is called direct, because C_{PZ} directly connects with the battery, and therefore transfers a portion of the energy directly. The controller controls the energizing time t_E' such that C_{PZ} and L_X hold just enough energy to drain at the same time at the end of the transfer.

4.2.2. Ohmic Losses

The inductor current in indirect–direct transfer, i_L' in the solid trace in Fig. 4-7, starts out the same as in indirect-only. However, since the energizing time t_E' is shorter, the inductor current only reaches $i_{L(PK)}'$, which is less than $i_{L(PK)}$. With a sinusoidal transfer, the energy before and after t_E' is equal:

$$E_{C(PK)} = E_{C(M.ID)} + E_{L(ID)} = 0.5C_{IN}v_{C(M.ID)}{}^2 + 0.5C_{IN}i_{L(PK.ID)}{}^2, \qquad (44)$$

where $E_{C(M.ID)}$, $E_{L(ID)}$, $v_{C(M.ID)}$, and $i_{L(PK.ID)}$ denote the transition point energy on C_{PZ}, the transition point energy on L_X, the voltage across C_{PZ} at the transition point, and the peak current on L_X in the indirect–direct transfer. The energizing time is the fraction of the cosine that drains v_C from $v_{C(PK)}$ to $v_{C(M.ID)}$,

$$v_{C(M.ID)} = v_{C(PK)} \cos\left(\frac{2\pi t_{E(ID)}}{t_{LC}}\right) \tag{45}$$

$$t_{E(ID)} = \frac{t_{LC}}{2\pi} \cos^{-1}\left(\frac{v_{C(M.ID)}}{v_{C(PK)}}\right). \tag{46}$$

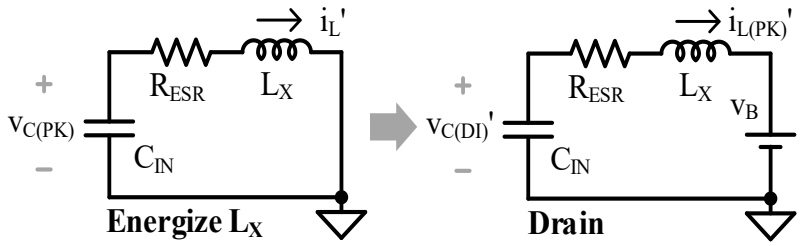

Figure 4-6. Switching configuration for energize and drain phases in an indirect–direct transfer.

Next, both C_{PZ} and L_X drain directly into v_B across drain time $t_{D(ID)}$. Fig. 4-8 depicts the voltage transfer with the solid trace, as well as its steady-state extrapolation of the oscillation between C_{PZ} and L_X with the dashed trace. The capacitor voltage v_C is a sinusoidal waveform centered around the dc voltage v_{DC} with peaks of $v_{DC} + v_{PK}$ and $v_{DC} - v_{PK}$. In this case, the dc voltage is the battery voltage, v_B, and since the negative peak is 0 V, the peak voltage of the sinusoid v_{PK} is also v_B. As v_C drains from $v_{C(M.ID)}$ to 0, the drain time t_D is the fraction of the cosine it takes to go from $v_B - v_{C(M.ID)}$ to v_B:

$$\Delta v_{C(ID)} = v_B - v_{C(M.ID)} = v_B \cos\left(\frac{2\pi t_{D(ID)}}{t_{LC}}\right) \tag{47}$$

$$t_{D(ID)} = \frac{t_{LC}}{2\pi} \cos^{-1}\left(\frac{v_B - v_{C(M.ID)}{}'}{v_B}\right). \tag{48}$$

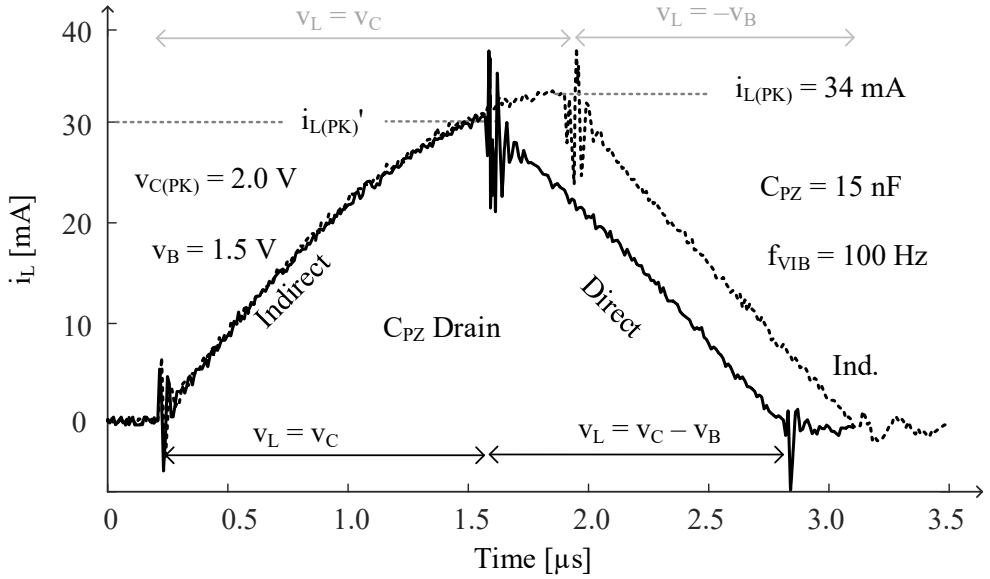

Figure 4-7. Inductor current for indirect transfer and indirect-direct transfer when draining C_{PZ}.

Note that the direct phase of the transfer starts at $0.33t_{LC}$ in Fig. 4-8 corresponds to 1.50 µs in Fig. 4-7, and ends at $0.50t_{LC}$ corresponds to 2.80 µs. Because the voltage is centered at v_B, the energy in the LC tank would also need to refer to its dc voltage. At the end of the transfer, the inductor is drained, so C_{IN} hold all the energy in the LC tank ΔE_{LC}'. Since the transfer is assumed to be sinusoidal, the energy in the LC tank stays the same before and after the transfer:

$$\Delta E_{LC(ID)} = 0.5 C_{PZ} {v_B}^2 = \Delta E_{C(ID)}{}' + E_{L(ID)}$$

$$= \Delta E_{C(ID)} + E_{C(PK)} - E_{C(M.DI)}$$

$$= 0.5 C_{PZ} \left[\left(v_B - v_{C(M.ID)} \right)^2 + {v_{C(PK)}}^2 - {v_{C(M.ID}}^2 \right] \tag{49}$$

$$= 0.5 C_{PZ} \left[{v_B}^2 - 2 v_B v_{C(M.ID)}{}' + {v_{C(PK)}}^2 \right],$$

where $\Delta E_{C(ID)}$ is the initial energy on C_{IN} when referred to v_{DC}. From (49), the $v_{C(M.ID)}$ to stop energizing can be solved for:

$$v_{C(M.ID)}{}' = \frac{{v_{C(PK)}}^2}{2 v_B}. \tag{50}$$

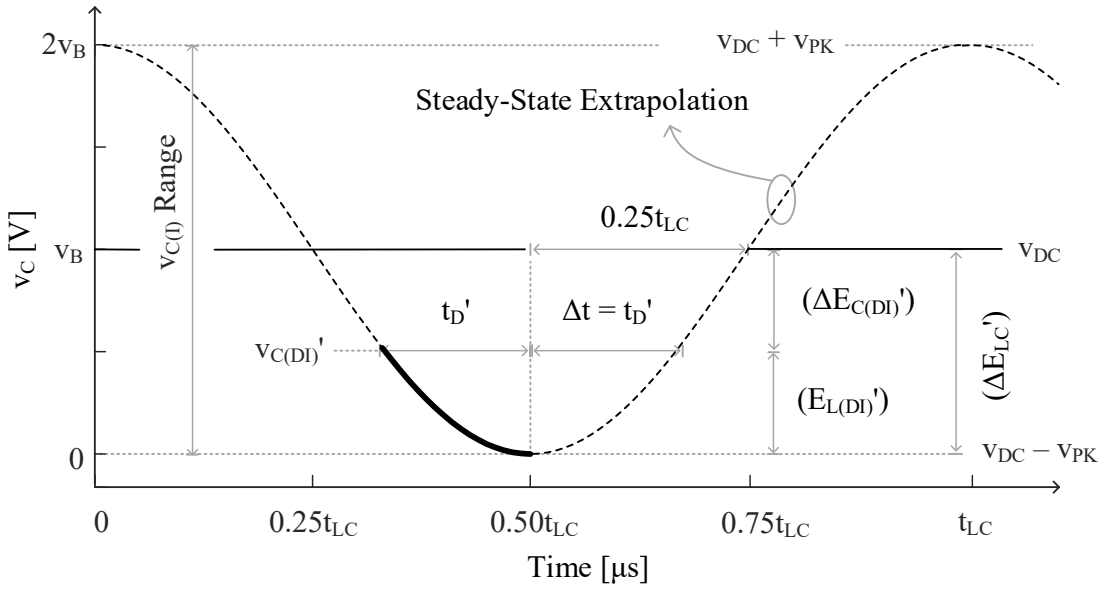

Figure 4-8. Steady-state extrapolation of direct phase voltage transition.

With $v_{C(M.ID)}$', the $t_{E(ID)}$ and $t_{D(ID)}$ to complete the transfer can be solved for with (45), (46), and (47). As a result, the ohmic loss during an indirect–direct transfer can be calculated:

$$E_{R(ID)} = R_{ESR} i_{L(RMS.ID)}{}^2 t_{X(ID)} = R_{ESR} i_{L(RMS.ID)}{}^2 \left(t_{E(ID)} + t_{D(ID)}\right), \tag{51}$$

where $i_{L(RMS.ID)}$ is the RMS current across the indirect–direct transfer, and $t_{X(ID)}$ is the total transfer time. Note that during energize, C_{IN} drains from $v_{C(PK)}$ to $v_{C(M.ID)}$, so $v_{C(M.ID)}$ has to be lower than $v_{C(PK)}$. The indirect–direct transfer can only be possible when:

$$v_{C(PK)} \geq v_{C(M.ID)} = \frac{v_{C(PK)}{}^2}{2v_B} \tag{52}$$

$$v_{C(PK)} \leq 2v_B \ . \tag{53}$$

Another way to analyze the condition for indirect–direct is to examine Fig. 4-8. $v_{C(M.ID)}$ has a range between ground and the peak of the steady-state extrapolation, $2v_B$,

$$v_{C(M.ID)} = \frac{v_{C(PK)}{}^2}{2v_B} \leq 2v_B \tag{54}$$

$$v_{C(PK)} \leq 2v_B \ . \tag{55}$$

The indirect–direct can transfer part of the energy to the battery without L_X holding it. Therefore, L_X never receives the entire energy E_C, and the peak inductor current is always lower. As a result, the ohmic loss would be lower.

4.2.3. Pre-Charge

As detailed in Chapter 3, pre-charging can significantly increase drawn and output power, and is necessary for tiny piezoelectric chargers. To achieve pre-charging, we need to use the battery to charge C_{PZ} to the desired voltage before a half cycle starts. Unlike the indirect case shown in Section 4.3.3, the pre-charging transfer can also be achieved with a direct portion. This can be done by directly energizing both L_X and C_{PZ} with the circuit in Fig. 4-9(a) first, and then use the circuit in Fig. 4-9(b) to drain L_X further into C_{PZ} to complete pre-charging. The inductor current waveform is shown in Fig. 4-10, where from 0.6 µs to 3.2 µs depicts the indirect–direct transfer to drain C_{PZ}, and from 3.2 µs to 5.8 µs shows the direct–indirect pre-charge. Both the drain C_{PZ} transfer and the pre-charge transfer have lower inductor current and transfer time compared with their indirect counterparts, saving ohmic power.

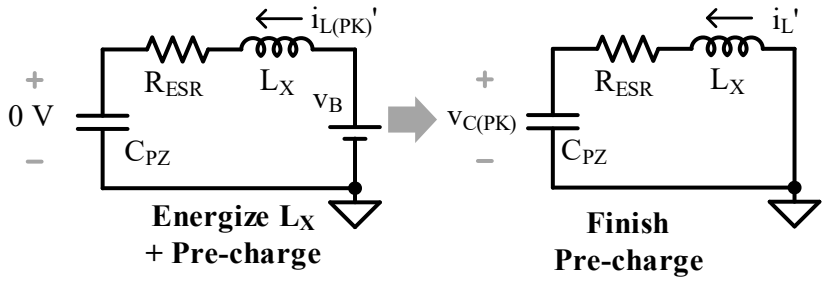

Figure 4-9. Switching configuration for direct-indirect pre-charge.

4.3. **Direct–Indirect Transfer**

4.3.1. Operation

Since the indirect–direct transfer only works under certain conditions, we need to find another direct energy transfer configuration when indirect–direct is impossible. The way

to accomplish that is the direct–indirect transfer, where C_{IN} drains to L_X and directly to v_B to start the transfer, as shown in Fig. 4-11(a). Note that v_B has to be lower than $v_{C(PK)}$ for this transfer to start. As v_C drains from $v_{C(PK)}$ to v_B, L_X energizes. The first phase of the draining the inductor has the same switching configuration as the energizing phase, so that both C_{IN} and L_X can both drain directly into v_B, until C_{PZ} has no charge. At that point, L_X holds draining current $i_{L(M.DI)}$, and then is connect to the battery in the second drain phase to complete the transfer.

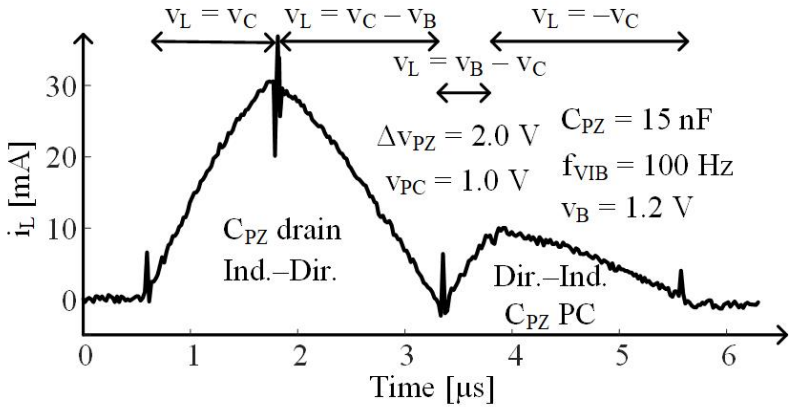

Figure 4-10. Inductor current for indirect–direct C_{PZ} drain and direct–indirectpre-charging with battery investment.

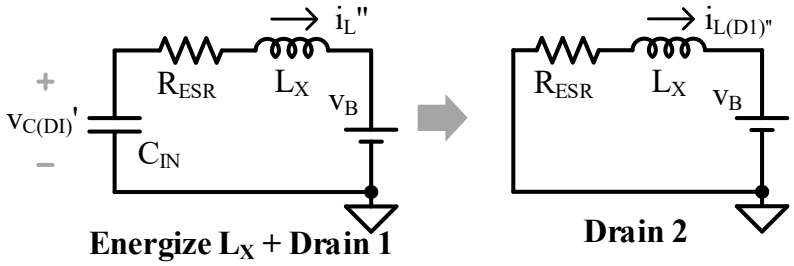

Figure 4-11. Switching configuration for energize, drain 1, and drain 2 phase in a direct–indirect transfer.

4.3.2. Ohmic Losses

The inductor current i_L" for Direct–Indirect is shown in the solid trace in Fig. 4-12. As a reference, the indirect current i_L is also plotted with the dashed trace. The energizing phase is still a quarter cycle of the LC oscillation,

$$t_{E(DI)} = 0.25t_{LC} = 0.5\pi\sqrt{L_X C_{PZ}}\,. \tag{56}$$

However, since the energizing voltage for L_X is $v_C - v_B$ instead of v_B, the peak current $i_{L(PK)}$ is redueced from 34 mA in indirect to 20 mA. After LX finishes energizing, piezoelectric voltage is at v_B instead of at 0, and needs to continue to drain. This drain 1 phase is achieved by continuing the L_X oscillation with piezoelectric voltage v_C centered around battery voltage v_B, during which both C_{PZ} and L_X drain into v_B. Together with the energizing phase make up the direct part of the transfer, as shown from 1.2 µs to 4.0 µs in Fig. 4-12.

Figure 4-13 shows the waveform for v_C and its steady-state extrapolation during the direct phase of the transfer. The steady state extrapolation is sinusoidal centered at the dc voltage. Since L_X is a dc short, the dc voltage is v_B. Because the transfer starts at $v_{C(PK)}$, the peak voltage of the sinusoidal is $v_{C(PK)} - v_B$. The energize phase takes up a quarter cycle of the sinusoidal, and the drain 1 phase is a part of quarter cycle. Across the drain 1 phase, v_C goes from v_B to 0, which takes

$$v_B = \left(v_{C(PK)} - v_B\right)\sin\left(\frac{2\pi t_{D1(DI)}}{t_{LC}}\right). \tag{57}$$

$$t_{D1(DI)} = \frac{t_{LC}}{2\pi}\sin^{-1}\left(\frac{v_B}{v_{C(PK)} - v_B}\right). \tag{58}$$

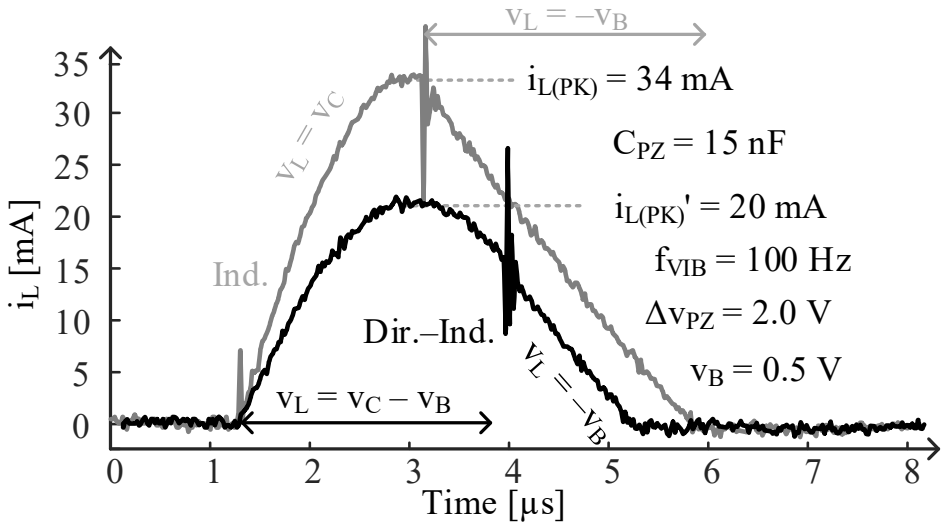

Figure 4-12. Inductor current for indirect and indirect–direct transfers.

Because the voltage is centered at v_B, the energy in the LC tank would also need to refer to its dc voltage. The total energy transferred in the direct phase is

$$\begin{aligned} \Delta E_{LC(DI)} &= 0.5 C_{PZ}\left(v_{C(PK)} - v_B\right)^2 \\ &= \Delta E_{C(DI)} + E_{L(DI)} = 0.5 C_{PZ} v_B{}^2 + 0.5 L_X i_{L1(DI)}{}^2 \end{aligned} \tag{59}$$

From (59), we can get

$$i_{L1(DI)} = \sqrt{\frac{L_X}{C_{PZ}} v_{C(PK)}\left(v_{C(PK)} - 2v_B\right)} \tag{60}$$

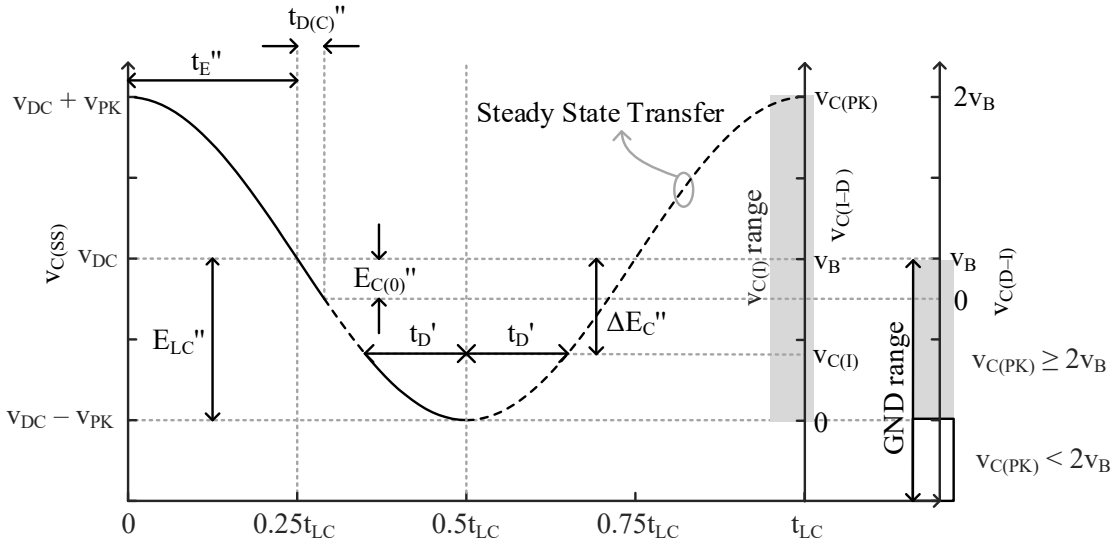

Figure 4-13. Steady-state extrapolation of direct phase voltage transition.

The indirect phase of the transfer is between the inductor and the battery, and the inductor current falls linearly. Therefore, the time it takes to drain the inductor is

$$t_{D2(DI)} = \frac{L_X}{v_B} i_{L1(DI)}. \tag{61}$$

With the transfer time and current profile completed, we can calculate the ohmic loss during a direct–indirect transfer. Note from Fig. 4-13, in order to be able to completely drain C_{IN} after drain 1 phase, ground has to be above the negative peak of the oscillation. Therefore, direct–indirect transfer has to satisfy:

$$v_{DC} - v_{PK} = v_B - \left(v_{C(PK)} - v_B\right) = 2v_B - v_{C(PK)} \leq 0. \tag{62}$$

The same condition can be obtained from (18), since $v_{C(PK)} - 2v_B$ is inside of a square root and therefore has to be non-negative. Interestingly, the condition for direct–indirect transfer complements that for indirect–direct, meaning no matter the relationship between $v_{C(PK)}$

and v_B, we can always choose either direct–indirect or indirect–direct. The only exception is when $v_{C(PK)} = 2v_B$, and that's when both can work. In fact, that's the condition when the entire transfer is direct.

Similar to indirect–direct, direct–indirect can deliver part of the energy to the battery without L_X holding it. Therefore, L_X never receives the entire energy E_C, and the peak inductor current is always lower. The ohmic loss is

$$\begin{aligned} E_{R(DI)} &= R_{ESR} i_{L(RMS.DI)}{}^2 t_{X(DI)} \\ &= R_{ESR} i_{L(RMS.DI)}{}^2 \left(t_{E(DI)} + t_{D1(DI)} + t_{D2(DI)}\right), \end{aligned} \tag{63}$$

where $i_{L(RMS.DI)}$ is the RMS current across the direct–indirect transfer, and $t_{X(DI)}$ is the total transfer time.

4.3.3. Pre-Charge

Pre-charges using direct–indirect transfer can be done using the same direct–indirect pre-charge after charging v_B, shown in Fig. 4-10. However, there is a more efficient way by not completely draining the inductor when it charges the battery. Instead, some energy is preserved to charge C_{PZ} in the opposite direction. The switching configuration is shown in Fig. 4-14, while the inductor current is shown in Fig. 4-15. From 0.6 µs to 3.0 µs C_{PZ} directly charge battery and energize L_X, and LX partially drains into both C_{PZ} and v_B using the direct configuration in the Fig. 4-14(a). From 3.0 µs to 3.8 µs L_X charges v_B using Fig. 4-14(b), and from 3.8 µs to 5.8 µs L_X charges C_{PZ} in the negative direction using the circuit in Fig. 4-14(c).

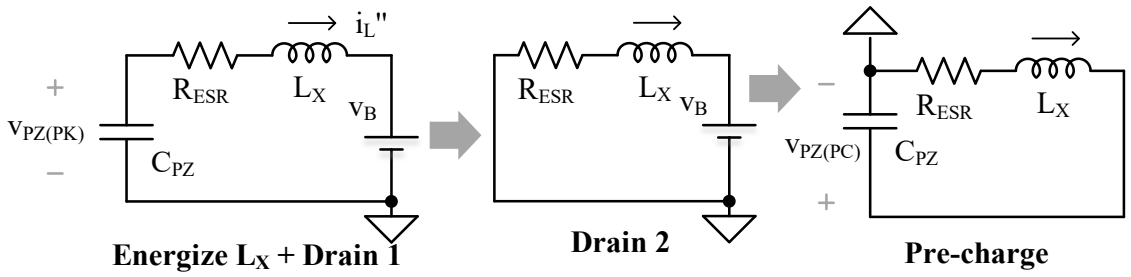

Figure 4-14. Switching configuration to pre-charge after a direct-indirect transfer.

4.4. **Comparisons**

The previous three sections detail the operation of indirect, indirect–direct, and direct–indirect transfers, and this section compares the ohmic loss. Since indirect–direct transfer and direct–indirect transfer both deliver part of the energy directly from C_{IN} to the battery, and the conditions for one complements the other, we combine the two transfers and denote them direct transfers.

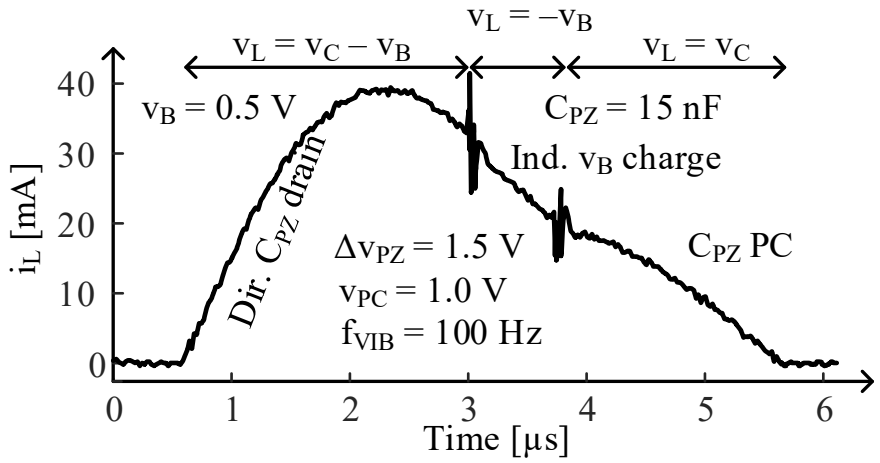

Figure 4-15. Inductor current for direct–indirect C_{PZ} drain and pre-charging without battery investment.

4.4.1. Ohmic Loss

Fig. 4-16 compares the total transfer time and peak current for Indirect-Only transfer and direct transfers when $v_{C(PK)}$ is 1 V and v_B between 0.1 V and 5 V. The Direct–Indirect transfer region, $v_B \leq 0.5$ V is highlighted by the grey shade, while the Indirect–Direct transfer region has the white background. The y-axis indicates the percentage of t_X and $i_{L(PK)}$ the direct transfers have. The dotted black trace at 100% represents t_X and $i_{L(PK)}$ as reference. As shown by the solid trace, t_X' and t_X" are between 80% and 95 % of t_X, so the direct transfers always take shorter time than the corresponding indirect transfer. Similarly, the peak current for direct transfers, indicated by the dashed trace, is between 50% and 99% of that for indirect transfer. Although peak current is not always proportional to RMS current, it's still a strong correlation with ohmic loss. From Fig. 4-7 and Fig. 4-12, the current for direct is always lower than the current for indirect, even without assuming sinusoidal transfer, resulting in lower ohmic loss.

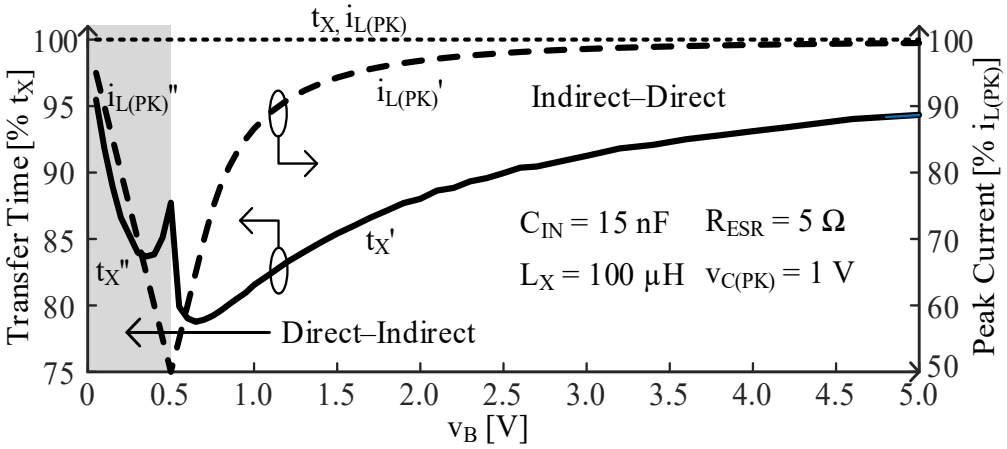

Figure 4-16. Transfer time and peak current comparisons between indirect and direct transfers.

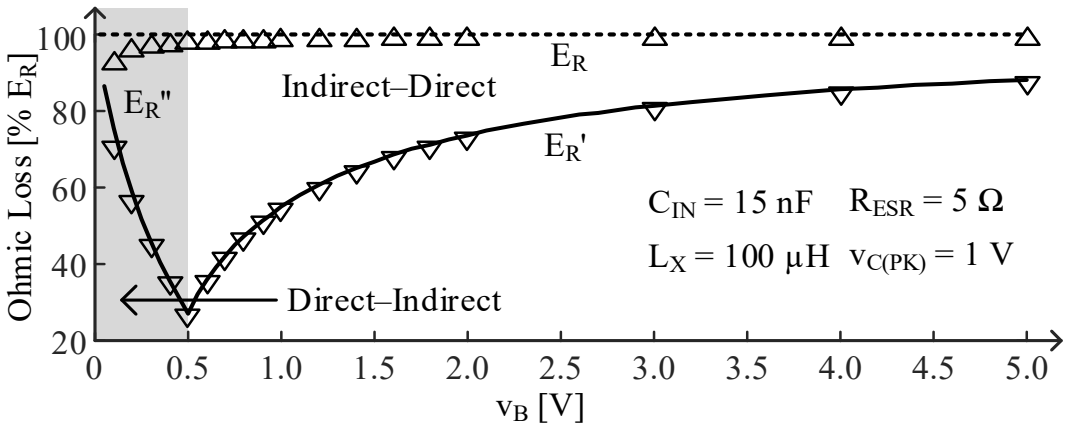

Figure 4-17. Simulated Ohmic loss for indirect and direct transfers.

Fig. 4-17 validates the comparison between the total ohmic loss for indirect transfer and direct transfers when $v_{C(PK)}$ is 1 V and v_B between 0.1 V and 5 V. Again the direct–indirect transfer region, $v_B \leq 0.5$ V, is highlighted by the grey shade, while the indirect–direct transfer region has the white background. The y-axis is the percentage of E_R that the direct transfers consume. Utilizing direct transfer drops the ohmic loss to 26% to 86% of that for indirect, indicated by the solid black trace. The markers represent the simulated ohmic loss across a transfer on a 5 Ω ESR and the error is below 8%. The reduction is the greatest when $v_B = 0.5$ V, which is the condition for the entire transfer to be direct. This makes sense because although the transfer time is not the shortest, the peak current is only half of that for indirect, and therefore L_X only needs to hold a quarter of the energy transferred. The triangle markers represent the simulated loss across a transfer on a 5 Ω ESR and the error is below 8%. It's noticeable from Fig. 4-17 that the more direct a transfer has, the lower the loss is. Therefore, utilizing as much direct as possible is key to have the least ohmic loss piezoelectric charger. As a result, the switched-inductor bridge is the least

lossy charger. Along with the fact that it uses symmetric pre-charging to significantly increase drawn power, it's the best piezoelectric charger with synchronized discharge.

Table 4-1. Switching configurations for each transfer mode

Transfer Mode		Half Cycle	Transfer		Switches Engaged
			From	To	
Indirect		+ to –	C_{PZ}	L_X	$S_{GI–}$, S_{I+}, $S_{I–}$
			PC L_X	C_{PZ}	S_{GI+}, S_{I+}, $S_{I–}$
			L_X	v_B	S_{G+}, $S_{O–}$
		– to +	C_{PZ}	L_X	S_{GI+}, S_{I+}, $S_{I–}$
			PC L_X	C_{PZ}	$S_{GP–}$, S_{I+}, $S_{I–}$
			L_X	v_B	$S_{G–}$, S_{B+}
Dir.	Ind. to Dir.	+ to –	C_{PZ}	L_X	$S_{GI–}$, S_{I+}, $S_{I–}$
			C_{PZ}	$L_X + v_B$	$S_{GI–}$, S_{I+}, $S_{O–}$
			PC v_B	$L_X + C_{PZ}$	S_{GI+}, $S_{P–}$, S_{B+}
			PC L_X	C_{PZ}	S_{GI+}, $S_{I–}$, S_{I+}
		– to +	C_{PZ}	L_X	S_{GI+}, S_{I+}, $S_{I–}$
			C_{PZ}	$L_X + v_B$	S_{GI+}, $S_{I–}$, S_{O+}
			PC v_B	$L_X + C_{PZ}$	$S_{GI–}$, S_{I+}, S_{B+}
			PC L_X	C_{PZ}	$S_{GI–}$, S_{I+}, $S_{I–}$
	Dir. to Ind.	+ to –	C_{PZ}	$L_X + v_B$	$S_{GI–}$, S_{I+}, $S_{O–}$
			$C_{PZ} + L_X$	v_B	
			L_X	v_B	S_{G+}, $S_{O–}$
			PC L_X	C_{PZ}	S_{GI+}, S_{I+}, $S_{I–}$
		– to +	C_{PZ}	$L_X + v_B$	$S_{GI–}$, $S_{I–}$, S_{O+}
			$C_{PZ} + L_X$	v_B	
			L_X	v_B	$S_{G–}$, S_{O+}
			PC L_X	C_{PZ}	S_{GI+}, S_{I+}, $S_{I–}$

The synchronous discharge without pre-charge, with symmetrical pre-charge, and with asymmetrical pre-charge using indirect and 2 types of direct transfers are all implemented and measured using the circuit in Fig. 3-12. Table 4-1 lists the switch configuration for all the transfers. For each mode, across the positive half cycle, S_{GPN} is closed so that the bottom plate of C_{PZ} is ground, and all other switches open so that i_{PZ} can charge C_{PZ} by $\Delta v_{PZ(OC)}$. Similarly, across the negative half cycle, S_{GPP} is closed so that the top plate of C_{PZ} is ground, and all other switches open so that i_{PZ} can charge C_{PZ} by $\Delta v_{PZ(OC)}$. The PC under the Transfer column denotes pre-charging. It is only used in the pre-charge cases and ignored in the no pre-charge ones.

4.4.2. Prototype

The power stage in Fig 3-12 has been fabricated using 0.18μm CMOS technology, shown in Fig. 4-18. The photo of the die is shown in Fig. 4-19. A 15 nF piezoelectric transducer from Mide Technology is used as the source, and a shaker from Brüel & Kjær, which is controlled by a signal generator, is utilized to vibrate the transducer to produce 0 – 14 μA sinusoid current, which translates to 0 – 3.0 V open circuit voltage. A 100 μH, 0.6 Ω surface mount inductor is used to transfer the energy, and a field programmable gate array controls the switching sequence and tracks the maximum power-point (MPP). MPP is achieved by increasing the pre-charging voltage, which is controlled by the pre-charging time in the respective transfer scheme, until the output power peaks. The MPP controller also monitors the switching node to sense the zero current point to turn off the inductor current path. The

testing setup, including the piezoelectric transducer and the PCB with fabricated IC, inductor, and connection to FPGA, is shown in Fig. 4-20.

4.4.2.A. Bulk Connection

When an NMOS (PMOS) the off state has its bulk voltage a diode voltage below (above) its source voltage, the body diode turn on, and the MOSFET starts conducting unwanted current. As detailed in Section II, there are no negative voltage in the system. Therefore all the NMOS can have their bulk connect to ground, and the body diodes will not turn on.

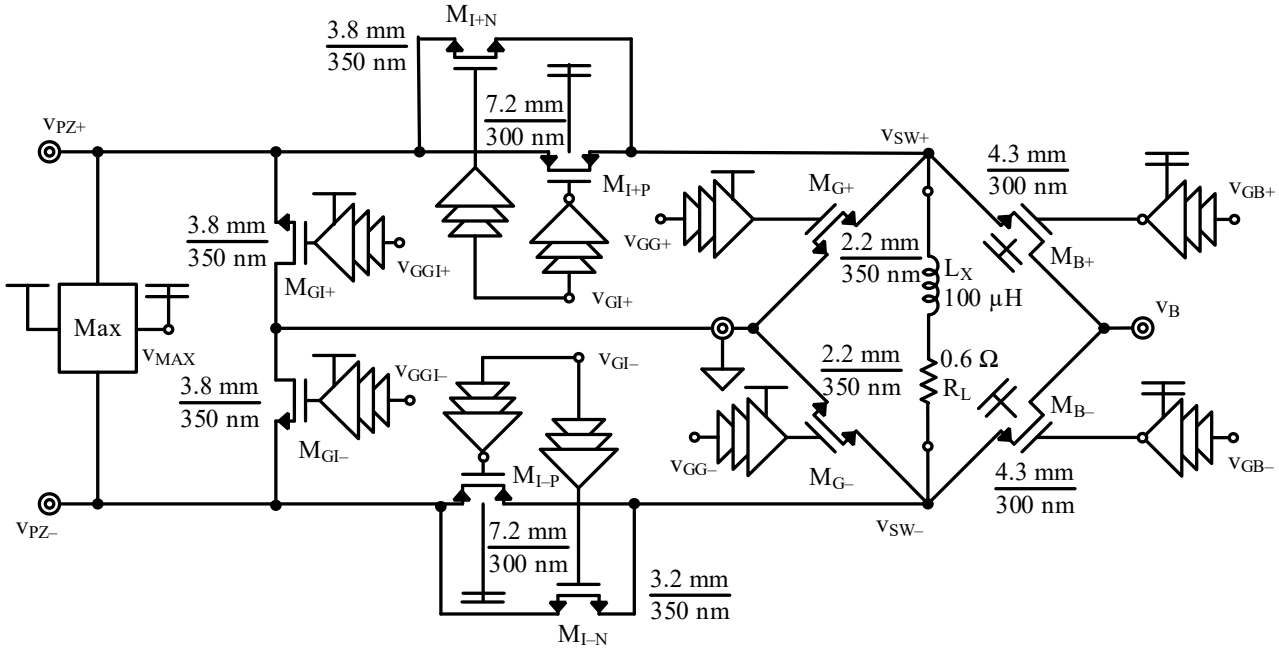

Figure 4-18. Power stage implemented in 180-nm CMOS technology with 3.3-V devices.

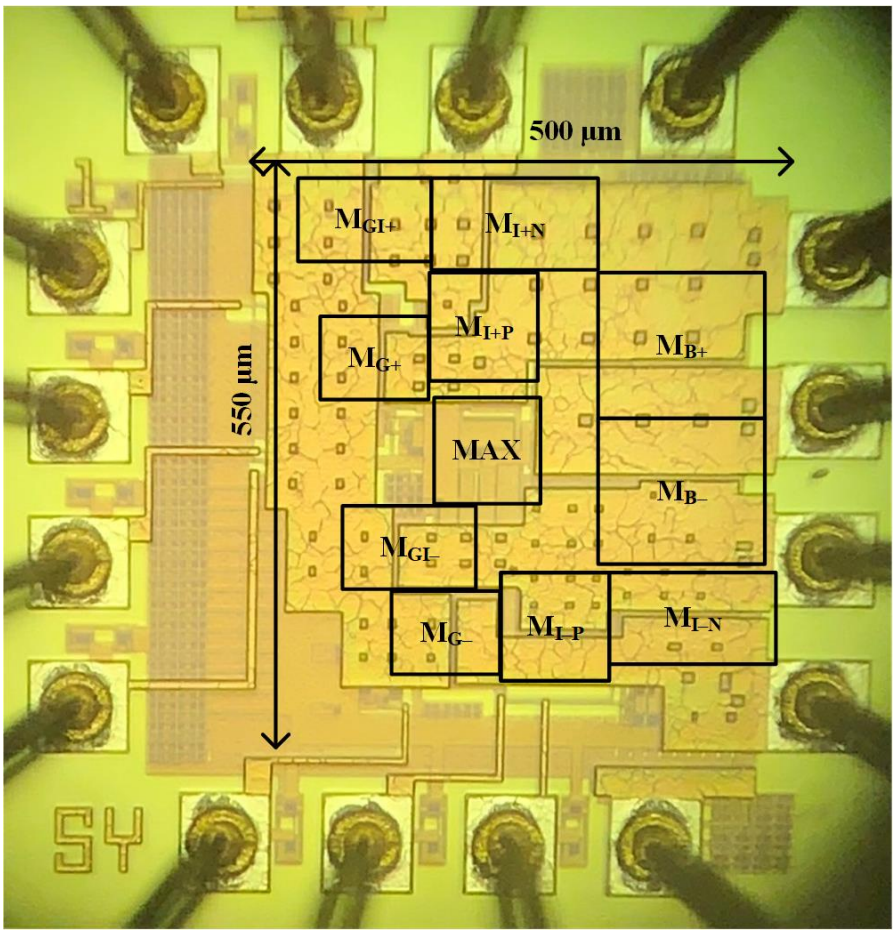

Figure 4-20. Photo of the die of the power stage.

The PMOS switches, on the other hand, are different because the piezoelectric voltage varies between 0 and V_{BD}, while the battery voltage can also be between 0 and V_{BD}. Since the switching nodes (v_{PZ+}, v_{PZ-}, v_{SW+}, and v_{SW-}) can be either higher or lower than v_B, but we still don't want the PMOS to conduct current when i_{PZ} is charging C_{PZ}, the bulk of the PMOS switches have to connect to the highest voltage in the system in order to stop body diodes from turning on. Therefore, a max block is needed to select the highest of the three voltages among v_{PZ+}, v_{PZ-}, and v_B too feed the bulk and the gate drivers of the PMOS.

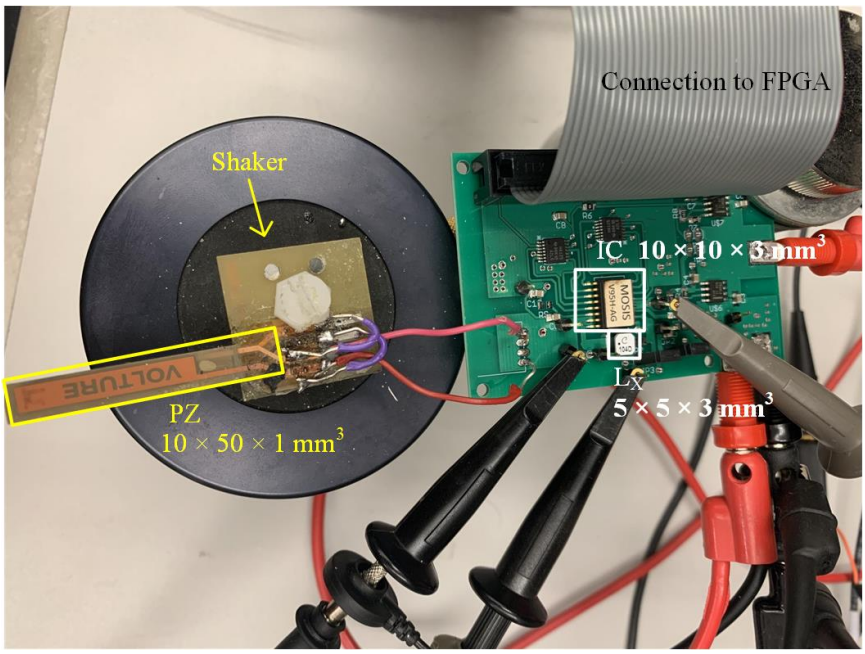

Figure 4-21. Photo of the testing setup including piezoelectric transducer, power stage IC, inductor L_X, and connection to FPGA.

4.4.2.B. Max Block

As discussed in the previous sub-section, the max block outputs the highest voltage among its three inputs. Two cross-coupled PMOS pairs can accomplish this function. Each cross-coupled PMOS pair connects the middle node to the input if it's at least a threshold higher than the other input. As Fig. 4-21 shows, v_{O1} is connected to the higher of v_{PZ+} and v_{PZ-}, and v_{MAX} is the higher voltage of v_{O1} and v_B. Since v_{MAX} is the highest voltage of all, the bulks of the PMOS are connected to it.

If the two inputs are within a threshold of each other, the middle node could drop to up to a threshold below the higher input. Decoupling capacitors are added to the output to maintain the voltage when the inputs are close, and as long as the voltage drop does not turn on the PMOS switches completely, the functionality is maintained. Since the v_{MAX} is

the supply of the PMOS gate drivers, it needs to be able to provide current without too much voltage drop. The PMOS pairs are therefore sized such that they can provide the maximum instant current v_{MAX} supplies without v_{MAX} dropping by 200 mV.

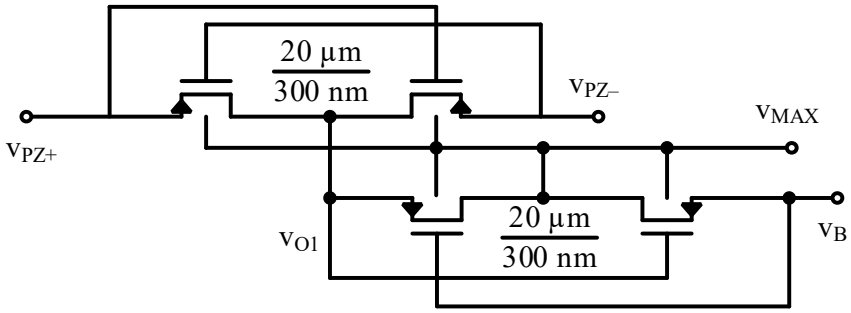

Figure 4-22. Schematics of the Max block.

4.4.2.C. Drivers

Because the MOSFET switches have large widths to balance ohmic loss and switching loss, they require gate drivers to turn them on and off quickly and efficiently. An inverter chain with each stage 2.72× larger than the previous stage can produce the shortest delay. However, increasing the number of the stages can result in larger switching and shoot-through losses. Because the extra pico-seconds delay does not affect the operation of the charger, an inverter chain in which each stage is 5× to 10× larger than the previous stage is used as drivers.

The NMOS switches can be turned on with v_B and turned off with ground. Therefore, v_B and ground are the supplies for the NMOS gate drivers, as shown in Fig. 4-22. The PMOS switches, on the other hand, must be turned on with ground and turned off with v_{MAX}. Therefore, a level shifter is needed between the the signal from the controller

and the gate. As Fig. 4-23 shows, the level shifter with cross-coupled PMOS is used as the last stage of the inverter chain, to minimize the loss on the gate driver.

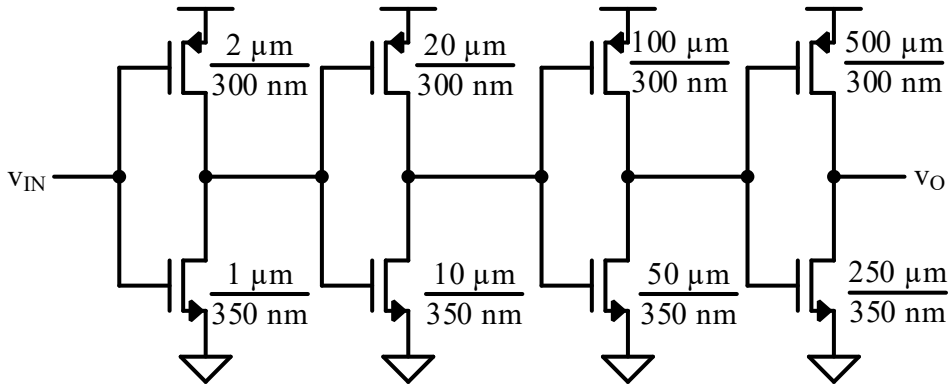

Figure 4-23. Schematic of the NMOS gate drivers.

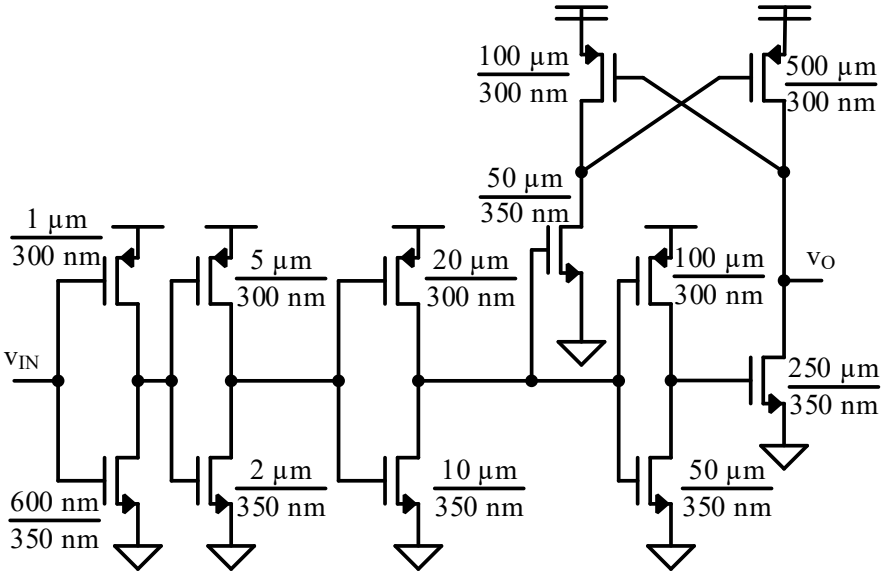

Figure 4-24. Schematic of the PMOS gate drivers.

4.4.3. Output Power

The output power using no pre-charging, symmetric pre-charging indirect, asymmetric pre-charging direct, and symmetric pre-charging indirect are shown in Fig. 4-24 with vibration

frequency of 100 Hz, open circuit voltage $\Delta v_{PZ(OC)}$ at 1.5 V, and battery voltage v_B ranging from 0.1 V to 3.0 V. All the data points are collected at its MPP, and the pre-charging voltage varies for each data point. The data points to the left of v_B' uses direct–indirect, and to the right of v_B' uses indirect–direct.

The figure shows that pre-charging can output more power than no pre-charging. It also shows that for symmetrical pre-charging, using direct can output almost 50% more power because of the lower ohmic losses. The reduced loss in the transfer can also allow the symmetrical pre-charging direct to have higher pre-charging voltage, resulting in additional drawn power. The figure also shows that the symmetrical pre-charging direct has higher output power than asymmetrical pre-charging direct, because the symmetrical case charges the battery using two smaller energy packet each cycle, resulting in lower ohmic loss.

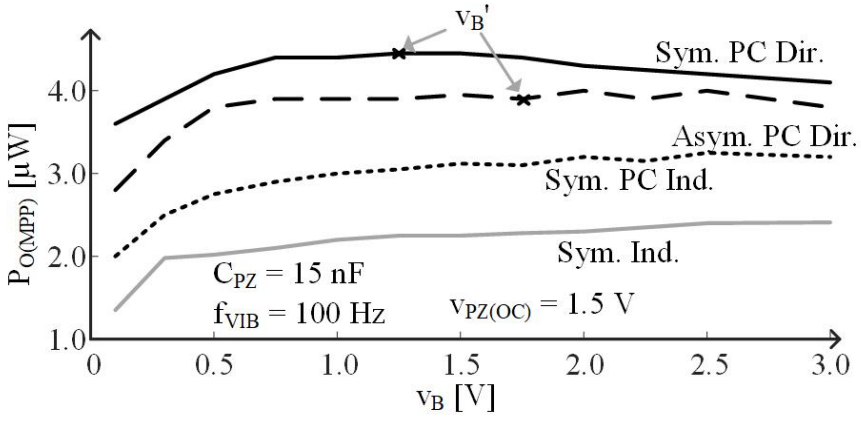

Figure 4-25. Output power for symmetry and direct vs indirect across v_B.

The chargers also consumes charge loss, quiescent loss, and leakage loss. However, these losses are the same for all the transfer schemes, and the only difference is ohmic loss. Moreover, because the inductor has to be small, and because the vibration frequency is

low, ohmic loss on the inductor is the dominant loss. Fig. 4-24 also shows that the output power is not very sensitive to battery voltage, meaning the charger can output close to the same power regardless of the condition of the battery. That's because the peak inductor current in each transfer using synchronous discharge is not affected by v_B. It also shows that for the symmetrical pre-charging direct case, the highest output power, another way of saying lowest ohmic loss, is at the v_B', where the entire transfer is direct, confirming the theory proposed in [151].

Fig. 4-25 shows the maximum output power across the vibration range. The symmetrical/asymmetrical pre-charging direct/indirect transfers are plotted, and each data point is at its MPP. For the direct cases, $v_{PZ(OC)}'$ are marked as the point where the entire transfer is direct, and the data points to the left are with indirect–direct, and to the right vice versa. The figure confirm that symmetrical pre-charge with direct is the best across all the operating conditions.

Fig. 4-25 also shows the operating range for the chargers. From the lower side, symmetrical PC direct, thanks to its lower ohmic loss, can start output net power with 0.2 V of $\Delta v_{PZ(OC)}$, which is the lowest among all the reported works This is significant because although vibrations are omnipresent, they are intermittent, and can be low amplitude across a long time. Therefore, being able to output net power from as low a vibration as possible is important to prolonging life and expanding functionality for wireless microsensors.

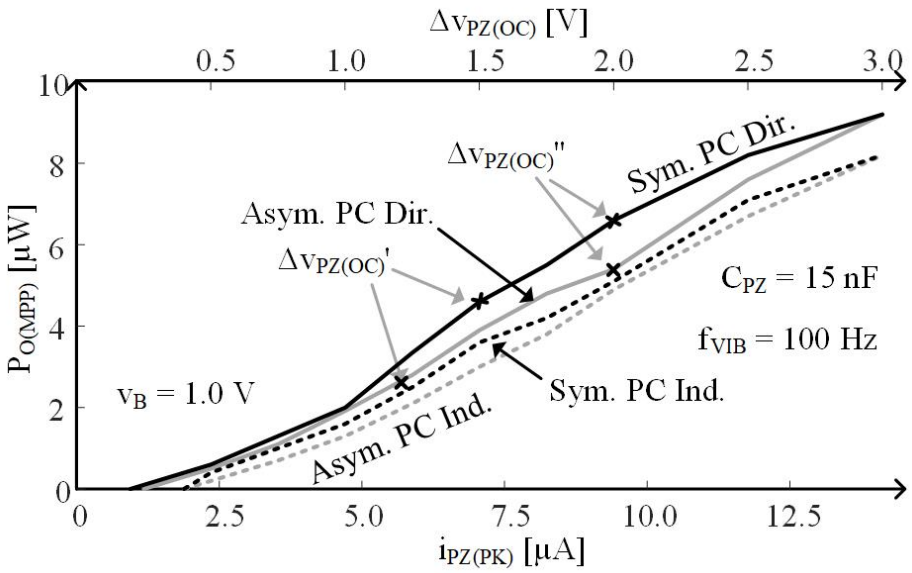

Figure 4-26. Output power for symmetry and direct vs indirect across vibration.

On the other end, because of the breakdown limit, the systems transitions from loss limited region into breakdown limited region at the $\Delta v_{PZ(OC)}$" marks on Fig. 12. For symmetrical PC, we need to lower pre-charge voltage, thereby sacrificing output power, to keep the system under safe conditions. For the asymmetrical case, $\Delta v_{PZ(OC)}$" is the highest open circuit voltage it can handle, unless the system can enter partial asymmetrical operation, and the trace to the right of $v_{PZ(OC)}$" shows the maximum output power. On the other end, because of the breakdown limit, the systems transfers from loss limited region into breakdown limited region from the data points $\Delta v_{PZ(OC)}$" marked on Fig. 4-25. For the symmetrical case, we would need to lower pre-charging voltage, therefore sacrificing drawn power and output power, to keep the system under safe conditions. On the other hand, for the asymmetrical case, this would be the highest vibration they can handle. However, with partial asymmetric pre-charging introduced in Section II.C, the system can

enter partial asymmetrical operation, and the trace to the right of $v_{PZ(OC)}$" shows the maximum output power.

Overall the charger, with a 3.0 V breakdown voltage, draws from 0.2 V – 3.0 V $\Delta v_{PZ(OC)}$, outputs 0.01 – 7.9 μW with indirect transfers, and outputs 0.01 – 9.1 μW with direct transfers. Even though the system is not optimized for any mode of operation, the symmetrical pre-charging direct is the best. Although other factors may impact the power performance (quality of design, different transducer, limits, etc), the theories presented in Chapters 3 and 4, and the validations here prove that symmetrical pre-charge with direct can draw the highest power with lowest losses.

4.5. **Summary**

Direct transfers can allow the inductor to transfer more power than it carries. As a result, the transfer time, and more importantly, peak inductor current, are lower than the indirect counterpart, reducing ohmic loss. Direct–indirect transfers should be utilized when the peak piezoelectric voltage is higher than $2v_B$, and indirect–direct transfers can be used otherwise. The ohmic loss saving is the most when the peak piezoelectric voltage is exactly twice the battery voltage, because the entire transfer can be direct, reducing the peak inductor current by half, and cutting the ohmic loss by 74%. Both indirect–direct and direct–indirect C_{PZ} drain can be followed by a direct–indirect pre-charge with battery investment. The investment can be avoided by not charging the battery with the entire inductor current. Instead, a portion of the energy is preserved, and used to pre-charge the piezoelectric transducer for the next half cycle.

The same charger used to compare the damping symmetry has been used to validate the performance for indirect/direct, with symmetrical, asymmetrical, and no pre-charging. Output power measurement shows that direct loses less power than indirect, and that the maximum output power is not sensitive to battery voltage, removing the need of an additional maximum power-point charger stage, like the recycling bridge state of the art does. Because of the saved ohmic loss, and the additional drawn power with the same breakdown limit, the symmetrical pre-charge with direct transfer is the best charger with synchronous discharges.

CHAPTER 5. HIGHEST OUTPUT POWER CHARGER

The previous chapter focuses on how to manage the piezoelectric transducer and its voltage to draw and output the most power. This chapter, on the other hand, shifts the focus on the switched-inductor. Specifically, how the inductor transfers the energy, and how to save the most power. The traditional way of transferring the energy by first energizing the inductor fully, then drain it completely is the simplest approach, but is it the best? Could there be some flaws in that scheme? Might some more carefully thought out approach save some power losses? This chapter dives deep into these issues.

5.1. **Design**

5.1.1. Optimize MOSFET Switch

The power switches employed in the power stage consume ohmic loss when they conduct current. They also require charge provided from the supply to switch them on and off [145]. For a MOSFET switch, we use the minimum length device to reduce the silicon area. The on resistance R_{MOS} decreases with the width of the device W_{MOS}, and the gate capacitance C_G increases with it. Therefore, the wider the switches, the higher the charge loss, but the lower the ohmic loss. Optimizing the power switches comes down to finding the lowest sum of these two losses.

Each power switch consumes ohmic power $P_{R(MOS)}$

$$P_{R(MOS)} = i_{MOS(RMS)}{}^2 R_{MOS} \left(\frac{t_C}{t_{VIB}}\right) \propto \frac{1}{W_{MOS}}, \tag{64}$$

where $i_{MOS(RMS)}$ is the root-mean-square (RMS) current through the device, t_C is the conduction time, and $K_{R(MOS)}$ is the coefficient. Each switch also requires charge to switch it on and off, and consumes charge loss $P_{C(MOS)}$

$$P_{C(MOS)} = {v_{DD}}^2 q_C f_{SW} = v_R(C_G v_R) f_{SW} = C_G {V_{BD}}^2 f_{SW} = K_C W_{MOS} \propto W_{MOS}, \quad (65)$$

where q_C is the charge required to turn the switch on, f_{SW} is the switching frequency, v_{DD} is the supply voltage, and $K_{C(MOS)}$ is the coefficient. Since v_R is regulated to near V_{BD}, v_{DD} is also near V_{BD}. To find the lowest total loss, we increase W_{MOS} until the change in $P_{C(MOS)}$ cancels the change in $P_{R(MOS)}$:

$$\frac{dP_{MOS}}{dW_{MOS}} = \frac{dP_{R(MOS)}}{dW_{MOS}} + \frac{dP_{C(MOS)}}{dW_{MOS}} = -\frac{K_{R(MOS)}}{{W_{MOS}}^2} + K_{C(MOS)} = 0. \quad (66)$$

The optimum width W_{MOS}' is

$$W_{MOS}' = \sqrt{\frac{K_{R(MOS)}}{K_{C(MOS)}}}, \quad (67)$$

and the total loss is

$$P_{MOS}' = P_{R(MOS)}' + P_{C(MOS)}' = \frac{K_{R(MOS)}}{W_{MOS}'} + K_{C(MOS)} W_{MOS}'$$

$$= \frac{K_{R(MOS)}}{\sqrt{\frac{K_{R(MOS)}}{K_{C(MOS)}}}} + K_{C(MOS)} \sqrt{\frac{K_{R(MOS)}}{K_{C(MOS)}}} = 2\sqrt{K_{R(MOS)} K_{C(MOS)}}. \quad (68)$$

This occurs when $P_{C(MOS)}$ equals $P_{R(MOS)}$, and it is shown in Fig. 5-1. As a result, optimized power switches always consume equal ohmic and charge loss.

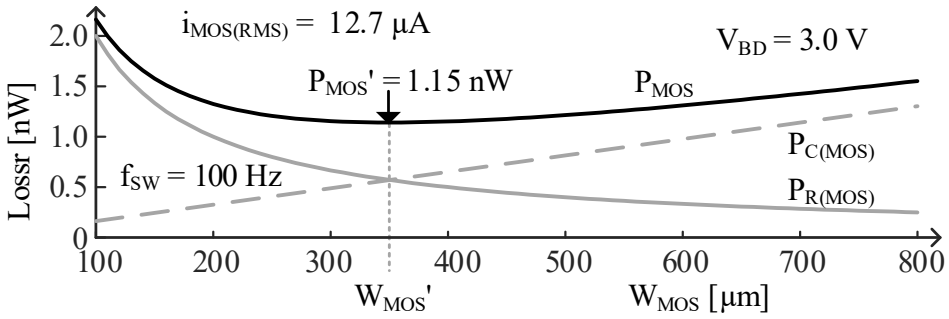

Figure 5-1. Ohmic loss, charge loss, and total loss on a MOSFET switch with minimum length and increasing width.

Bridge: The bridge consists of 4 power switches. Each switch on the bridge conducts half of t_{VIB}, and the current across that conduction time is $i_{PZ,}$ with an RMS of 12.7 µA. Therefore, we can use (64) and (65) to optimize the bridge, and each switch consumes 1.15 nW with and optimized width of 350 nm. Therefore, the loss of bridge P_{BRG} is 4.6 nW.

Recycler/Switched Inductor: The ohmic loss and charge loss on the power switches in the rest of the power stage, i.e. the two switched inductors (SL), is not only a function of the width of the device, but some other design parameters, e.g. inductance and switching frequency. However, the conclusion that the loss on the power switch is the least when charge loss equals the ohmic loss still applies. Therefore, we can use this conclusion to remove device width as a variable in the optimization, and optimize the other design parameters.

5.1.2. Optimize Recycler

After the bridge steers current into rectifying capacitor C_R across a half cycle, the recycler, consists of switch S_X and inductor L_X with equivalent series resistance R_{LX}. The inductor receives all the energy from C_{PZ} across a quarter of the LC oscillation cycle, as the current and voltage waveforms in Fig. 5-2 indicate, and back to the C_{PZ} in the opposite direction across the next quarter cycle. The transition takes a half cycle

$$t_X = 0.5t_{LC} = 0.5\sqrt{2\pi L_X C_{PZ}}. \tag{69}$$

The energy transferred E_X is

$$E_X = E_C = 0.5C_{PZ}{V_{BD}}^2 \approx E_{LX}{i_{LX(PK)}}^2. \tag{70}$$

The period of the LC oscillation is so short compared with a vibration period that the transition looks instantaneous. The ohmic loss on R_{LX} is

$$\begin{aligned} P_{R(LX)} &= {i_{LX(RMS)}}^2 R_{LX}\left(\frac{t_C}{t_{VIB}}\right) = \frac{1}{2}\left(\frac{C_{PZ}{V_{BD}}^2}{L_X}\right)(L_X k_L)\left(\frac{0.5\sqrt{2\pi L_X C_{PZ}}}{t_{VIB}}\right) \\ &= K_{R(LX)}\sqrt{L_X} \propto \sqrt{L_X}\,, \end{aligned} \tag{71}$$

where k_L is the ratio of R_{LX} to L_X, and $K_{R(LX)}$ is the coefficient. Since the inductor is limited to a $3 \times 3 \times 0.8$ mm^3 box, inductance increases with the number of turns, which leads to higher series resistance. To better demonstrate the optimization, DC resistance values are used for derivations. As shown in Fig. 5-3, where the solid line is a linear approximation of the values of inductance and resistance, the coefficient $k_L$is 55 Ω/mH. Since L_X is the

only variable in the final expression, we can simplify and see that loss of L_X is proportional to square root of L_X.

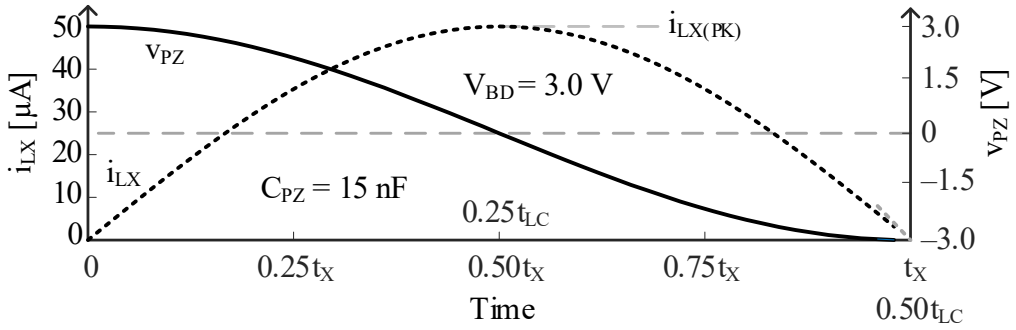

Figure 5-2. Current and voltage waveforms for the recycler.

Similarly, the ohmic loss on S_X is

$$P_{R(SX)} = {i_{LX(RMS)}}^2 R_{SX}\left(\frac{t_C}{t_{VIB}}\right) = \frac{1}{2}\left(\frac{C_{PZ}{V_{BD}}^2}{L_X}\right)R_{SX}\left(\frac{0.5\sqrt{2\pi L_X C_{PZ}}}{t_{VIB}}\right)$$
$$= \frac{K_{R(LX)}}{W_{SX}\sqrt{L_X}} \propto \frac{1}{W_{SX}\sqrt{L_X}}, \quad (72)$$

where $K_{R(SX)}$ is the constant coefficient. Interestingly, the ohmic loss on R_{LX} increases with higher L_X, but the ohmic loss on S_X decreases with higher L_X. That is because although higher L_X means lower peak inductor current, the transfer time increases with L_X, and R_{LX} also increases with L_X, but R_{SX} is completely decoupled with L_X.

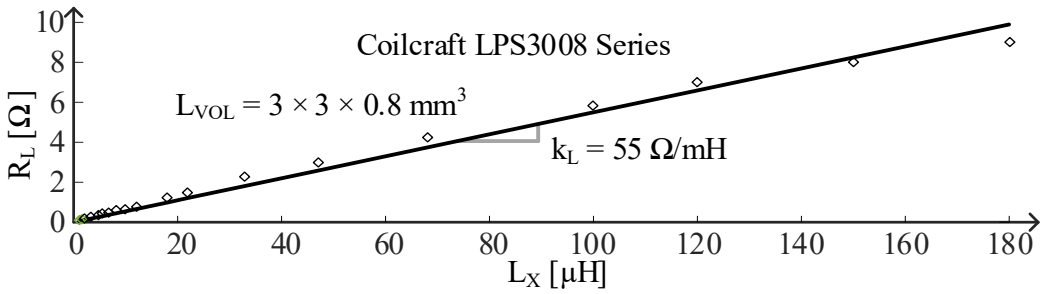

Figure 5-3. Inductance and resistance for a 3 × 3 × 0.8 mm^3 inductor.

From (64), the switch S_X also consumes charge loss that is proportional with W_{SX}, From Section 5.1.1, the total loss on S_X is at its minimum when $P_{R(SX)} = P_{C(SX)}$, and from (68) the total loss P_{SX} is the least when

$$P'_{SX} = 2\sqrt{K_{R(MOS)}K_{C(MOS)}} = 2\sqrt{\left(\frac{K_{R(SX)}}{\sqrt{L_X}}\right)K_{C(MOS)}} = \frac{K_{SX}}{L_X{}^{0.25}} \propto \frac{1}{L_X{}^{0.25}}, \qquad (73)$$

where K_{SX} is the coefficient. From (71) and (73), we can see that increasing L_X would result in higher loss on the inductor, but lower loss on the switch. Therefore, we increase L_X until the gain in $P_{R(LX)}$ cancels the reduction in P_{SX}

$$\frac{dP_X}{dL_X} = \frac{dP_{R(LX)}}{dL_X} + \frac{dP_{SX}}{dL_X} = \frac{0.5K_{R(LX)}}{\sqrt{L_X}} - \frac{K_{SX}}{4L_X{}^{0.25}} = 0. \qquad (74)$$

As shown in Fig. 5-4, the total loss on the recycler is 944 nW with an optimum L_X' = 7 μH, and W_{SX}' = 9.8 mm.

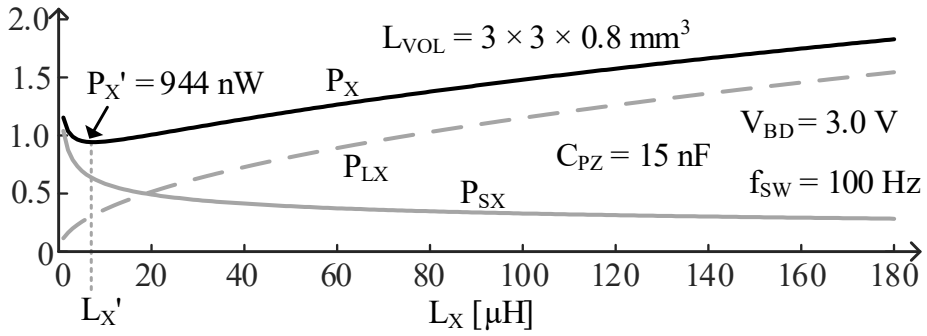

Figure 5-4. Power loss on inductor L_X, switch S_X, and total for the recycler.

5.1.3. Optimize MPP Switched Inductor

The last part of the power stage is the MPP switched-inductor (SL) charger that regulates the rectifying voltage at just under V_{BD} and charges the battery v_B. It is needed because P_{PZ} is proportional to the rectifying voltage, so it cannot directly connect to the battery, whose voltage varies from 0 to V_{BD}.

A buck-boost converter is used to lower loss. Switches S_R and S_{GO} close to establish energizing voltage v_E, which is v_R near V_{BD}, to energize the inductor L_O over energizing time t_E:

$$t_E = \left(\frac{\Delta i_{LO}}{v_E}\right) L_O, \tag{75}$$

where Δi_{LO} is the peak to peak inductor current, shown in Fig. 8 and Fig. 10. Similarly, switches S_{GR} and S_O close to drain L_O with draining voltage v_D equals v_O across draining time t_D:

$$t_D = \left(\frac{\Delta i_{LO}}{v_D}\right) L_O. \tag{76}$$

A buck-boost can operate in either continuous conduction mode (CCM) or discontinuous conduction mode (DCM), and they need to be analyzed individually.

5.1.3.A. CCM

In continuous conduction mode [146], the inductor conducts current the entire switching cycle t_O, as shown in Fig. 5-5. Therefore, the power transferred by the inductor is its maximum energy minus its minimum energy

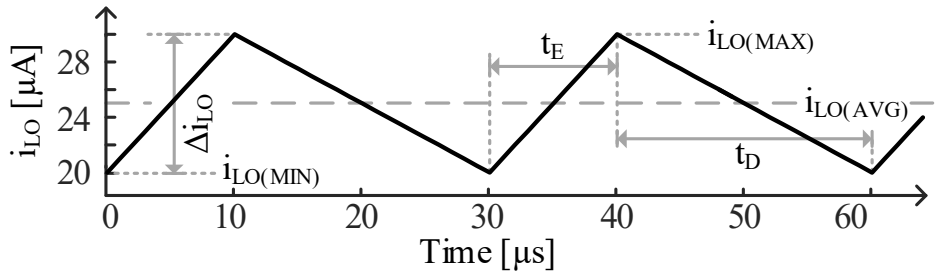

Figure 5-5. Inductor current waveform in continuous conduction mode.

$$\begin{aligned} P_O &= \left(E_{L(MAX)} - E_{L(MIN)}\right) f_O = 0.5 L_O \left(i_{LO(MAX)}{}^2 - i_{LO(MIN)}{}^2\right) f_O \\ &= L_O i_{LO(AVG)} \Delta i_{LO} f_O \approx P_{PZ} - P_X - P_B, \end{aligned} \tag{77}$$

where $i_{LO(AVG)}$ is the average inductor current, and $f_O = 1/t_O$ is the switching frequency. The energy transferred is also the drawn power from the piezoelectric transducer minus the losses on the recycler and the bridge.

Again, the transfers are not lossless. The inductors resistance R_{LO} burns ohmic power:

$$\begin{aligned} P_{R(LO)} &= {i_{LO(RMS)}}^2 R_{LO} = \left({i_{LO(DC)}}^2 + {i_{LO(AC.RMS)}}^2\right) R_{LO} \\ &= \left[{i_{LO(AVG)}}^2 + \left(\frac{0.5\Delta i_{LO}}{\sqrt{3}}\right)^2\right] L_X k_L. \end{aligned} \tag{78}$$

The energizing switches S_{EI} and S_{EG} burn ohmic power:

$$P_{R(EI/G)} = {i_{LO(RMS,E)}}^2 R_{EI/G} \left(\frac{t_E}{t_{SW}}\right) \propto \frac{{i_{LO(AVG)}}^2 + \left(\frac{0.5\Delta i_{LO}}{\sqrt{3}}\right)^2}{W_{EI/G}}, \tag{79}$$

where $i_{LO(RMS,E)}$, $R_{EI/G}$, and $W_{EI/G}$ are the RMS current, resistance, and width of S_{EI} and S_{EG}. Similarly, draining switches S_{DG} and S_{DO} burn

$$P_{R(DI/O)} = {i_{LO(RMS,D)}}^2 R_{DI/O} \left(\frac{t_D}{t_{SW}}\right) \propto \frac{{i_{LO(AVG)}}^2 + \left(\frac{0.5\Delta i_{LO}}{\sqrt{3}}\right)^2}{W_{DI/G}}, \tag{80}$$

where $i_{LO(RMS,D)}$, $R_{DG/O}$, and $W_{DG/O}$ are the RMS current, resistance, and width of S_{DG} and S_{DO}. All four switches require charge loss

$$P_{C(SW)} = q_C v_{DD} f_O. \tag{81}$$

From (6), the loss on all the switches P_{SW} is

$$P_{SW} = \sum P_{SE/D} \propto \sqrt{\left[i_{LO(AVG)}{}^2 + \left(\frac{0.5\Delta i_{LO}}{\sqrt{3}} \right)^2 \right] f_O} \,. \tag{82}$$

The total loss is the sum of (78) and (82), and with the help of (73), it can be reduced to a function of 2 variables, i.e. L_O and f_O. Since L_O is limited to 1 µH to 180 µH, by setting L_O and sweeping f_O, it is shown in Fig. 5-6 that the optimal CCM charger is with the following settings: L_O' is 180 µH, f_O' is 111 MHz, R_{LO}' is 10 Ω, $i_{LO(AVG)}'$ is 38.2 µA, $\Delta i_{LO}'$ is 50 µA. With the operation set, switches can be optimized from Section 5.1.1, with W_{EI}' at 1.2 µm, W_{EG}' at 860 nm, W_{DG}' at 1.2 µm, W_{DO}' at 1.5 µm, and total loss is 7.5 µW. Note that the width for 2 energizing switches are different, and similarly the width for 2 energizing switches are different, because S_{EI} and S_{DO} are PMOS, and S_{EG} and S_{DG} are NMOS.

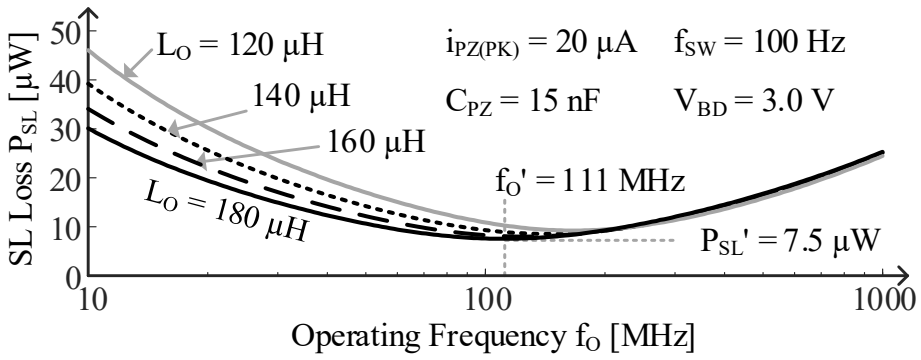

Figure 5-6. Total loss on optimized SL in CCM for different inductances.

5.1.3.B. DCM

In discontinuous conduction mode [151], on the other hand, the inductor does not conduct current across the entire switching cycle. Instead, the inductor is energized from 0 to $i_{LO(PK)}$ across t_E, and drained across t_D. After that, it stays at 0 current, until the next switching

cycle begins, as Fig. 5-7 shows. The input power is the power from the piezoelectric transducer minus the losses on the recycler and the bridge, and the energy transferred by the inductor is approximately the peak energy it holds:

$$P_O = 0.5 L_O {i_{LO(PK)}}^2 f_O - P_{SL} \approx P_{PZ} - P_X - P_B - P_{SL}, \tag{83}$$

where P_{SL} is the loss on the SL. Since drawn power P_{PZ}, loss on the recycler P_X, and loss on the bridge P_{BRG} are all known variables for the SL, the term $L_O {i_{LO(PK)}}^2 f_O$ is a constant

$$L_O {i_{LO(PK)}}^2 f_O \approx 2(P_{PZ} - P_X - P_B). \tag{84}$$

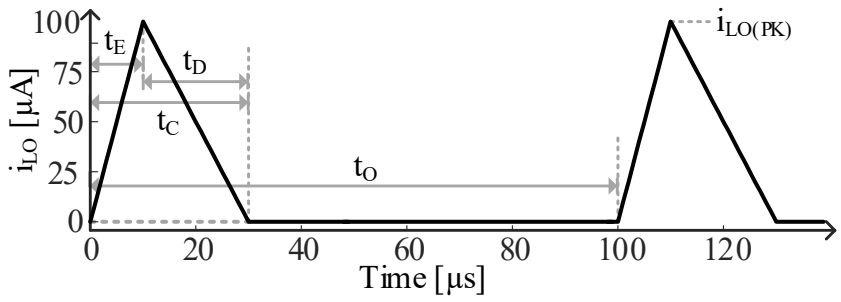

Figure 5-7. Inductor current waveform in discontinuous conduction mode.

The switched inductor in DCM still consumes ohmic loss on the inductor's resistance:

$$P_{R(LO)} = {i_{LO(RMS)}}^2 R_{LO} = \left(\frac{i_{LO(PK)}}{\sqrt{3}}\right)^2 R_{LO}\left(\frac{t_C}{t_O}\right)$$

$$= \left(\frac{i_{LO(PK)}}{\sqrt{3}}\right)^2 (L_O k_L)\left[\left(\frac{L_O}{v_E} + \frac{L_O}{v_D}\right) i_{LO(PK)}\right] f_O \tag{85}$$

$$\propto {i_{LO(PK)}}^3 {L_O}^2 f_O = 2(P_{PZ} - P_X - P_B) i_{LO(PK)} L_O \propto i_{LO(PK)} L_O.$$

The last step is because from (83), $L_O i_{LO(PK)}^2 f_O$ is constant. It also burns ohmic loss on the energizing switches S_{EI} and S_{EG}:

$$P_{R(EI/G)} = {i_{LO(RMS,E)}}^2 R_{EI/G} = \left(\frac{i_{LO(PK)}}{\sqrt{3}}\right)^2 R_{EI/G}\left(\frac{t_E}{t_O}\right)$$

$$= \left(\frac{i_{LO(PK)}}{\sqrt{3}}\right)^2 R_{EI/G}\left[\frac{i_{LO(PK)} L_O}{v_E}\right] f_O \tag{86}$$

$$\propto \frac{{i_{LO(PK)}}^3 L_O f_O}{W_{EI/G}} = 2(P_{PZ} - P_X - P_B)\frac{i_{LO(PK)}}{W_{EI/G}} \propto \frac{i_{LO(PK)}}{W_{EI/G}} \propto \frac{K_{R(MOS)}}{W_{EI/G}}.$$

Therefore, ohmic loss coefficient $K_{R(MOS)}$ is proportional to $i_{LO(PK)}$. Similarly, the draining switches S_{DG} and S_{DO} burn ohmic power:

$$P_{R(DI/G)} = {i_{LO(RMS,D)}}^2 R_{DI/G} = \left(\frac{i_{LO(PK)}}{\sqrt{3}}\right)^2 R_{EI/G}\left(\frac{t_D}{t_O}\right)$$

$$= \left(\frac{i_{LO(PK)}}{\sqrt{3}}\right)^2 R_{DI/G}\left[\frac{i_{LO(PK)} L_O}{v_D}\right] f_O \tag{87}$$

$$\propto \frac{{i_{LO(PK)}}^3 L_O f_O}{W_{DI/G}} = 2(P_{PZ} - P_X - P_B)\frac{i_{LO(PK)}}{W_{DI/G}} \propto \frac{i_{LO(PK)}}{W_{DI/G}} \propto \frac{K_{R(MOS)}}{W_{DI/G}}.$$

Again, the second to last step of (86) and (87) is because from (83), $L_O {i_{LO(PK)}}^2 f_O$ is a constant. The charge loss is the same as the CCM case in (81), and $K_{C(MOS)}$ is proportional to f_O. Therefore, the balanced ohmic loss and charge loss result in the optimum switch with total loss P_{SW}':

$$P_{SW}' = \sum P_{SE/D} \propto \sum 2\sqrt{K_{R(MOS)} K_{C(MOS)}}$$

$$\propto \sqrt{i_{LO(PK)} f_O} = \frac{\sqrt{i_{LO(PK)} f_O}\sqrt{i_{LO(PK)} L_O}}{\sqrt{i_{LO(PK)} L_O}} \propto \frac{1}{\sqrt{i_{LO(PK)} L_O}}. \tag{88}$$

The total loss on the SL is the sum of (85) and (88), and there is an optimum $i_{LO(PK)}L_O$ that yields the lowest total loss on the SL. In other words, no matter what inductor we choose, we can always modify to switches and controller accordingly such that it is least lossy, shown in the thick solid black trace in Fig. 5-8. The loss stays flat because for each inductance value, the $i_{LO(PK)}$ is inversely proportional to L_O so that their product stays constant. As a result, from (84), the optimum f_O is also proportional to L_O. It consumes P_{SL}' = 2.11 μW in the following optimal settings: L_O' is 130 μH, R_{LO}' is 7.2 Ω, f_O' is 40 kHz,

and $i_{LO(PK)}$' is 3.9 mA. With the waveforms set, the optimum switch size can be obtained from Section III: $W_{EI,G}$' is 459 µm and $W_{DG,O}$' is 640 µm. The thin traces in Fig. 11 also show the optimized losses with different inductor volume constraint. Therefore, DCM is less lossy than CCM, while operating at a much lower frequency, so we would operate it at DCM.

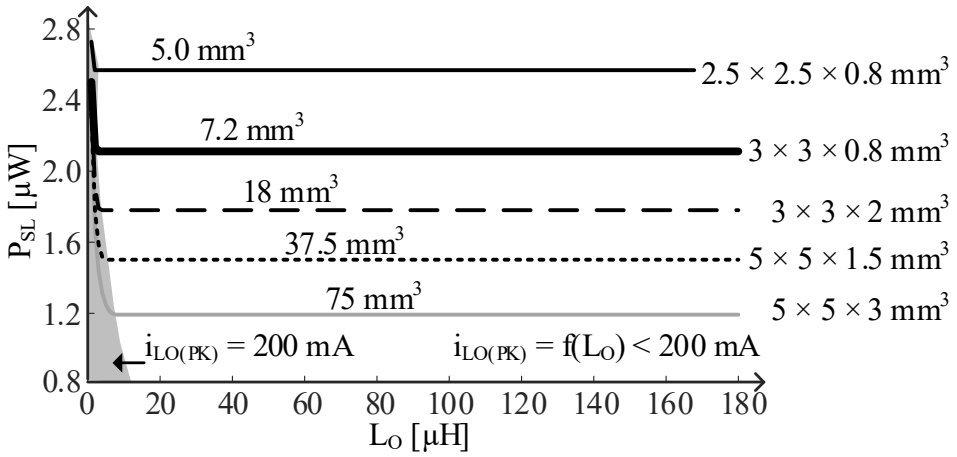

Figure 5-8. Total loss on optimized SL in CCM for different inductor volumes.

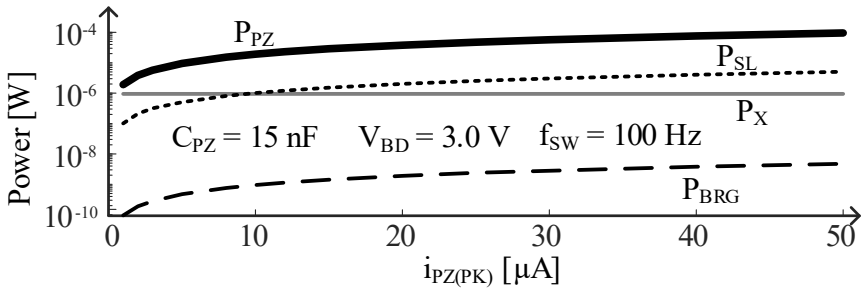

Figure 5-9. Drawn power and optimized losses across vibration strength.

5.1.4. Overall Performance

From the previous three sections, the optimum piezoelectric charger when the vibration provides 20 µA on the transducer is built. The charger draws 38.2 µW from P_{PZ}, and loses

944 nW on the recycler, 4.6 nW on the bridge, and 2.11 µW on the SL, resulting in an overall efficiency of 92%. Simulation of the circuits consumes 990 nW on the recycler, 8.6 nW on the bridge, and 2.35 µW on the SL, resulting in an overall efficiency of 91 %. Repeating the same process for $i_{PZ(PK)}$ from 1 µA to 50 µA, the results are presented in Fig. 5-9. P_{PZ}, P_{SL}, and P_D all scale linearly with vibration strength, but P_X does not. That is because the recycler operation is the same across all conditions, and the loss also remains the same.

5.2. **Synchronous Discharge: Series Switched-Inductor**

5.2.1. Design and Operation

The first basic objective of the charger proposed is to draw the power that C_{PZ} collects across each half cycle. For this, the switched-inductor bridge in Fig. 5-10 drains C_{PZ} between half cycles. This is why C_{PZ}'s voltage v_{PZ} in Fig. 5-11 falls to zero at 4.2, 8.4, and 13 ms. The second aim is to pre-charge the transducer before drawing power each half cycle to raise the damping force across the half cycle. The bridge does this by using some of the energy drawn to pre-charge C_{PZ} to v_{PC} before every half cycle begins (at 4.2, 8.4, and 13 ms). v_{PZ} therefore starts at v_{PC} and rises to $v_{PC} + \Delta v_{PZ(OC)}$ and is never less than v_{PC}, except during half-cycle transitions.

To start this, all but bottom ground switch M_{GB} open across i_{PZ}'s positive half cycle, so the bridge open-circuits and i_{PZ} charges C_{PZ} to $v_{PZ(PK)}$ across 0.1–4.2 ms in Fig. 5-11. Top ground switch M_{GT} then closes to drain C_{PZ} into transfer inductor L_X. As L_X energizes, v_{PZ} falls to zero and L_X's current i_L in Fig. 5-12 rises (across t_E at 4.167–4.170 ms). M_{GB} and M_{GT} remain closed for another short interval t_{D1} to partially drain L_X into C_{PZ}, and that

way, pre-charge C_{PZ} in the negative direction. M_{GT} opens and top battery switch M_{BT} closes after t_{D1} across t_{D2} to deplete L_X into the battery v_B and C_{PZ}. So v_B charges and C_{PZ} pre-charges further to pre-charging target $-v_{PC}$ in Fig. 5-11.

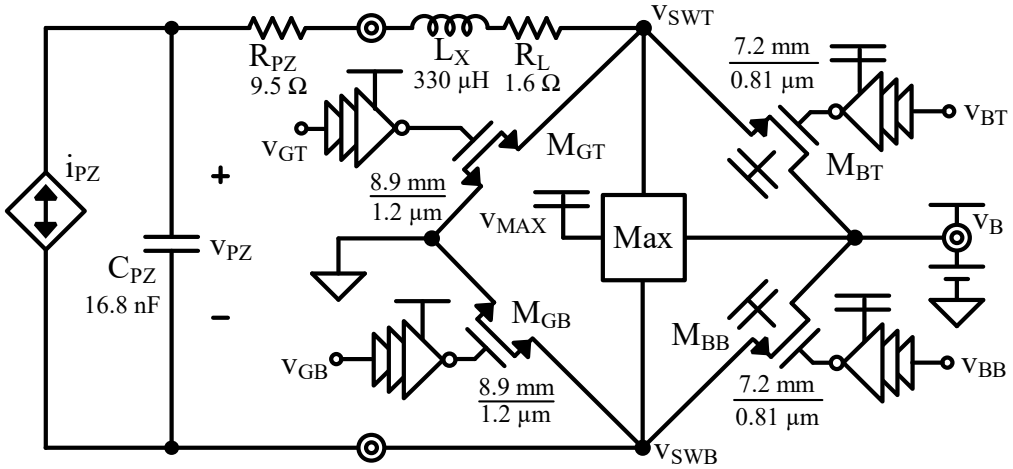

Figure 5-10. Proposed piezoelectric-powered series switched-inductor bridge.

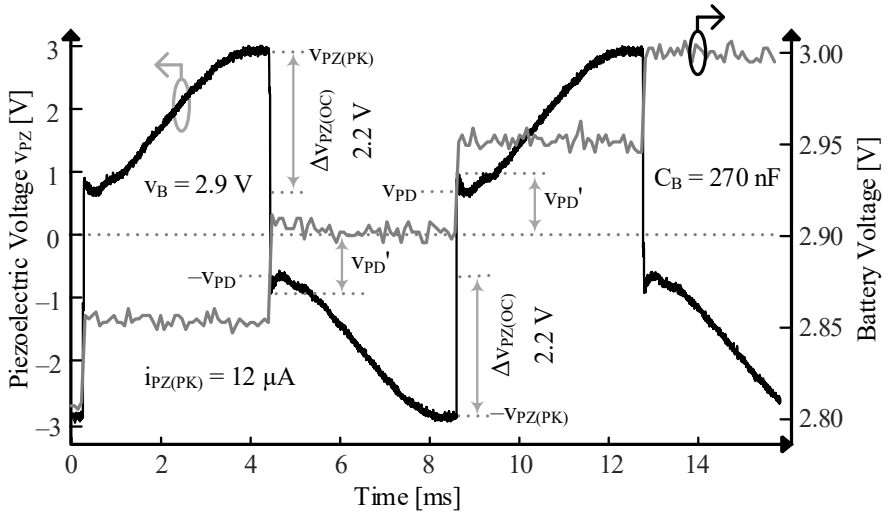

Figure 5-11. Measured piezoelectric voltage.

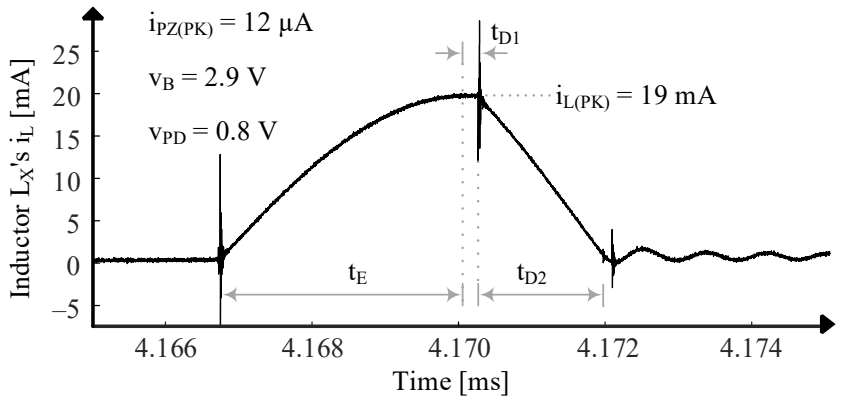

Figure 5-12. Measured inductor current at the end of a positive half cycle.

The process repeats for a negative half cycle. In this case, all but M_{GT} open across 4.2–8.4 ms in Fig. 5-11, so i_{PZ} charges C_{PZ} from $-v_{PC}$ to $-v_{PZ(PK)}$. M_{GB} then closes at 8.320 ms in Fig. 5-11 to drain C_{PZ} into L_X (across t_E) and a little longer (across t_{D1}) to partially drain L_X into C_{PZ}. M_{GB} opens and M_{BB} closes after that across t_{D2} to deplete L_X into v_B and C_{PZ}. This way, v_B receives charge and C_{PZ} pre-charges to v_{PC} in Fig. 5-11. Table 5-1 tabulates the switching sequences. To illustrate the charging profile, a 270-nF capacitor replaces the battery, and the grey trace in Fig. 5-11 shows that the battery voltage goes up by about 50 mV between every half cycle. Fig. 5-14 shows that the charger can work with a wide range of battery voltage, as it charges the 270-nF capacitor from 2.7 V to 4.2 V.

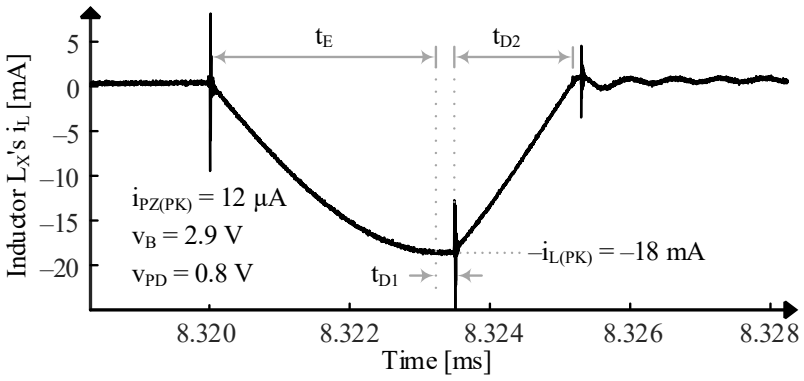

Figure 5-13. Measured inductor current at the end of a negative half cycle.

Table 5-1. Switching sequence for series inductor switch bridge

State	M_{GT}	M_{GB}	M_{BT}	M_{BB}
Positive half	Open	Closed	Open	Open
Positive t_E	Closed	Closed	Open	Open
Positive t_{D1}	Closed	Closed	Open	Open
Positive t_{D2}	Open	Closed	Closed	Open
Negative half	Open	Open	Open	Closed
Negative t_E	Open	Open	Closed	Closed
Negative t_{D1}	Open	Open	Closed	Closed
Negative t_{D2}	Closed	Open	Open	Closed

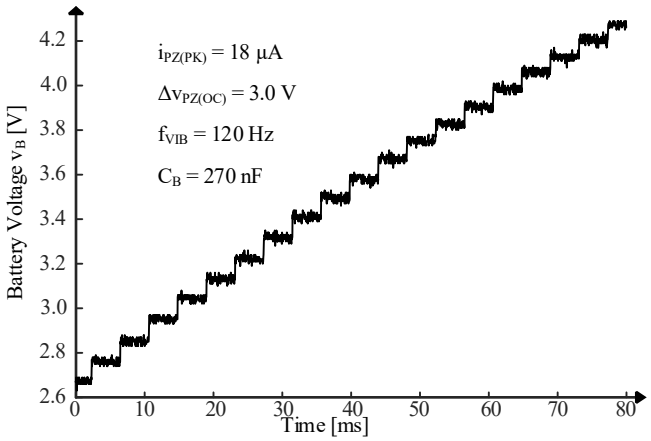

Figure 5-14. Measured inductor current at the end of a negative half cycle.

5.2.1.A. Power Transistors

The switches require gate-drive power P_G to switch and ohmic power P_R to conduct. Since gate capacitance C_G and channel resistance R_{CH} increase with channel length L_{CH}, L_{CH} should be minimum length L_{MIN}. The minimum length L_{MIN} than can withstand 5.5 V is 1.2 µm for NFETs and 0.81 µm for PFETs. But since C_G increases and R_{CH} decreases with wider channels, as discussed in Section 5.1.1, channel widths W_{CH} in Fig. 5-10 balance P_G and P_R when the system draws 30 µW from i_{PZ}, which corresponds to the most probable vibration strength. Optimizing W_{CH} for the most likely condition saves, and as a result, outputs the most power.

5.2.1.B. Drivers

Three inverters with transistors of increasing dimensions drive each switch. The third inverter is 5× larger than the second, the second 5× larger than the first, and the first is minimum size. Although 2.67× is optimal for shortest delay, a higher gain reduces the number of inverter stages and the shoot-through power they consume.

Since NFETs connect to ground and ground is the lowest potential in the circuit, NFETs can open and close with ground and the voltage that a lithium-ion battery can furnish: 2.7–4.2 V. This is why the supplies for NFET drivers are v_B and ground. For PFETs to open, their gates must charge to the highest terminal voltage. PFETs here connect to v_B and switching nodes v_{SWT} and v_{SWB}, which rise to a level $v_{PZ(PK)}$ (in Fig. 5-11) that depends on pre-charging voltage v_{PC} and vibration strength $\Delta v_{PZ(OC)}$. This means, v_{SWT} and v_{SWB} may or may not surpass v_B, so v_B is not a good supply for PFET drivers.

5.2.1.C. Maximum-Supply Selector

The purpose of the maximum-supply selector block Max in Fig. 5-10 is to establish the highest supply v_{MAX} with which PFET drivers can open P-type switches. For this, cross-coupled PFET pair M_{1A}–M_{1B} in Fig. 5-15 selects and connects the higher of v_{SWT} and v_{SWB} to v_{O1}: M_{1A} connects v_{SWT} to v_{O1} when v_{SWB} is below v_{SWT} by a more than a PFET threshold voltage $|v_{TP}|$ and M_{1B} connects v_{SWB} when the opposite is true. M_{2A}–M_{2B} similarly selects and connects the higher of the resulting v_{O1} and v_B to v_{MAX}. So together, v_{MAX} is the highest of the three:

$$\mathbf{v_{MAX} = Max\left\{v_{O1}, v_B\right\} = Max\left\{v_{SWT}, v_{SWB}, v_B\right\}.} \tag{89}$$

v_{MAX} in Fig. 5-16, for example, connects to v_B at 1.6–3.2 ms because v_B's 2.9 V exceeds v_{SWT}'s 0–2.9 V and v_{SWB}'s 0 V. v_{MAX} connects to v_{SWT} at 3.2–5.2 ms because v_{SWT}'s 2.9–4.5 V similarly surpasses v_B's 2.9 V and v_{SWB}'s 0 V. v_{MAX} then connects to v_{SWB} at 7.2–9.4 ms because v_{SWB}'s 2.9–4.5 V is greater than v_B's 2.9 V and v_{SWT}'s 0 V.

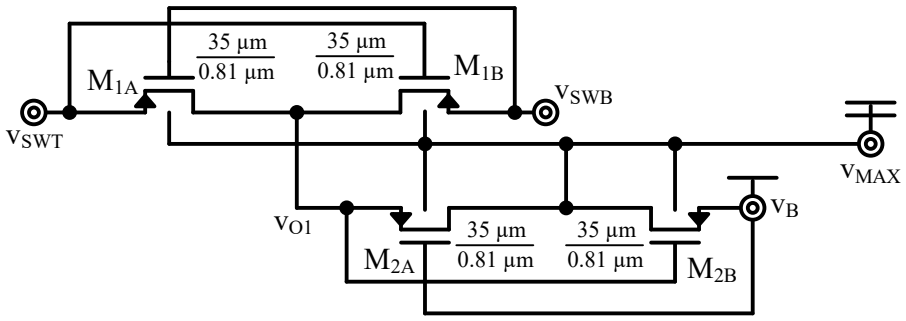

Figure 5-15. Maximum-supply selector.

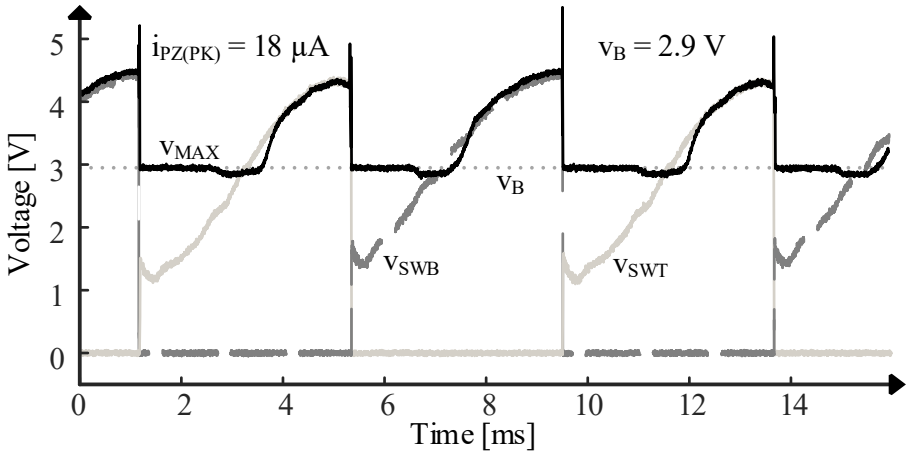

Figure 5-16. Measured supply waveforms.

Although M_{1A}, M_{1B}, M_{2A}, and M_{2B} do not conduct as much current as power NFETs and PFETs in Fig. 5-10, they nevertheless supply the charge that PFET gates in Fig. 5-10 require to switch between states. This is why their channel lengths (in Fig. 5-15) are the shortest that can withstand 5.5 V. Their channel widths ensure M_{1A}, M_{1B}, M_{2A}, and M_{2B} drop less than 100 mV when charging PFET gates in Fig. 5-10.

PFETs in a pair do not close when their terminal (gate) voltages are within a threshold $|v_{TP}|$ of one another. Here, however, M_{1A}–M_{1B}'s v_{SWT} and v_{SWB} are within a $|v_{TP}|$ only between half cycles across 2–4-µs transitions, when M_{GT} and M_{GB} connect v_{SWT} and

v_{SWB} to ground. This is not a problem because v_B is much greater than v_{SWT} and v_{SWB} during this time, so M_{2B} connects v_B to v_{MAX}.

M_{2A}–M_{2B}'s v_{O1} and v_B are within a $|v_{TP}|$ only when C_{PZ} charges high enough to be within a $|v_{TP}|$ of v_B, which does not always happen. If $v_{PZ(PK)}$ is well above v_B, for example, v_{SWT} and v_{SWB} are within a $|v_{TP}|$ of v_B only when v_{SWT} and v_{SWB} cross v_B. This does not present a problem because transitions are short and PFET gates do not require charge halfway across transitions. But even if v_{PZ} peaks within a $|v_{TP}|$ of v_B, M_{1A}–M_{1B} and M_{2A}–M_{2B}'s combined bulk-to-substrate capacitance C_{BULK} is large enough to hold and supply the charge that PFET gates in Fig. 5-10 require across this short interval. Although adding capacitance helps, C_{BULK} adds to C_{PZ} when v_{SWT} or v_{SWB} is higher than v_B, so C_{BULK} steers i_{PZ} away from C_{PZ}. In other words, adding capacitance sacrifices power.

The worst-case condition occurs when v_{SWT} and v_{SWB} cross v_B within half cycles (at 3.2, 7.4, and 12 ms in Fig. 5-16). During these millisecond crossings, v_{MAX} is a $|v_{TP}|$ below v_{SWT} and v_{SWB}. With $|v_{TP}|$ of gate drive, however, battery PFETs M_{BT} and M_{BB} in Fig. 5-10 are in weak inversion. So although their effect is to leak v_B to ground and C_{PZ} to v_B, leakage is low because these PFETs are very resistive in weak inversion.

5.2.2. Features

The system draws *between* half cycles what C_{PZ} collects *across* half cycles. The energy E_{PC} that C_{PZ} requires to pre-charge to pre-charging level v_{PC} essentially cycles between C_{PZ} and L_X. So of the energy drawn when v_{PZ} peaks (E_{PK}), i_{PZ} sources the difference $E_{PK} - E_{PC}$ every half cycle and twice that difference $2(E_{PK} - E_{PC})$ every full cycle t_{VIB}.

Since i_{PZ} charges C_{PZ} across $\Delta v_{PZ(OC)}$ every half cycle, v_{PZ} increases from v_{PC} (at 4.2, 8.4, and 13 ms in Fig. 5-11) to $v_{PC} + \Delta v_{PZ(OC)}$ or $v_{PZ(PK)}$. C_{PZ}'s peak energy E_{PK} or $0.5C_{PZ}v_{PZ(PK)}^2$ is therefore $0.5C_{PZ}(v_{PC} + \Delta v_{PZ(OC)})^2$. And after subtracting E_{PC}'s $0.5C_{PZ}v_{PC}^2$, drawn piezoelectric power P_{PZ} reduces to

$$P_{PZ} = 2\left(\frac{E_{PK} - E_{PC}}{T_{VIB}}\right) = 2\left(0.5C_{PZ}{v_{PZ(PK)}}^2 - 0.5C_{PZ}{v_{PC}}^2\right)f_{VIB}$$

$$= C_{PZ}\left({\Delta v_{PZ(PC)}}^2 + 2v_{PC}\Delta v_{PZ(OC)}\right)f_{VIB}, \tag{90}$$

where f_{VIB} is the frequency of vibrations.

The underlying assumption here is that, as discussed in Chapters 2 and 3, P_{PZ}'s load to motion is negligible, which is the case for small piezoelectric devices. As a result, i_{PZ} is nearly independent of P_{PZ}, which is another way of saying i_{PZ} can source much more power than i_{PZ} *actually* supplies. This is why pre-charging C_{PZ} is so important, because v_{PC} raises the voltage v_{PZ} with which i_{PZ} sources P_{PZ}. And with a higher v_{PZ}, i_{PZ} sources more power.

5.2.3. Limitations

The mechanical properties of the transducer dictate how much piezoelectric capacitance C_{PZ} appears across its terminals. In the case of the unit tested, C_{PZ} in Fig. 5-17 is 16.8 nF at the vibration frequency f_{VIB}: at 120 Hz. This is the capacitance that collects piezoelectric charge across half cycles.

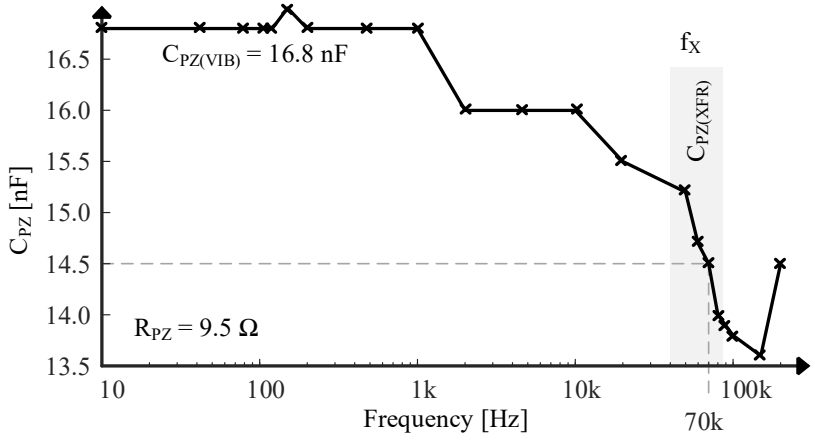

Figure 5-17. Measured piezoelectric capacitance across frequency.

Interestingly, C_{PZ} falls as frequency climbs. This is not unreasonable because uneven distribution of so much series resistance R_{PZ} steers more current into capacitive components with lower resistance. This is why 14.5 nF of the 16.8 nF available activate when transferring energy at 70 kHz.

Here, 40–80 kHz corresponds to the 2–4 μs that L_X requires to transfer C_{PZ}'s energy between half cycles. In other words, a lower average capacitance $C_{PZ(XFR)}$ of 14.5 nF transfers between half cycles what the higher counterpart C_{PZ} collects across half cycles. $C_{PZ(XFR)}$ therefore transfers the pre-charging charge q_{PC} needed to pre-charge C_{PZ} to v_{PC}:

$$q_{PC} = C_{PZ}v_{PD} = C_{PZ(XFR)}v_{PC}'. \tag{91}$$

Except, this same q_{PC} establishes a higher voltage v_{PC}' across $C_{PZ(XFR)}$'s lower capacitance. This is why C_{PZ}'s pre-charging level in Fig. 5-11 falls slightly at the beginning of every half cycle, because $C_{PZ(XFR)}$'s v_{PC}' drops to C_{PZ}'s v_{PC}.

This is unfortunate because a linear rise in voltage produces a quadratic rise in energy that outpaces a linear fall in capacitance. In other words, $C_{PZ(XFR)}$ requires more

energy (E_{XFR}) than C_{PZ} requires (E_{VIB}) to charge C_{PZ} to v_{PC}. Series resistances in C_{PZ} burn this difference $E_{XFR} - E_{VIB}$ every half cycle and twice every full cycle t_{VIB}, so this loss P_{CPZ} is

$$P_{PZ} = 2\left(\frac{E_{XFR} - E_{VIB}}{T_{VIB}}\right) = 2\left(0.5C_{PZ(XFR)}{v_{PC}}'^2 - 0.5C_{PZ}{v_{PC}}^2\right)f_{VIB}$$

$$= \left[C_{PZ(XFR)}\left(\frac{C_{PZ}v_{PC}}{C_{PZ(XFR)}}\right)^2 - C_{PZ}{v_{PC}}^2\right]f_{VIB} = C_{PZ}{v_{PC}}^2\left(\frac{C_{PZ}}{C_{PZ(XFR)}} - 1\right)f_{VIB}. \quad (92)$$

Note P_{CPZ} vanishes when $C_{PZ(XFR)}$ and C_{PZ} match, when all capacitive components in the transducer transfer energy between half cycles. Also notice P_{CPZ} scales with v_{PC}, so P_{CPZ} climbs when v_{PC} rises. Plus, the series resistance R_{PZ} that transfers the power at 40–80 kHz burns ohmic losses P_{RPZ}. So imperfections in the transducer ultimately cost the system ohmic and dynamic losses P_{RPZ} and P_{CPZ}.

5.2.4. Maximum Output Power

Loss Limit: Power losses P_{LOSS} limit how much of the piezoelectric power P_{PZ} drawn the system can deliver. Unfortunately, all components lose power. The transducer loses ohmic power P_{RPZ} to R_{PZ} and dynamic power P_{CPZ} when pre-charging C_{PZ}. The inductor L_X's series resistance R_L also burns ohmic power P_{RL}. MOS transistors consume ohmic power P_{MR} to conduct and require gate-drive power P_{MG} to switch. Plus, drivers burn shoot-through power P_{ST} when they transition. And although not nearly as much, power PFETs leak piezoelectric and battery power P_{LK} when the switching nodes v_{SWT} and v_{SWB} cross v_B and C_{BULK} leaks piezoelectric power P_B away from C_{PZ} when v_{SWT} and v_{SWB} surpass v_B. So of P_{PZ}, the battery v_B receives $P_{PZ} - P_{LOSS}$, where P_{LOSS} is

$$P_{LOSS} = P_{RPZ} + P_{CPZ} + P_{RL} + P_{MR} + P_{MG} + P_{ST} + P_{LK} + P_{B}. \quad (93)$$

Conversion efficiency η_C is therefore the fraction of P_{PZ} that all these losses P_{LOSS} in the system avail with output power P_O:

$$\eta_C = \frac{P_O}{P_{PZ}} = \frac{P_{PZ} - P_{LOSS}}{P_{PZ}} = 1 - \frac{P_{LOSS}}{P_{PZ}}. \quad (94)$$

Notice that fractional losses P_{LOSS}/P_{PZ} set this efficiency.

Since ohmic losses P_R climb with L_X's (root–mean–squared) conduction current $i_{L(RMS)}$ and $i_{L(RMS)}$ climbs with piezoelectric power P_{PZ}, losses P_{RPZ}, P_{RL}, and P_{MR} increase with P_{PZ}. But while P_{PZ} rises linearly with $i_{L(RMS)}$, P_R grows quadratically (with $i_{L(RMS)}^2 R_{EQ}$) across resonant transfers (t_E and t_{D1} in Figs. 5-12 and 5-13) and cubically (with $i_{L(RMS)}^3 R_{EQ}$) across battery transfers (t_{D2} in Figs. 5-12 and 5-13), as discussed in Chapter 4. This means that, when vibration strength is low, an increase in P_{PZ} exceeds the rise in P_R to produce a net gain in P_O. Eventually, however, P_R's quadratic-to-cubic loss outpaces P_{PZ}'s linear gain to the extent that P_O falls. Plus, P_{CPZ} also increases quadratically with pre-damping voltage v_{PD}. So even though P_{PZ} rises monotonically across pre-damping voltage v_{PD}'s entire 0 to 4 V range in Fig. 5-18, P_O maxes at 12 μW when vibration strength peaks i_{PZ} to 12 μA and charges C_{PZ} across 2.0 V.

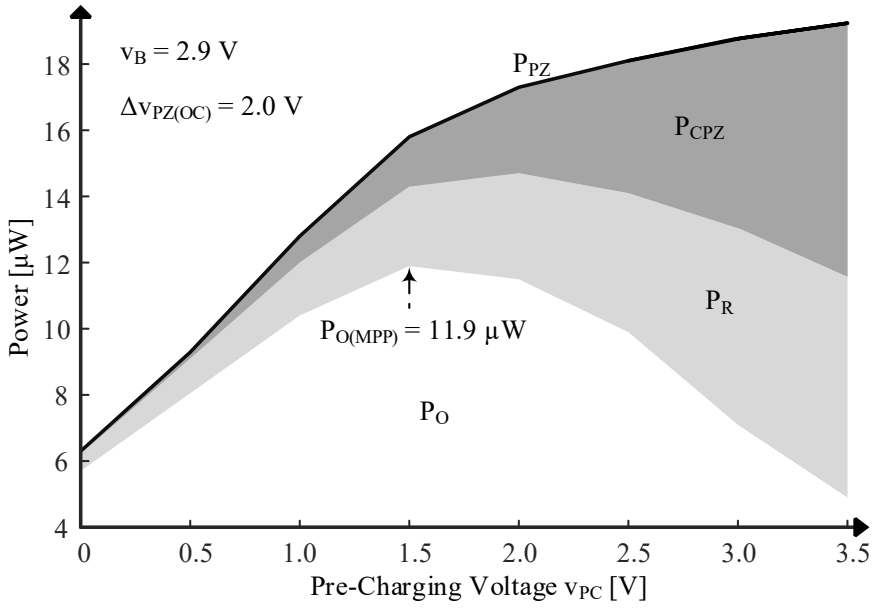

Figure 5-18. Measured power across pre-damping voltage.

As vibrations gain strength, P_R's rise cancels P_{PZ}'s gain at higher power levels. This is why the maximum power point $P_{O(MPP)}$ in Fig. 5-19 climbs with $i_{PZ(PK)}$ up to 21 µA. As this happens, P_{RPZ}, P_{RL}, and P_{MR} rise, but not P_{MG} and P_{ST} because gate-drive losses and shoot-through power do not scale with vibration strength. P_{RPZ} and P_{RL} dominate because R_{PZ} and R_L in small devices are much higher at 1–10 Ω than MOS resistances, which engineers normally keep at milliohms. In other words, scaling down the size of the transducer and inductor produces the dominant losses that limit $P_{O(MPP)}$.

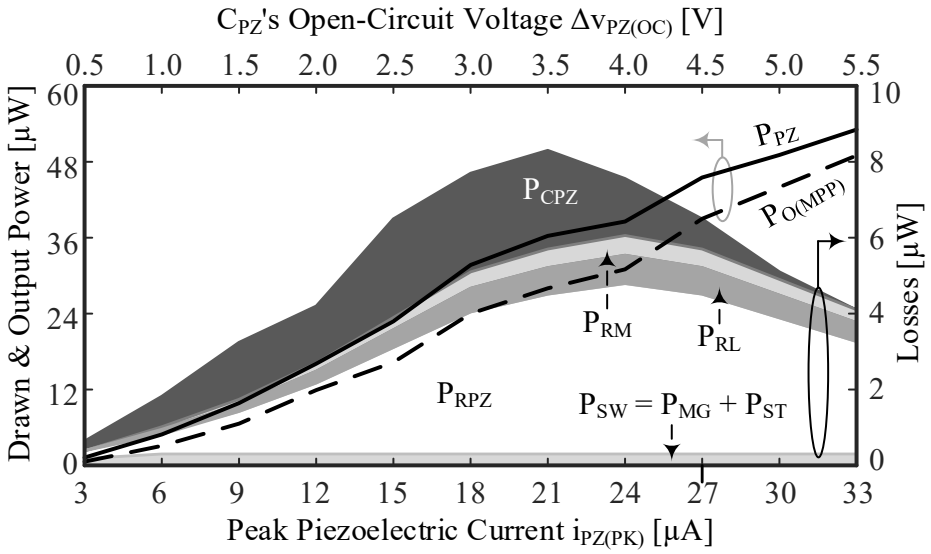

Figure 5-19. Measured output power and losses.

Since the power P_{CPZ} that C_{PZ} loses when pre-charging scales with v_{PD} and v_{PD} increases with vibration strength in this region, P_{CPZ} also climbs with $\Delta v_{PZ(OC)}$ up to 3.5 V. In all, the system delivers 45%–91% of the 1.2–55 µW that i_{PZ} sources with P_{PZ}. Conversion efficiency η_C is lower when vibrations are weak because switching losses P_{MG} and P_{ST}, which do not scale with $\Delta v_{PZ(OC)}$, dominate when P_{PZ} is low.

Breakdown Limit: Recall that C_{PZ}'s voltage v_{PZ} is the voltage with which the piezoelectric current i_{PZ} sources power P_{PZ}. So i_{PZ} outputs more power with a higher v_{PZ}. The switched inductor here raises v_{PZ} by pre-charging C_{PZ} to v_{PD} before every half cycle begins. This way, i_{PZ} charges C_{PZ} to a higher peak $v_{PZ(PK)}$: to $v_{PD} + \Delta v_{PZ(OC)}$ instead of $\Delta v_{PZ(OC)}$. But since C_{PZ} exposes the switches in the bridge to this $v_{PZ(PK)}$, $v_{PZ(PK)}$ cannot exceed the transistors' breakdown level V_{BD}:

$$v_{PZ(PK)} = v_{PD} + \Delta v_{PZ(OC)} \leq V_{BD}. \tag{95}$$

$v_{PZ(PK)}$ does not exceed V_{BD} when losses limit maximum output power $P_{O(MPP)}$, like in Figs. 8 and 9 when $i_{PZ(PK)}$ is below 21 µA. Above 21 µA, however, additional losses P_{LOSS} balance gains in piezoelectric power P_{PZ} at levels that require $v_{PZ(PK)}$ to surpass V_{BD}. Under such conditions, V_{BD} limits $v_{PZ(PK)}$, and with $v_{PZ(PK)}$, limit $P_{O(MPP)}$ before P_{LOSS} does. So as stronger vibrations raise $\Delta v_{PZ(OC)}$ above 3.5 V in Figs. 10 and 11, the system reduces C_{PZ}'s pre-damping level v_{PC} to keep $v_{PZ(PK)}$ from exceeding V_{BD}'s 5.5-V level. This is why C_{PZ}'s loss P_{CPZ} falls in this region, because P_{CPZ} scales with v_{PD} and v_{PD} drops when $\Delta v_{PZ(OC)}$ surpasses 3.5 V.

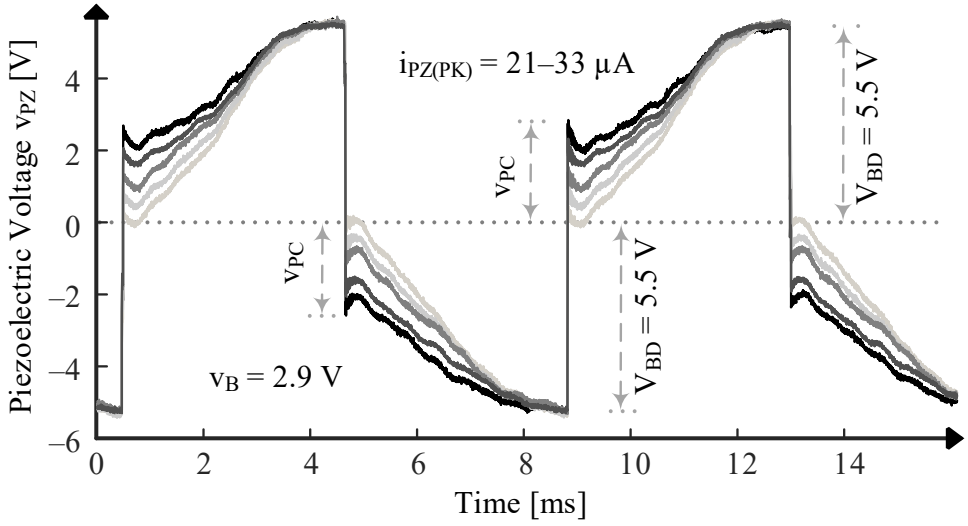

Figure 5-20. Measured piezoelectric voltage when breakdown limits v_{PZ}.

v_{PZ}'s breakdown boundary limits $v_{PC} + \Delta v_{PZ(OC)}$ to V_{BD}, and that way, limits the maximum power $P_{PZ(MAX)}$ that i_{PZ} can supply to

$$P_{PZ(MAX)} = P_{PZ}|_{v_{PC}+\Delta v_{PZ(OC)}=V_{BD}} = C_{PZ}\left(2V_{BD}\Delta v_{PZ(OC)} - \Delta v_{PZ(OC)}{}^2\right)f_{VIB}. \quad (96)$$

But to be clear, $P_{PZ(MAX)}$ still under-damps the transducer to such a degree that i_{PZ} can easily supply more power. The circuit, however, is the ultimate bottleneck that limits P_{PZ} to $P_{PZ(MAX)}$. This is why the trajectory of the maximum power point in Fig. 5-21 shifts when vibrations charge C_{PZ} across 3.5 V, because losses P_{LOSS} limit $P_{O(MPP)}$ below 3.5 V and breakdown voltage V_{BD} limits $P_{O(MPP)}$ above 3.5 V.

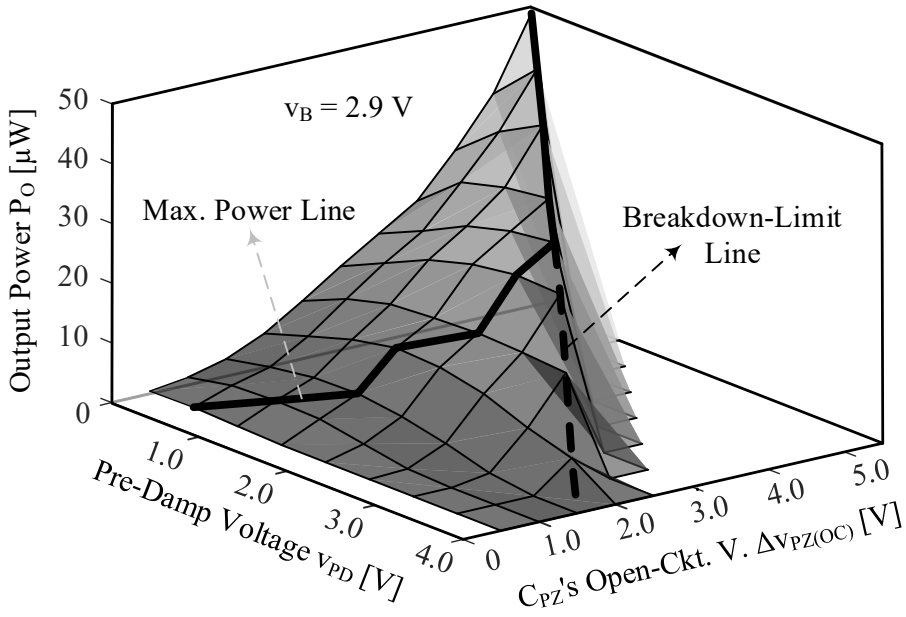

Figure 5-21. Measured power across vibration strength and pre-damping levels.

Interestingly, ohmic losses P_R in Fig. 5-18 fall as stronger vibrations raise $\Delta v_{PZ(OC)}$ above 4.0 V. Before this happens, the switched inductor depletes C_{PZ} into L_X so, while L_X charges the battery v_B, L_X can pre-charge C_{PZ} to v_{PC}. When $\Delta v_{PZ(OC)}$ surpasses 4.0 V, however, V_{BD} keeps v_{PC} so low that C_{PZ}'s energy E_{PK} is too much for L_X to pre-charge C_{PZ} to v_{PD}. So before C_{PZ} finishes draining into L_X, the system steers some of this energy E_{PK} to v_B. As a result, L_X receives and transfers less energy, and with less conduction, series resistances burn less ohmic power P_R. And since fractional losses P_{LOSS}/P_{PZ} are lower, power-conversion efficiency η_C rises in this region.

5.3. **Recycling: Switched-Inductor Bridge**

5.3.1. Operation

The proposed charger, shown in Fig. 5-22, consists of the piezoelectric transducer i_{PZ} and C_{PZ}, an inductor L_X, the switch network, and the battery v_B. At steady-state, the voltage across the piezoelectric transducer v_{PZ} is always near the breakdown voltage V_{BD} across the positive half cycles, and $-V_{BD}$ across the negative half cycles. S_{GI-} closes across positive half cycle to connect the bottom plate of C_{PZ} to ground, while S_{GI+} closes across positive half cycle to connect the top plate of C_{PZ} to ground. This way, no negative voltage appears in the system, and the need of the negative supply is removed.

When the controller senses that v_{PZ} is at the breakdown voltage, the charger collects a portion of the charge to energize the inductor, and then charge the battery. After each battery charging transfer, the voltage across the capacitor drops by Δv_{PZ}, as shown in Fig. 5-19. Between half cycles, on the other hand, the inductor collects all the charge from C_{PZ}, and then puts it into the opposite direction back into C_{PZ}. As a result, the charger recycles the charge from C_{PZ}, and v_{PZ} can be close to V_{BD} across the entire half cycle.

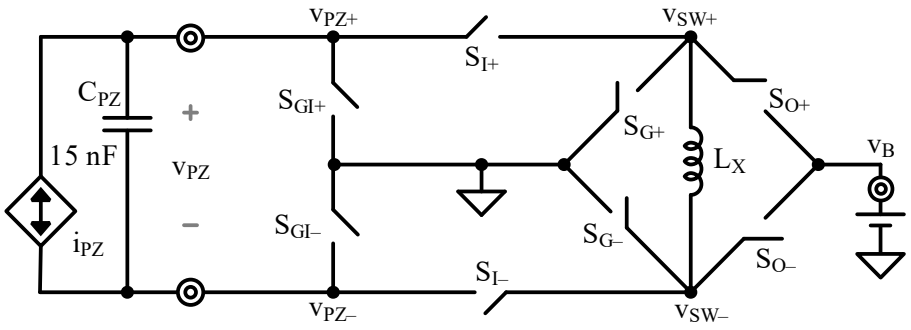

Figure 5-22. Schematic of the Recycling Switched-Inductor.

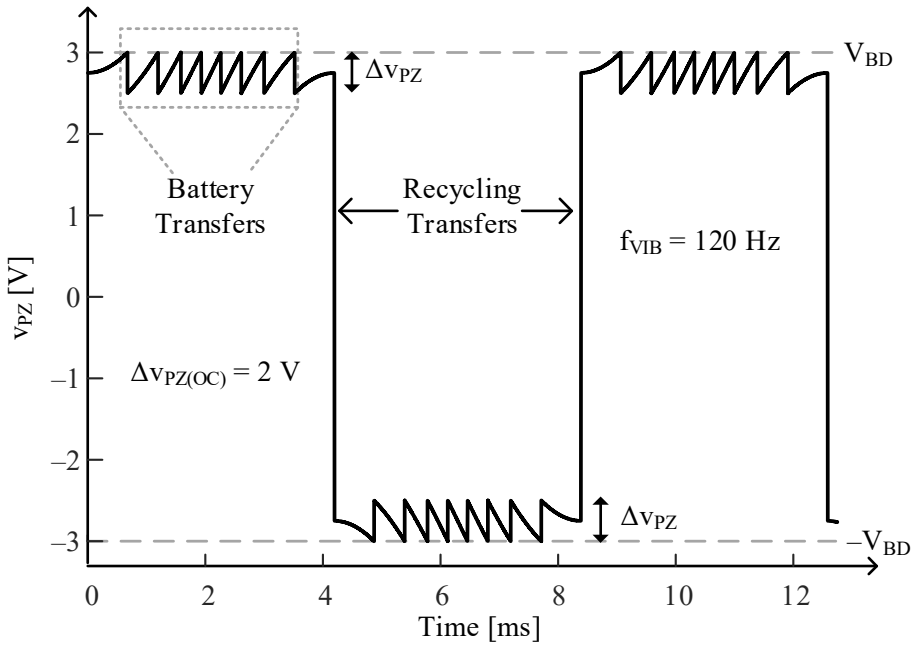

Figure 5-23. Simulated piezoelectric voltage v_{PZ}.

Because the time constant of the LC is within 5 µs, while the half cycle is usually 10s of milliseconds, the transfer is nearly instantaneous. This way, v_{PZ} is always between $V_{BD} - \Delta v_{PZ}$ and V_{BD} across a half cycle.

5.3.1.A. Battery-Charging Transfers

The battery-charging transfers take a small portion of the charge from the piezoelectric capacitor and charge the battery. Because the power stage is completely symmetrical, only the transfers in the positive half cycle is detailed below. The transfers in the negative half cycle is the same in the opposite direction. The inductor first energizes with switches S_{I+} and S_{I-}, and drains with switches S_{G+} and S_{O-}. Its measured inductor current is shown by the gray traces in Fig. 5-224 and Fig. 5-25 with different peak piezoelectric voltage $v_{PZ(PK)}$ (3.0 V and 1.0 V, respectively), battery voltage (1.5 V and 2.5 V, respectively), and (500

mV and 200 mV, respectively). The gray traces are labeled “indirect”, because C_{PZ} never directly transfers any portion of the energy directly into v_B.

The battery-charging transfers can also incorporate “direct” transfers [151]. The black trace in Fig. 5-24 shows the direct-indirect transfer, where the inductor energizes with switches S_{GI-} S_{I+}, and S_{O-}, and drains with switches S_{G+} and S_{O-} During energizing, the energizing voltage is reduced by vB, therefore lowing the peak inductor current. The capacitor transfers a portion of the energy directly into the battery during energizing, allowing the inductor to carry less energy than that transferred. Even though the total transfer time is longer, the total loss is lower [151]. Note that in order for the inductor to start energizing, battery voltage has to be lower than the peak piezoelectric voltage. This is usually the case because to draw the most power, $v_{PZ(PK)}$ is V_{BD}, and the battery voltage v_B has to be lower than that.

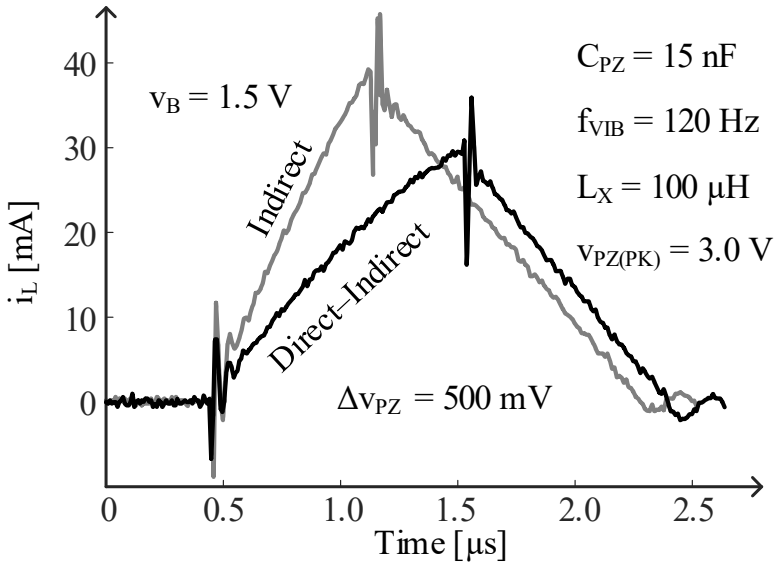

Figure 5-24. Measured i_L for battery transfers when Δv_{PZ} is 500 mV.

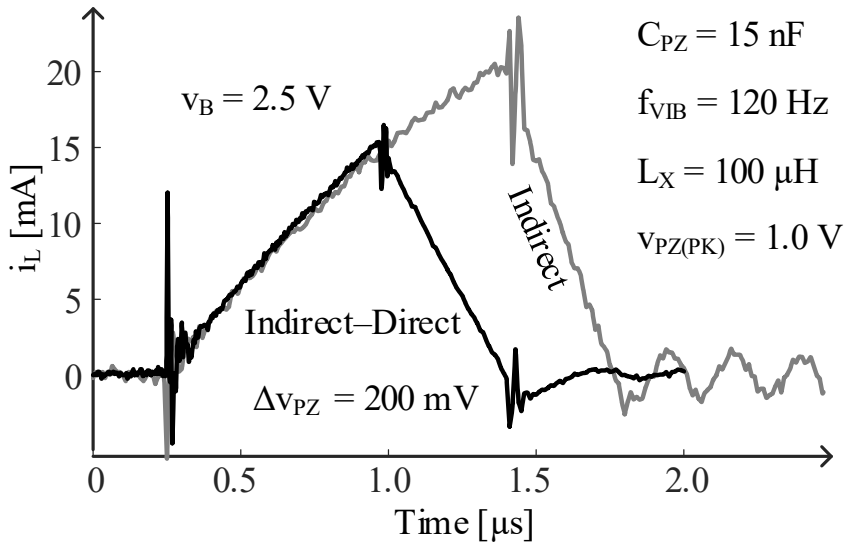

Figure 5-25. Measured i_L for battery transfers when Δv_{PZ} is 200 mV.

However, there are cases when the vibration strength is low that the maximum power point is when the $v_{PZ(PK)}$ is lower than the battery voltage. In that case, the direct–indirect scheme can no longer be used. However, the indirect–direct scheme can work, as shown in the black trace in Fig. 5-25. The inductor first energizes with switches S_{I+} and $S_{I–}$ and drains into both C_{PZ} and v_B with switches $S_{GI–}$, S_{I+}, and $S_{O–}$. Because v_{PZ} keeps dropping in the drain phase, the energizing phase can be cut short, allowing the inductor to again carry less energy than the transferred energy, saving ohmic power loss. The switching configurations for each transfer is listed in Table 5-2.

Table 5-2. Switching configurations for recycling switched-inductor

Transfer Mode	Half Cycle	Transfer	Switches Engaged
Battery Charging Transfers	+	Indirect Energize	S_{GI-}, S_{I+}, S_{I-}
		Indirect Drain	S_{GI-}, S_{G+}, S_{O-}
		Direct Energize	S_{GI+}, S_{I+}, S_{O-}
		Direct Drain	S_{GI+}, S_{I+}, S_{O-}
	–	Indirect Energize	S_{GI+}, S_{I-}, S_{I+}
		Indirect Drain	S_{GI+}, S_{G-}, S_{O+}
		Direct Energize	S_{GI-}, S_{I-}, S_{O+}
		Direct Drain	S_{GI-}, S_{I-}, S_{O+}
Recycling Transfers	+ to 0	Indirect	S_{GI-}, S_{I+}, S_{I-}
	0 to –	Indirect	S_{GI+}, S_{I+}, S_{I-}
	– to 0	Indirect	S_{GI+}, S_{I+}, S_{I-}
	0 to +	Indirect	S_{GI-}, S_{I+}, S_{I-}

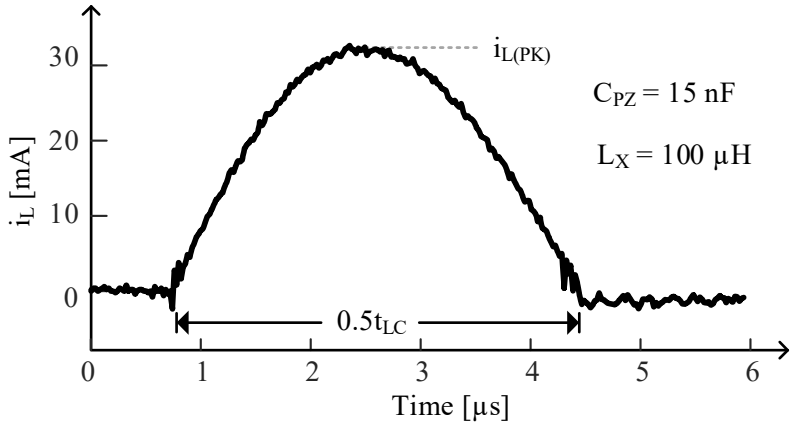

Figure 5-26. Measured i_L for recycling transfers.

5.3.1.B. Recycling Transfers

The charger senses when the half cycle ends, and recycles the charge from C_{PZ} back to C_{PZ} in the opposite direction. To do that, S_{I+} and S_{I-} are closed for the half LC oscillation cycle to first drain the capacitor into L_X, then charge C_{PZ} in the negative direction, as Fig. 5-26 shows. Note that by connecting the bottom plate of C_{PZ} to ground during the first quarter cycle via S_{GI-} and the top plate to ground during the second quarter cycle via S_{GI+}, there is still only positive voltage in the whole system, so that there is no need for a negative supply. Again, the switching configuration is listed in Table 5-2.

5.3.2. Features

The drawn power is calculated by taking the integral of the instantaneous power over a vibration cycle divided by the period:

$$P_{PZ} = \frac{\int_0^{T_{VIB}} v_{PZ} i_{PZ} dt}{T_{VIB}}. \tag{97}$$

Because the operation is completely symmetrical, it is equivalent to taking the integral over a half cycle, and multiply by twice the vibration frequency

$$\begin{aligned} P_{PZ} = \frac{\int_0^{0.5T_{VIB}} v_{PZ} i_{PZ} dt}{T_{VIB}} &\approx v_{PZ(AVG)}(2f_{VIB}) \int_0^{0.5T_{VIB}} i_{PZ} dt \\ &\approx \left(v_{PZ(PK)} - 0.5\Delta v_{PZ}\right)(2f_{VIB})\left(C_{PZ}\Delta v_{PZ(OC)}\right). \end{aligned} \tag{98}$$

From (98), the drawn power is $2C_{PZ}V_{BD}\Delta v_{PZ(OC)}f_{VIB}$, which is the highest possible drawn power, when the voltage drop for each battery charging transfer is negligibly small. The drawn power drops with higher Δv_{PZ}, as shown by the gray trace in Fig. 5-27. Even though keeping Δv_{PZ} as small as possible is enticing, there are also limits that associate with a small Δv_{PZ}, which will be discussed in detail in the next sub-section.

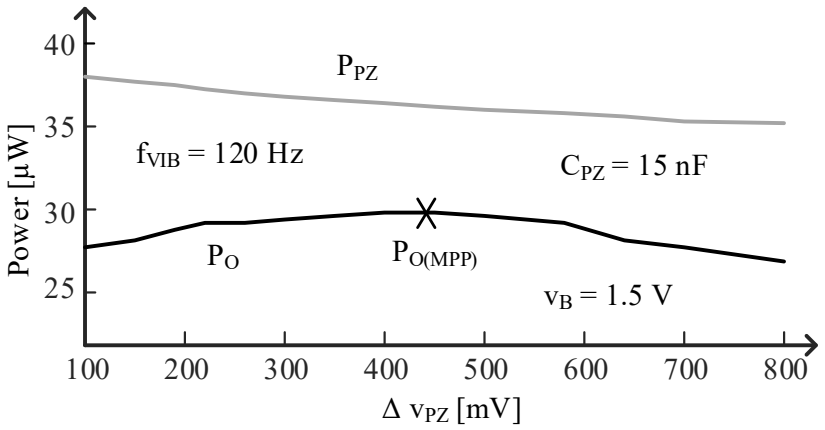

Figure 5-27. Measured power across Δv_{PZ}.

5.3.3. Limitations

Unfortunately the transfers are not ideal, and a portion of the drawn power is lost. The main source of the power loss is from the equivalent series resistance (ESR) through the inductor current path, and the charge loss to switch the power switches on and off. Other losses include overlap loss, shoot-through loss, leakage, and quiescent power to control the circuits.

The circuits, mainly the tiny inductor, transducer, and CMOS switches, are resistive. In a miniaturized solution, the devices are small, and the resistance increase with it. For each energy transfer, the inductor current that goes through the inductor, transducer,

and the switches burns ohmic loss along its path. For each transfer, the ohmic loss is the root-mean-square current squared, times the ESR, times the duration of the transfer $i_{L(RMS)}{}^2 R_{ESR} t_X$. Therefore, the total ohmic loss is

$$P_R = \frac{N_B E_{R(B)} + 2E_{R(R)}}{T_{VIB}} \approx \left(N_B i_{L(RMS,B)}{}^2 t_B R_B + 2 i_{L(RMS,R)}{}^2 t_R R_R\right)(f_{VIB}), \tag{99}$$

where N_B is the number of battery transfers in a half cycle, $i_{L(RMS,B)}$ and $i_{L(RMS,R)}$ are the RMS current, R_B and R_R are the series equivalent resistance, and t_B and t_R are the transfer time for the battery transfer and recycling transfer, respectively.

The ohmic loss is proportional to the number of transfers in a vibration cycle. On the other hand, however, the more times we transfer energy to the battery, each transfer is a smaller energy packet, and the inductor current and transfer time are smaller. This is why the black trace P_R rises with Δv_{PZ} in Fig. 5-28. The ohmic loss also rises with transfer time and RMS current of each transfer. This is why using direct transfers can reduce ohmic loss significantly, having both lower transfer current and transfer time than indirect transfers [151]. Lastly, the ohmic loss is proportional to the ESR. The resistance of the switches is inversely proportional to the width of the MOSFET switch.

On the other hand, the MOSFET switches require charge to switch them on and off, and in the process consumes charge loss. Each switch with gate capacitance C_G requires $v_{DD}C_G$ amount of charge for each switching event, and since it's supplied from v_{DD}, each switch consumes

$$E_C = C_G {v_{DD}}^2. \tag{100}$$

Therefore, the total charge loss is

$$P_C = \frac{N_B E_{C(B)} + 2E_{C(R)}}{T_{VIB}} \approx \left(N_B C_{G,B} {v_{DD}}^2 + 2C_{G,R} {v_{DD}}^2\right)(f_{VIB}), \tag{101}$$

where $C_{G,B}$ and $C_{G,R}$ are the total gate capacitance of the battery transfer switches and recycling transfer switches, respectively.

The charge loss from (101) increases with the number of battery transfers in a cycle. Therefore, PC drops with higher Δv_{PZ}, as shown in Fig. 5-28 with the gray trace. The charge loss is proportional to the total gate capacitance of the switches, which rises with wider devices. However, wider devices also result in lower resistance, and consequently lower ohmic loss. Therefore, each switch needs to be optimally designed so that the ohmic loss balance the charge loss, so that the total loss is the lowest.

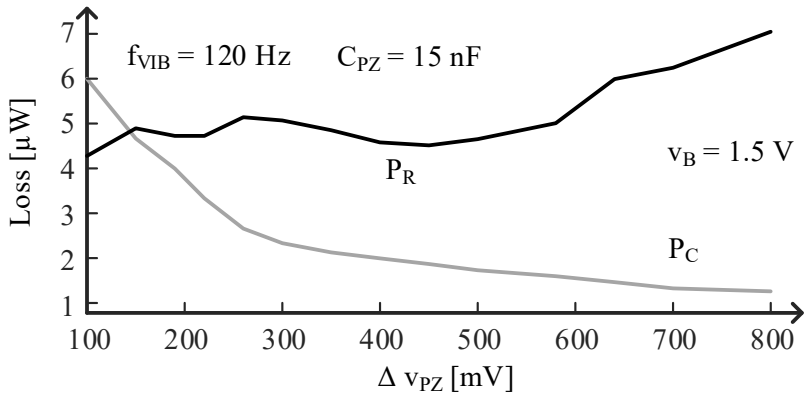

Figure 5-28. Measured power losses across Δv_{PZ}.

5.3.4. Maximum Output Power

The charger charges the battery N_B times every vibration cycle. For each battery transfer, the energy provided from the transducer is the energy difference before and after the transfer.

$$\Delta E_{PZ} = 0.5 C_{PZ} v_{PZ(PK)}{}^2 - 0.5 C_{PZ} \left(v_{PZ(PK)} - \Delta v_{PZ} \right)^2. \quad (102)$$

Because of the losses, the battery does not receive all the power drawn from the transducer. The output power is therefore the difference between input power and loss

$$P_B = \Delta E_{PZ} N_B f_{VIB} - P_R - P_C. \quad (103)$$

Figure 5-29 depicts the output power of the recycling switched-inductor with indirect transfers (solid gray trace) and direct transfers (solid black trace) across the vibration range. The direct scheme outputs more power because of the reduced ohmic loss. Both transfer schemes can withstand vibration voltage up to 10.5 V, 7.2 V higher than the breakdown voltage V_{BD}. When the $\Delta v_{PZ(OC)}$ is higher than 1.2 V, v_{PZ} can be charged to V_{BD} to maintain maximum power-point. Because V_{BD} limits how high v_{PZ} can reach, this region is breakdown limited. However, when the vibration is low, the MPP is achieved with a smaller peak voltage. It can be achieved easily by setting the peak voltage reference for which a battery transfer is triggered. Since the output power is limited by the losses, this region is loss limited. On the low end, the charger can start outputting power with a vibration of only 0.1 V peak to peak voltage on the transducer.

The graph also shows the maximum power a piezoelectric charger can draw with the dotted black trace label “lossless”. The recycling switched-inductor charger can output

about 50% of the maximum power when loss limited, and can reach 88% at the maximum vibration strength.

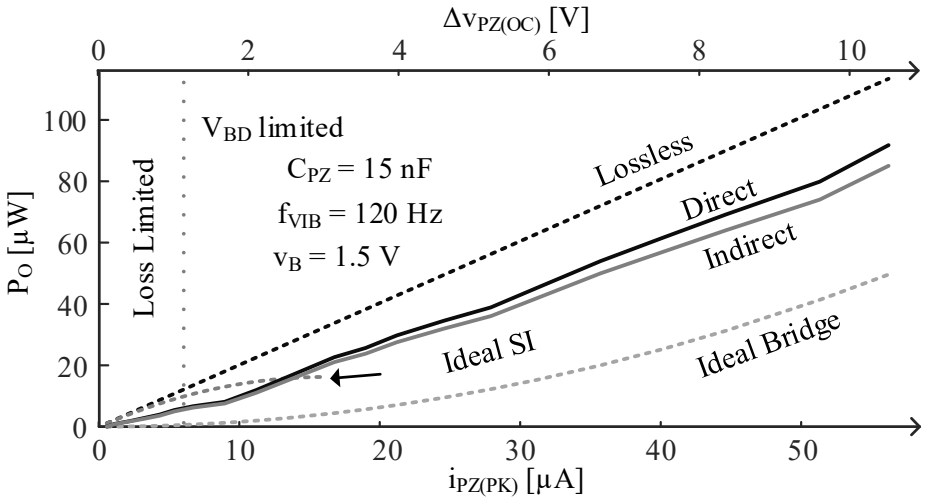

Figure 5-29. Maximum output power with different vibration strength.

The measured piezoelectric voltage is shown in Fig 5-30, and the battery charging capability is shown in Fig. 5-31. A 270 nF capacitor is used in place of the battery, which normally has much larger capacitance to maintain functionality for the wireless microsystems, to highlight the charging profile. The battery charging is intermittent because the recycling transfers are lossy, and it takes some time for the piezoelectric voltage to reach the breakdown voltage again. The piezoelectric voltage flips at 3 ms in Fig. 5-31, and reaches V_{BD} at 5.5 ms to start battery transfers. It shows that with each battery transfer, the battery receives energy throughout the range of 0.5 V to 2.5 V. As a result, the need for an extra maximum power-point charging stage is eliminated.

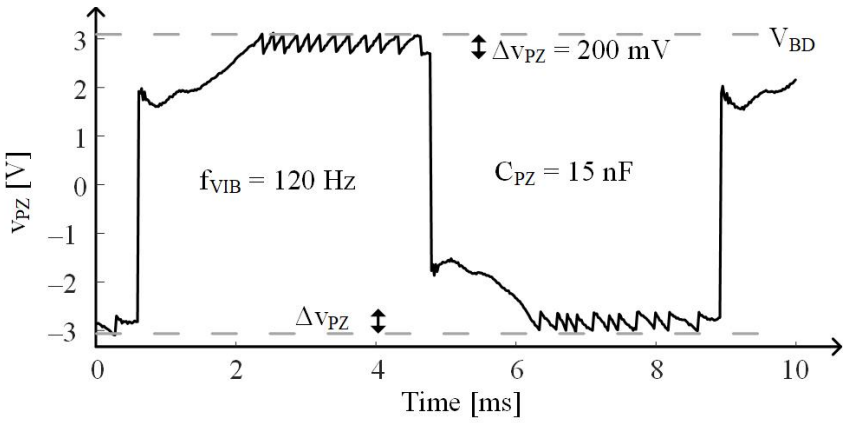

Figure 5-30. Measurement piezoelectric voltage v_{PZ}.

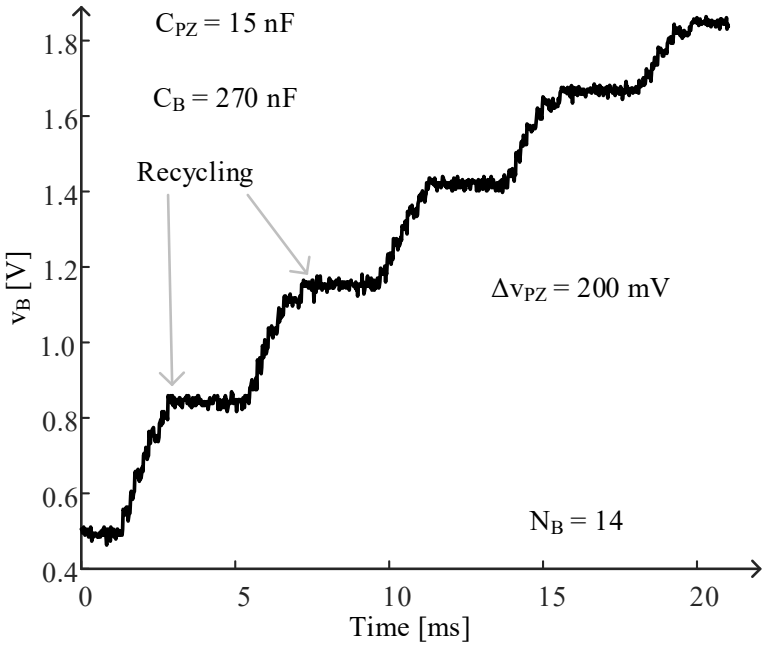

Figure 5-31. Measurement of the battery charging with a 270-nF capacitor.

5.4. **Summary**

This chapter first develop a guidance on how to reduce loss and optimize output power in a CMOS design for a recycling bridge power stage with a maximum power-point switched-inductor (SL) charger with an example piezoelectric device, vibration strength and

frequency, and battery conditions. It is first established that because the on resistance, which is proportional to the ohmic loss, of a MOSFET is inversely proportional to its width, yet the gate capacitance, which is proportional to the charge loss required to switch the MOSFET on and off, is proportional to the width, the optimum width that the total loss on the MOSFET is the lowest when the ohmic loss and the charge loss are equal. For the inductor, when constrained to a certain volume, its inductance rises with its series resistance. With the inductance also influencing the inductor current and transfer time, a set of formula was developed to find the optimum inductance for the recycler and the maximum power-point SL charger. The SL in both continuous conduction mode and discontinuous conduction mode were examined, and it was concluded that discontinuous conduction mode has lower losses with much smaller switching frequency under the provided device and input/output parameters. The optimization strategy can apply to all piezoelectric switched inductor chargers. The design and optimization on the maximum power-point SL can also apply to the more general buck/boost type power stages.

Next two different piezoelectric chargers were proposed, designed, prototyped, and tested. The first charger is a series switched inductor bridge with synchronous discharges, which utilizes symmetrical pre-charging to increase drawn power and lower ohmic loss, and incorporates direct transfers to further reduce ohmic loss. The bridged topology also removes the need for a negative supply, allowing the peak voltage on either direction to reach the breakdown voltage.

The second charger is a switched-inductor bridge with recycling operation. The charger lets the piezoelectric voltage reach the breakdown voltage, then draws a small portion of the charge to charge the battery, and then let the piezoelectric transducer charge

it up again. Between half cycles, the recycler collects all the charger, and puts it in the opposite direction back to the piezoelectric capacitor. The proposed operation can ideally draw the maximum power from the transducer, and uses one fewer inductor than the state of the art recycling bridge. It differs from the recycling bridge in that it charges the battery with the inductor, not with the diode bridge. This way, maximum power-point can be maintained across the battery's voltage range, removing the need for an extra maximum power-point stage.

CHAPTER 6. CONCLUSIONS AND FUTURE WORK

Wireless microsystems for internet-of-things, smart homes, industry, medical implants, and other applications are fast approaching our daily lives. In order to reduce cost, prolong their lifetime, and expand functionality, the microsystems turn to ambient energy from their surrounding environment for assistance. Fortunately, piezoelectric transducer is a good candidate to produce moderate power in an integrated system. From the almost omnipresent vibration, the piezoelectric transducer can constantly replenish the tiny on-board battery, serving as a virtually infinite energy tank.

However, the miniaturized piezoelectric transducer can only convert a small portion of the energy from the vibration to the electric domain. With the low coupling factor, the power level barely matches the average power level of the microsystem. Therefore, the charger needs to extract the maximum energy from the transducer to the battery whenever the vibration is available. The charger would therefore require a maximum power-point function, which maximizes the drawn power and minimizes losses. The charger would also need to function across different magnitude of the vibration strengths to extend its operating range and to protect the system. This research focuses on drawing the maximum power from the piezoelectric transducer, reducing losses during the energy transfer, and with the least constraint on the system to power wireless microsystems. This chapter lists and summarizes the contribution of this research, compares the proposed chargers against the state of the art, and explains the limitation of the technology and possible future research directions for tiny piezoelectric chargers.

6.1. **Contributions**

6.1.1. Piezoelectric Study

The first main contribution of this research is to list, summarize, categorize, compare, and assess the state of the art in piezoelectric chargers. The published chargers were categorized into three groups: basic bridge based, synchronous discharges, and recycling. The summary of the piezoelectric study is listed in Table 6-1. The bridge based charger can draw and output power autonomously, but they draw little power because they cannot collect all the charge, and they require an extra maximum power-point charger to maximize output power. The synchronous discharges increase drawn power by collecting all charge, and pre-charging can further increase drawn power, but inductors are bulky, and it requires a controller to sense the half cycles and control the switches to maintain maximum power-point. Nevertheless, the output power increase is significant enough that these sacrifices are well worth it. Recycling bridge, on the other hand, can draw the maximum power possible from the transducer, but it requires an extra maximum power-point tracker to maintain high output power. The output power would drop significantly without the maximum power-point tracker.

One journal article has been published based on the state of the art, and the conclusions set the research path for the rest of the program.

[J1] G.A. Rincón-Mora and S. Yang, "Tiny piezoelectric harvesters: Principles, constraints, and power conversion," *IEEE Transactions on Circuits and Systems I: Regular Papers*, vol. 63, no. 5, pp. 639–649, May 2016.

Table 6-1. Summary of the piezoelectric study.

	Basic Bridges		Synchronous Discharges		Recycling
	Full	**Half**	**No Pre-Charge**	**Pre-Charge**	
Collected Charge	0.5	0.25	All	All	All
Energy/Cycle	$0.25C_{PZ}\Delta v_{PZ(OC)}^2$		$C_{PZ}\Delta v_{PZ(OC)}^2 + 2C_{PZ}\Delta v_{PZ(OC)}v_{PC}$		$2C_{PZ}\Delta v_{PZ(OC)}v_{BD}$
Damping	Sym.	Asym.	Sym.	Sym./Asym.	Sym.
Pre-Damping	–	–	–	$\pm v_{PD}$	$\pm v_{REC}$
Switches	4+	2+	6	4	8
Inductors	1	1	1	1	2
C_{REC}	1	1	–	–	1
Control	Charger	Charger	Sync.	Sync.	Sync. + Charger

6.1.2. Optimal Pre-Charging

From the conclusions of the state of the art, this research first focuses on improving the synchronous discharges chargers. The existing state of the art uses asymmetrical pre-charging, which requires a negative supply, and the peak-to-peak voltage of the transducer has to be below the breakdown voltage. This research compares the symmetrical pre-charging against the asymmetrical pre-charging, and concludes that both can draw the same power under the same peak-to-peak voltage, but if the symmetrical can draw more power

if only the peak voltage in either direction is the breakdown limit. On the other hand, symmetrical pre-charging recycles some of the energy at the end of the half cycles to pre-charge before the next half cycle, while asymmetrical pre-charging needs assist from the battery. The ohmic loss on the battery transfers for the asymmetrical pre-charging far surpasses that for the symmetrical pre-charging. As shown in Fig. 6-1, under the same peak to peak voltage $v_{PZ(PP)}$, both symmetrical and asymmetrical pre-charging can draw the same power, but ohmic loss reduces the output power, and maximum power point, for asymmetrical pre-charging. Therefore, symmetrical pre-charging should be favoured, due to higher drawn power under the same peak voltage constraint, and lower ohmic losses.

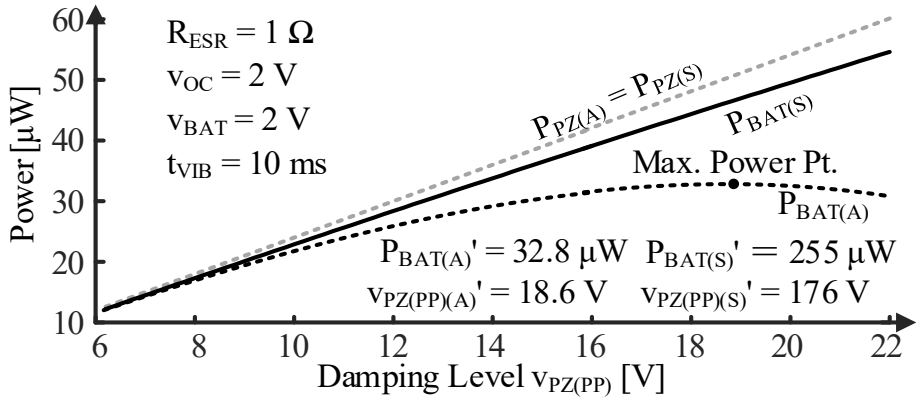

Figure 6-1. Drawn power and output power for symmetrical and asymmetrical pre-charging.

For this contribution, one conference paper has been published to theorize the drawn power and ohmic loss of the symmetrical pre-charging and asymmetrical pre-charging, and one journal article has been published to verify the theories.

[C1] S. Yang and G.A. Rincón-Mora, "Optimally pre-damped switched-inductor piezoelectric energy-harvesting charger," *in Proceedings of 2016 14th IEEE International New Circuits and Systems Conference (NEWCAS)*, Vancouver, BC, 2016, pp. 1-4

6.1.3. Optimal Energy Transfers

This research also closely examines the inductor transfers, and finds out that direct transfers are preferable to indirect transfers. The direct transfers contain a portion of the transfer where the piezoelectric capacitance, the transferring inductor, and the battery are all connected in series. This way, the input capacitor can transfer part of the energy directly into the battery, and the inductor does not have to carry the total energy. Both the transfer time and, more importantly, the root-mean-square inductor current are lower compared to indirect transfers, and the difference is quantified across the battery range. Meanwhile, using direct transfers to pre-charge has also been explored and tested, and it was concluded that using direct transfers with symmetrical pre-charging is the best.

For this contribution, one conference article has been published to introduce direct transfers and theoretically prove that direct transfers consume lower ohmic loss than indirect transfers, and one journal article that experimentally verified the theory, because direct transfers have lower inductor current and, as a result, lower ohmic loss. The journal article also verified the theory on optimal pre-charging, and concludes that the best synchronous discharge charger is the symmetrical pre-charge with direct transfers. Table 6-2 summarizes the comparisons.

[C2] S. Yang and G.A. Rincón-Mora, "Least lossy piezoelectric energy-harvesting charger," *in Proceedings of 2019 IEEE 62nd International Midwest Symposium on Circuits and Systems (MWSCAS)*, Dallas, TX, USA, 2019, pp. 275-278.

[J2] S. Yang and G.A. Rincón-Mora, "Highest power-producing piezoelectric transfers in energy-harvesting switched-inductor chargers," submitted to *IEEE Transactions on Circuits and Systems I: Regular Papers*, 2020.

Table 6-2. Relative performance comparison for damping symmetry and transfer modes.

	JSSC [140]	**TPE [133]**	**JSSC [138]**	**This Work**			
Mode	Asym. PC Ind.	Sym. PC Dir.	Sym. PC Ind.	Asym. PC Ind.	Sym. PC Ind.	Asym PC Dir.	Sym. PC Dir.
C_{PZ}	15 nF	17 nF	20 nF	15 nF	15 nF	15 nF	15 nF
f_{VIB}	143 Hz	120 Hz	140 Hz	100 Hz	100 Hz	100 Hz	100 Hz
$i_{PZ(PK)}$	8.2–36 µA	3.0–33 µA	11 µA	2.3 – 14 µA	1.8 – 14 µA	1.4 – 14 µA	0.9 – 14 µA
$\Delta V_{PZ(OC)}$	1.2–5.2 V	0.5–5.5 V	1.2	0.5–3.0 V	0.4–3.0 V	0.3–3.0 V	0.2–3.0 V
V_{BD}	15 V	5.5 V	> 7.0 V	3.0 V	3.0 V	3.0 V	3.0 V
L_X	330 µH	330 µH	340 µH	100 µH	100 µH	100 µH	100 µH
P_O	2.1–53 µW	0.7–49 µW	15 µW	0 – 7.9 µW	0 – 7.9 µW	0 – 9.1 µW	0 – 9.1 µW
η_O	2.6×– 3.5×	3.2×– 6.8×	14×	2.8× – 6.6×	2.8× – 7.2×	3.3× – 10.5×	3.3× – 15.5×

6.1.4. Optimal Design

The research then provides a guideline on how to design an optimal piezoelectric charger. The summary of the optimization sequence and concept is listed in Table 6-3. Because ohmic loss decreases with the width of the MOSFET switch, but the charge loss increase with it, the MOSFET loses the least combine power when the ohmic loss and the charge

loss balance. The inductor also has a trade-off: with larger inductance to reduce peak inductor current, the transfer time and series resistance both increase. With this information, the switched inductor loss can be fully calculated, and an optimum inductor can be selected. The optimization scheme should be used in both continuous conduction mode and discontinuous conduction mode, and the superior one should be used.

Table 6-3. Summary of the optimal design.

	Optimize Power Switch	**Optimize Recycler**	**Optimize SL Charger**	
			CCM	**DCM**
1	Lowest L for low R_{ON}, C_G	P_{LX} rises with L_X	$P_O \propto P_{PZ} - P_X - P_B - P_{SL}$	
2	$P_R \propto \frac{1}{W}$	P_{SX} falls with L_X with optimized switches	Calculate $P_{R(LO)}$	
3	$P_C \propto W$	Choose L_X so that $P_{LX} + P_{SX}$ is lowest	Calculate $P_{SE/D}$	
4	Choose W so that $P_R = P_C$		Plot $P_{RLO} + \Sigma P_{SE/D}$ to find lowest loss	For L_O, choose corresponding f_O, $i_{LO(PK)}$ for lowest loss
5			Choose the lower loss	

For this contribution, one conference article has been published to detail the optimization.

[C3] S. Yang and G.A. Rincón -Mora, "Piezoelectric CMOS Charger: Highest Output Power Design," *in Proceedings of IEEE International Symposium on Quality Electronic Design (ISQED)*, Santa Clara, CA, 2020.

6.1.5. Series Switched-Inductor Charger

Using the aforementioned design guidelines, and to increase drawn power, reduce loss, and relax limits on the system, the research proposed, designed, fabricated, tested, and assessed two piezoelectric chargers. The first charger utilizes direct transfers and symmetrical pre-charge with series switched-inductor bridge power stage. The 3.3–33 μA (i_{PZ}) that the shaker here induces at 120 Hz (f_{VIB}) charges a 16.8-nF piezoelectric capacitance C_{PZ} across 0.5–5.5 V ($\Delta v_{PZ(OC)}$). With this stimulation, the lossless diode bridge can draw 0.13–15 μW, like $P_{PZ(BRDG)}$' in Fig. 6-2 shows. The prototyped series switched-inductor bridge, however, draws 1.2–55 μW (P_{PZ}) and delivers 0.70–49 μW ($P_{O(MPP)}$). Overall, like Fig. 6-2 demonstrates, the prototype draws 3.7×–9.8× ($\eta_{I(PZ)}$) and outputs 3.3×–6.8× ($\eta_{I(O)}$) more power than the lossless bridge can and outputs 45%–91% (η_C) of the power drawn.

Piezoelectric power P_{PZ} overcomes losses when vibrations charge C_{PZ} more than 0.5 V. This 0.5-V threshold level corresponds to the minimum vibration strength from which the system can harvest power. Power indices $\eta_{I(PZ)}$ and $\eta_{I(O)}$ are high at 5.9–9.8 and 4.5–6.8 when vibrations charge C_{PZ} 0.5–3.5 V. Harvesting performance is lower when vibrations are stronger because the transistors' 5.5-V breakdown voltage V_{BD} limits the voltage v_{PZ} with which i_{PZ} draws P_{PZ}.

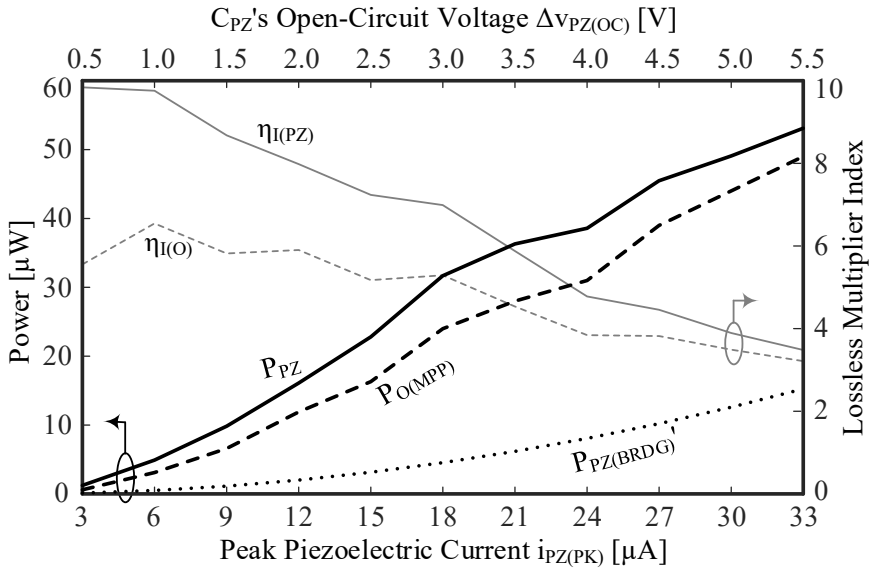

Figure 6-2. Measured power and lossless diode-bridge index.

Power-conversion efficiency η_C is not as important as $\eta_{I(PZ)}$ and $\eta_{I(O)}$ because η_C does not account for how much power the harvester can draw. η_C is still a good measure of quality, however, because systems output more power when optimally designed to balance losses. In this case, η_C is 75%–91% when vibrations charge C_{PZ} more than 3 V. η_C falls to 45% below 1 V because gate-drive and shoot-through losses P_G and P_{ST}, which do not scale down with P_{PZ}, dominate when P_{PZ} is low. In other words, the system is more optimal for higher P_{PZ}.The relative performance of the series switched-inductor charger compared with the state of the art is shown in Table 6-4. One journal article has been published to report the proposed power stage, introduce the design and operation, and compare with the state of the art.

[J3] S. Yang and G.A. Rincón-Mora, "Energy harvesting piezoelectric-powered CMOS switched-inductor bridge," *IEEE Transactions on Power Electronics*, vol. 34, no. 7, pp. 6489–6497, July 2019.

Table 6-4. Relative performance of the state of the art and the two proposed chargers

	JSSC [144]	JSSC [140]	TCAS-I [132]	JSSC [145]	JSSC [146]	This Work	
Power Stage	Diode Bridge	SL Half Bridge	Recycling Bridge			SL Bridge	Recycling SL
L_{MIN}	1 µm	0.18 µm	250 nm	350 nm	130 nm	0.82–1.2 µm	0.3–0.35 µm
V_{BD}		15 V		5 V		5.5 V	3.3 V
Si. Area	4.25 mm^2	2.3 mm^2	0.75 mm^2	0.54 mm^2	0.53 mm^2	0.25 mm^2	0.26 mm^2
L_X		330 µH	220 µH	3400 µH	47 µH	330 µH	100 µH
R_L		1.6 Ω		8.1 Ω		1.6 Ω	0.6 Ω
C_{PZ}	12 nF	15 nF	19 nF	9.6 nF	14 nF	17 nF	15 nF
f_{VIB}	225 Hz	143 Hz	144 Hz	230 Hz	441 Hz	120 Hz	120 Hz
$\Delta V_{PZ(OC)}$	4.8 V	1.2–5.2 V	9.8 V	≥ 1.34 V	3 – 4 V	0.50–5.5 V	0.15– 10.5 V
P_{IDEAL}	15.6 µW	0.80–15.1 µW	65.7 µW	≥0.99 µW		0.13–15 µW	0.008 – 41 µW
P_{PZ}	8.2 µW	7–78 µW				1.2–55 µW	0.2 – 100 µW
$P_{O(MPP)}$	7.5 µW	2.1–52.5 µW	136 µW	5–410 µW	40.6 µW	0.70–49 µW	0.1 – 91 µW
P_Q		0.5 µW	1.5 µW			Off Chip	Off Chip
$\eta_{O(MPP)}$	48 %	2.6×–3.5×	2.1×	3.1×–6.8×	4.48×	3.2×–6.8×	2.0 – 12×
$\eta_{O(BD)}$		Up to 3.3%		Up to 63%		Up to 14%	Up to 76%
Components	4 FETs, Buffer	L_X, 2 FETs	L_X, 4 FETs, Buffer	L_X, 6 FETs, Buffer	L_X, 10 FETs Buffer	L_X, 4 FETs	L_X,10 FETs

6.1.6. Recycling Switched-Inductor Charger

The second charger uses a newly proposed recycling switched-inductor that utilizes recycling operation, which can draw the highest possible power, and the switched inductor

charges the battery while maintaining the maximum power-point across the battery's operating range, negating the necessity of another maximum point-point charger stage. The second charger is also used to validate the theory that symmetrical pre-charging draws more and loses less power than asymmetrical pre-charge, and that direct transfers outperforms indirect transfers by allowing the inductor to transfer more power than it carries, saving ohmic loss.

The proposed recycling switched-inductor charger enjoys the benefit of the recycling bridge in that the piezoelectric voltage is also near the breakdown voltage across the half cycle. However, it does not require a second stage to achieve maximum power-point, since it can charge the battery directly across its range. Therefore, it can draw up to 85 μW from 10.5 V open circuit voltage from a 120 Hz vibration on a 15-nF piezoelectric capacitance. With direct transfers to further reduce the ohmic losses, the output power can be up to 91 μW, and the output power index can reach 12×.

Another significant improvement of the proposed power stage is when the vibration is very low. The charger starts outputting power when the vibration only generates 0.1 V peak to peak voltage on the capacitance. That is because without the use of a rectifying capacitor, the piezoelectric voltage can easily change from cycle to cycle, therefore maintaining maximum power point. With a wider input range, the charger can consistently output more energy to the battery.

The relative performance of the series switched-inductor charger compared with the state of the art is shown in Table 6-4. One journal article has been submitted to report

the proposed power stage, introduce the design and operation, and compare with the state of the art.

[J4] S. Yang and G.A. Rincón-Mora, “Piezoelectric-powered recycling switched-inductor maximum power-point charger,” submitted to *IEEE Transactions on Power Electronics*, 2020.

6.2. **The State of the Art**

6.2.1. Power Indices

Maximum output power $P_{O(MPP)}$ hinges on vibration frequency and strength, the transducer, the transducer's damping voltage, and losses. Of these, the only design-independent, application-specific factors are vibration frequency f_{VIB} and strength (in the form of acceleration in the mechanical domain and current i_{PZ} in the electrical domain). The transducer and the circuit that transfers power are typically the design variables that engineers control. Unfortunately, research splits along these lines, so advancements in circuits normally appear in the absence of advancements in transducers, and *vice versa*. As a result, literature rarely reports the best all-around solution.

Here and in the case of [132] – [150], the research focus is on how the circuit performs at steady-state, not the transducer. So comparing performance without normalizing the effects of the transducers used is unfair. The components in the transducer that in part determine $P_{O(MPP)}$ are capacitance C_{PZ}, resistance R_{PZ}, and dynamic capacitance $C_{PZ(XFR)}$. But since the diode bridges in draw power across half cycles (not between half cycles), the dynamic effects of $C_{PZ(XFR)}$ are absent. So including $C_{PZ(XFR)}$'s losses P_{CPZ} in

the comparison is fair. How R_{PZ} affects $P_{O(MPP)}$ also depends on the harvester, so although R_{PZ} is, like $C_{PZ(XFR)}$, an imperfection in the transducer, a fair evaluation should similarly account for R_{PZ}'s loss P_{RPZ}.

The steady-state power $P_{PZ(BRDG)}'$ that a lossless diode bridge draws from i_{PZ} and C_{PZ} at f_{VIB} [139] includes all the independent components that research in circuits assumes (like i_{PZ}, C_{PZ}, and f_{VIB}) and excludes all the variables that circuit designers control and assign:

$$P_{PZ(BRDG)}' = 0.25 C_{PZ} \Delta v_{PZ(OC)}^{2} f_{VIB}. \tag{104}$$

Like before, $\Delta v_{PZ(OC)}$ is the voltage that i_{PZ} charges C_{PZ} across every half cycle. So comparing input and output power to this lossless case is a good way of assessing and normalizing circuit performance to the transducers used.

Drawn power index $\eta_{I(PZ)}$, for example, indicates how much more power a harvester draws (with P_{PZ}) than a lossless diode bridge can harness from the same piezoelectric transducer:

$$\eta_{I(PZ)} = \frac{P_{PZ}}{P_{PZ(BRDG)}'}. \tag{105}$$

Losses P_{LOSS} limit how much of P_{PZ} the system delivers with $P_{O(MPP)}$. So with respect to the output, power-conversion efficiency η_C reduces $\eta_{I(PZ)}$ to yield output power index $\eta_{I(O)}$:

$$\eta_{I(O)} = \eta_{I(PZ)} \eta_C = \left(\frac{P_{PZ}}{P_{PZ(BRDG)}'} \right) \left(\frac{P_{O(MPP)}}{P_{PZ}} \right) = \frac{P_{O(MPP)}}{P_{PZ(BRDG)}'}. \tag{106}$$

which compares $P_{O(MPP)}$ with $P_{PZ(BRDG)}$'. But since gains in P_{PZ} can outpace P_{LOSS}, $\eta_{I(O)}$ is a better metric than either $\eta_{I(PZ)}$ or η_C alone. Still, $\eta_{I(PZ)}$ indicates the ability of a system to draw piezoelectric power P_{PZ} and η_C the efficacy with which a system transfers this power.

Another ideal power stage, the ideal recycling charger, can produce another normalized power index, especially if breakdown voltage limits the output power of a charger. The maximum power a lossless recycling charger is $2C_{PZ}V_{BD}\Delta v_{PZ(OC)}f_{VIB}$ from (98) in Chapter 5. The percentage of that ideal power that the charger can output to the battery is

$$\eta_{O(BD)} = \frac{P_{O(MPP)}}{2C_{PZ}V_{BD}\Delta v_{PZ(OC)}f_{VIB}}. \tag{104}$$

This normalizes the transducer, vibration, and the breakdown voltage, can be used to compare recycling chargers.

6.2.2. Relative Performance

The reported state of the art and the performance of the two proposed prototypes have been categorized and summarized in Table 6-4. Because P_{IDEAL} is the maximum drawn power for the ideal diode bridges and half bridges, real diode bridges and half bridges can draw less than P_{IDEAL}. Despite not requiring controllers to sense the half cycles, the bridge based power stages needs MPP chargers to keep them at maximum power-point. Adding to the ohmic loss and charge loss, the output power index for the basic bridge is well under 1.

The switched-inductor power stage improve upon the basic bridges by collecting all the charge created by the vibration. It can draw as much as four times higher power than

the ideal bridge can draw. It can be further improved by pre-charging the transducer before every half cycle, increasing the voltage the charge is created at. With the higher drawn power, even though the charger now consumes more ohmic and charge loss, the output power index can be as high as 6.8×.

The recycling bridges can draw the highest power, because the piezoelectric voltage is always the highest at near the breakdown voltage V_{BD}. However, it requires a MPP charger to regulate the rectifying voltage around the breakdown voltage, and the most efficient way to accomplish that is to use another switched-inductor power stage. A two-inductor solution is not ideal for the microsystem application, and because of the added losses, the output power index is still only about 6.8.

The proposed recycling switched-inductor has by far the highest output power index at 12×. Although the index drops to only 2.0× at higher vibration strength, that is fundamentally limited by the breakdown voltage. In fact, the highest possible drawn power index when the $\Delta v_{PZ(OC)}$ is 10.5 V with a 3.3 V breakdown is 2.6×, and the proposed charger is outputting 76% of that. It actually shows one of the strength of the recycling switched-inductor charger, in that it extends the operating range much beyond the breakdown limit of the system. On the other end of the vibration strength is where this topology outperforms its competitors. Because of the direct transfers and with symmetrical damping, the charger is optimized to output the highest power across the vibration strength, and across the battery voltage. It can draw from by far the lowest vibration strength, significantly increasing the feasibility of power a wireless microsystem with ambient vibrations or shocks.

6.3. **Future Work**

Although the proposed charger outperforms the state of the art, there is still a lot that it can improve on. This section lists some of the limitation of the prototype, and any future research on this topic can look to improve upon it.

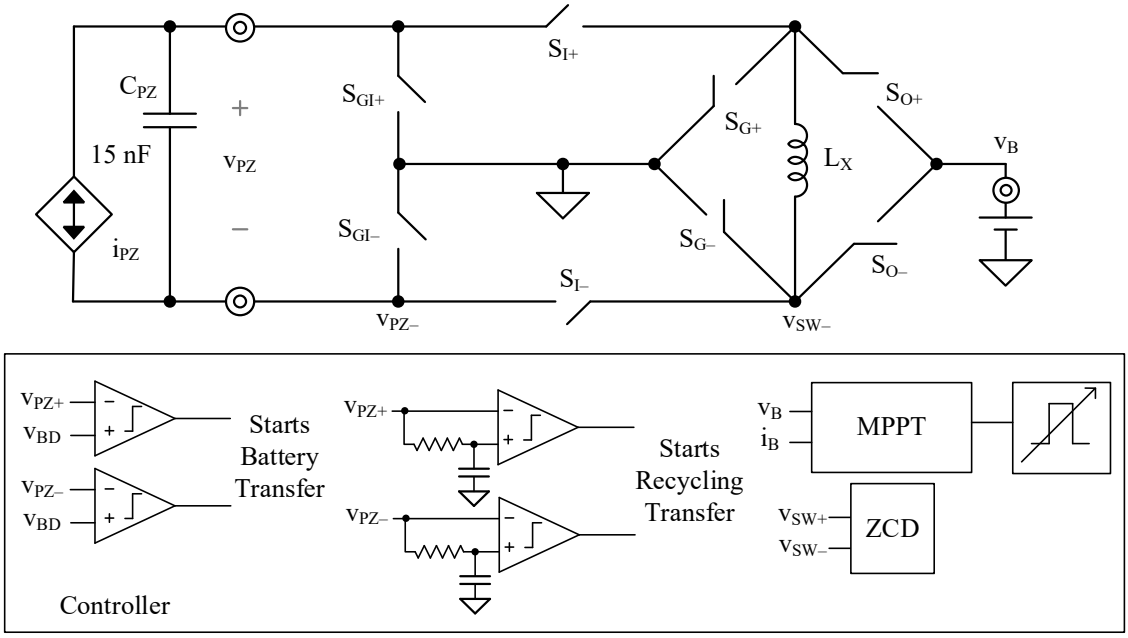

Figure 6-3. MPPT controller for recycling switched-inductor charger

6.3.1. Integrated Maximum Power-Point Controller

Although the power stage of the proposed charger outperforms the state of the art, the charger itself is not yet complete. What is missing is a closed-loop maximum power-point controller, which senses the half cycles, piezoelectric voltage, the battery voltage, and controls the switches to maintain maximum power-point. Currently the analog to digital converter on the FPGA controller senses the half cycles and the piezoelectric voltage, while the energizing time and drain time are adjusted in 20 ns increments until the maximum

power point and zero current switching is achieved. The integrated controller would need to accomplish all the functionality the FPGA has to be used in a piezoelectric powered wireless microsystem.

In an integrated closed-loop system, an on-chip comparator can be used to sense when the piezoelectric voltage is at the breakdown voltage to start a battery transfer, as Fig. 6-3 shows. Another comparators, whose inputs are the piezoelectric voltage and a delayed version of that, can sense the half cycles [140]. The maximum power point controller sets the energizing time for the battery transfer, and a zero current detection block controls the end of the drain time. Maximum power-point can be achieved mainly in two ways: a perturb and observe algorithm [152], otherwise known as hill-climbing algorithm, or a look-up table [153]. The perturb and observe method finds maximum power-point by changing one variable, in this case the energizing time in a battery transfer, and observe the change in output power. If the output increases, the variable is changed in the same direction for the next cycle; if the output decreases, the variable is changed in the opposite direction for the next cycle. Because the vibration strength changes slowly across cycle, the algorithm does not need to activate every cycle, in order to reduce quiescent power. The look-up table, on the other hand, stores the optimum value for a variable based on the conditions of the charger into a table. When the conditions changes, the controlling variable is also changed according to the look-up table. Both method should be able to be implemented with the recycling switched inductor charger, but more research is needed to verify and assess which one is better. A fixed delay that matches a quarter cycle of the LC oscillation can be used to control both the energizing time and the drain time for a recycling

transfer. The zero current detection block can also be used to fine tune the fixed delay to minimize the losses.

6.3.2. Cold Start

Another aspect of the charger that is not yet complete is the capability to start without any energy in the system initially, or cold start [154]. When the vibration is intermittent, there could be cases where the energy source goes away for a long time. Without a large battery on board, the system can deplete all the energy it has stored before the next wave of vibration becomes available. The charger would therefore need to harvest the vibration energy without any energy already in the system to complete cold start.

The controller that turns the switches on and off and tracks maximum power-point cannot work when the battery is depleted. However, diodes can still passively direct current into an energy storing device. As discussed in Chapter 2 and Section 6.2, the maximum drawn power of the diode bridge for a piezoelectric charger is low compared to the switched inductor with pre-charging or recycling chargers. The output power from a diode bridge is even lower if it's not at maximum power-point, and without a controller, it would not be. As a result, it would take a long time for the diodes to charge the battery above the headroom level for the controller to function. An alternative is to charge a small on-chip capacitor with the diode bridge. Because the capacitance is much smaller than the battery, it takes much shorter time to charge the temporary supply above the headroom level. The temporary supply capacitor would then supply the controller and drivers to output higher power to the main battery, while maintaining the headroom voltage on the temporary

supply. Once the main battery's voltage is also above the threshold, the temporary supply can be shorted with the battery, and the charger could then maintain normal operation.

As Fig. 6-4 shows, when the vibration starts at 1 s, the charger first charges the temporary supply with low output power. However, the temporary supply has low capacitance. Therefore, it's still able to reach the head room level, set at 1 V, in under 1 second. Once the voltage on the temporary supply v_{TEMP} reaches 1.1 V, it starts powering the maximum power point block, and output high power to the battery. As vTEMP drops to 1.0 V, the maximum power point charger halts, and the diodes again charges CTEMP to 1.1 V. The sequence it repeated until the battery reaches the headroom level, and then C_{TEMP} and v_{BAT} can be shorted together.

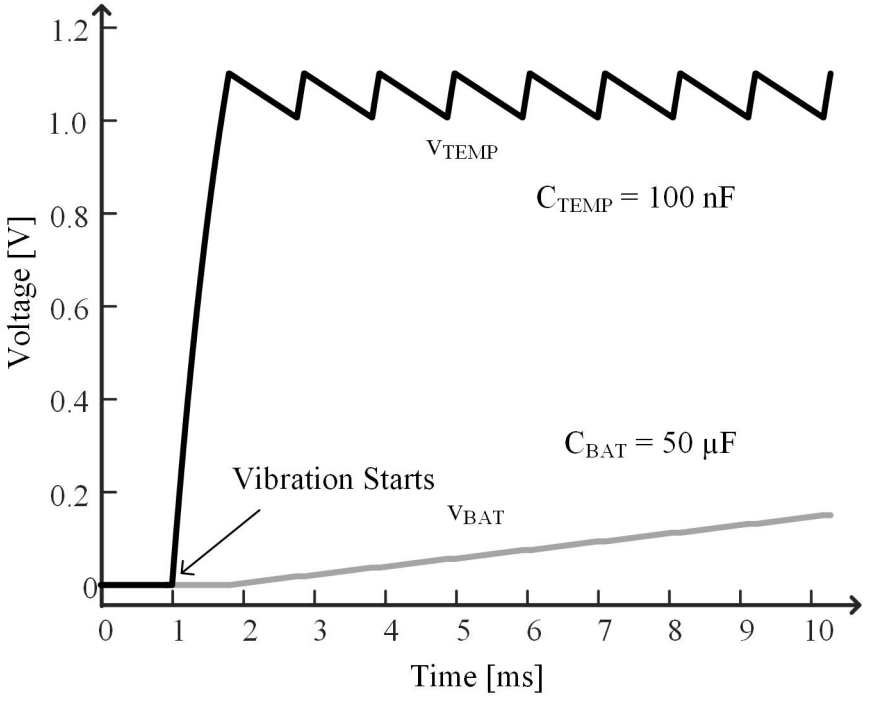

Figure 6-4. Cold start charging of temporary supply and battery.

The size and capacitance of both the main battery and the temporary supply capacitor need to be carefully designed. The main battery is bulky, and would take too much space if its capacitance is too large. However if the capacitance is too small, the energy could deplete more often, and cold start, which is much less efficient, would be used more frequently, which reduces the output power in the long run. The temporary supply capacitor needs to be small so that even the low output power diode bridge can charge it quickly. However, if it is too small, it could drop below the headroom level once it starts to supply the controller. Reference [155] offers a guideline on how to design cold start battery and temporary supplies for photovoltaic and thermal energy generators, and the technique could also be applied here.

6.3.3. Integrated Piezoelectric Energy Harvesting System

The last step to complete the system is to integrate the micro-electro-mechanical system (MEMS) piezoelectric transducer with the charger to create a fully miniaturized charger. The proposed charger, for proof of concept purposes, are tested with off the shelf, centimetre-scale transducers. The wireless microsystems would require MEMS transducers to fit in difficult to access spaces and be non-intrusive to the environment.

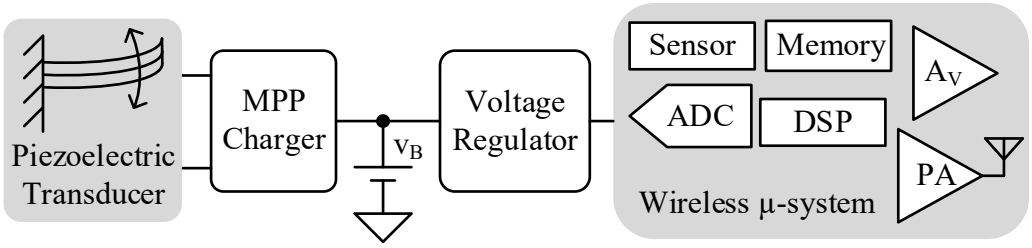

Figure 6-5. Integrated piezoelectric energy harvesting wireless microsystem.

As Fig. 6-5 shows, the complete integrated system includes the piezoelectric transducer, the MPP charger in Fig. 6-3, the battery, the voltage regulator that supplies power to the electronic loads, and the functional blocks for the wireless microsystems. Because building MEMS transducer require deep understandings and knowledge in microsystems design and fabrication, which is different from the power electronics design and analog IC designs required to build the optimum charger, the two researches have always been separate. MEMS transducer differs from the off-the-shelf transducers in capacitance, in capacitance, breakdown voltage, mechanical-electrical coupling coefficient, resonant frequency. However, all the basic concepts developed in this research (pre-charging increases drawn power, symmetrical pre-charging with direct transfers reduce losses, and recycling operation draws the maximum power) can apply to a fully integrated charger with MEMS transducers. This research can therefore be picked up by a future project that has already developed and tested a MEMS transducer, but would need a charger to maximize the power to charge the battery. Alternately, a power electronics engineer could look to build a MEMS device best suited for the current charger, to complete a fully integrated solution for the wireless microsystems.

6.4. **Summary**

6.4.1. Piezoelectric Transducers

A cantilever transducer is used for measurement because of its availability off the shelf and because it's easy to test. The model for other types of piezoelectric transducers, e.g. beam or membrane, are the same as the cantilever, with different resonant frequencies and coupling factor. However, the resonant frequencies still are in the range of 100s of hertz

[70]–[80], with excitation accelerations in the range of several meters per second, and they still have low coupling factor, so the techniques presented in this research to increase drawn power and the maximum power point tracker would be able to accommodate other types of transducers.

6.4.2. Transducer Model

The complete piezoelectric transducer model [156]–[158], shown in Fig. 6-6, includes the mass M_M, the stiffness of the cantilever k_{PZ}, the mechanical damping D_M, and the electrical components, v_{PZ} and i_{PZ}. The voltage v_{PZ} damps the vibration to convert energy into electrical domain. As the mass vibrates under external force F_{EXT}, the mechanical damping and electrical damping collectively oppose the force for the vibration to reach equilibrium:

$$M_M \frac{d^2x}{dt^2} + k_{PZ}x + D_M \frac{dx}{dt} + \alpha v_{PZ} = M_M \gamma. \tag{105}$$

where x is the displacement, α is the mechanical-electrical force factor, and γ is the acceleration under external force.

The equivalent circuit model of the piezoelectric transducer is depicted by Fig. 6-7. According to the maximum power transfer theorem, the maximum power the electrical load can receive from the vibration happens when the electrical damping is the same as the mechanical damping. Therefore, increasing electrical damping v_{PZ} increases drawn power until electrical damping overwhelms mechanical damping. Tiny piezoelectric transducers, however, have low k_C, and electrical damping never reaches the maximum point. The circuit in [140] operates up to 15 V, and the vibration displacement only drops by 4%. The

power stage in [146] tests with open-circuit voltage of 50 V, and the electrical damping has still not reached maximum power point. Since the breakdown voltage limit the proposed series switched-inductor charger to 5.5 V, and the recycling switched-inductor charger to 3.3 V, the electrical damping barely affects the vibration displacement and the current it induces. Therefore, the circuit model of the transducer is simplified to an alternating current source. Moreover, the low breakdown voltage also means that Giga-ohm leakage only consumes nanowatts, and therefore is also negligible to the 1–100 microwatt they output. Therefore, the alternating current source in parallel to its parasitic capacitance, shown in Fig. 1-10, is used as the model for all simulation in Cadence.

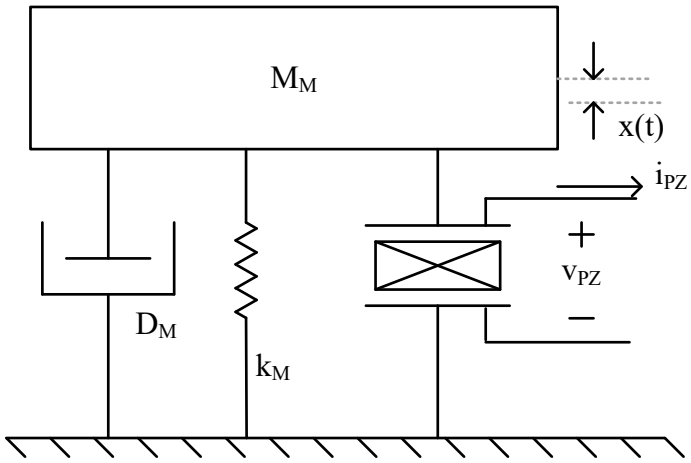

Figure 6-6. Piezoelectric transducer model

The transducer vibration amplitude would be significantly increased if the vibration excitation frequency matches the resonant frequency. However, ambient vibration frequencies can be unpredictable. This is why outputting net power from as low a vibration amplitude as possible is important for a piezoelectric charger. What's more common is when the transducer is under periodic shock excitation from the ambient and the transducer is vibrating at its resonant frequency with decaying amplitude. This is why the maximum

power point tracker loop, which wasn't part of this research, should be fast enough to react to the decaying sinusoidal input. The state of the art [130]–[146] is aware of this, where the same simplifications of the piezoelectric model are made.

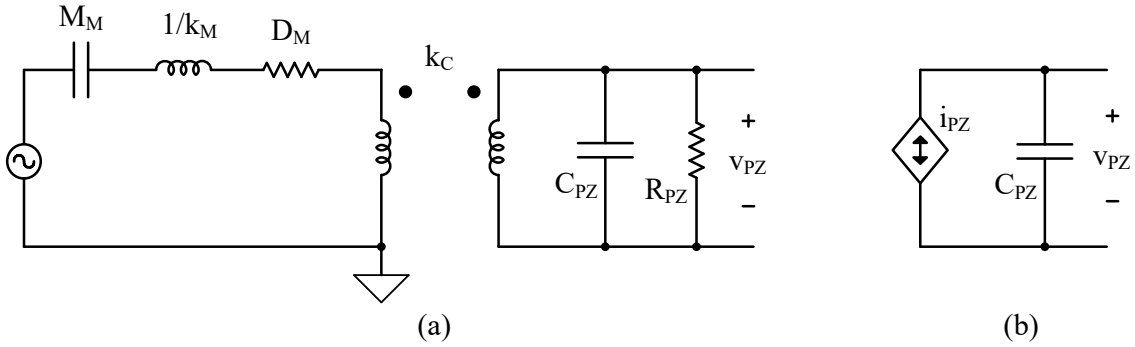

Figure 6-7. Equivalent circuit model for piezoelectric transducers: (a) complete model, and (b) simplified model.

6.4.3. Why Switched-Inductor

The basic bridge and half bridge are the state-of-the-art without the use of inductors. However, both schemes lose part of the charge generated by the vibration to charging C_{PZ} between positive and negative rectifying voltages. As Fig. 6-8 shows, the diode bridge only collects the charge when $|v_{PZ}|$ is at v_{REC}, (2.5 – 5 ms, and 7.5 to 10 ms), and some charge is lost to charge C_{PZ} between the positive and negative rectified voltages. The recycling chargers in the state of the art [142]–[150] can collect all the charge because inductor can use the energy from C_{PZ} to quickly discharge/charge C_{PZ} to the rectified plus/minus targets, as shown in Fig. 6-9. Because the LC oscillation period is within microseconds, while the vibration cycles last milliseconds, the transfer appears instantaneous. Therefore, before each half cycle starts, the piezoelectric voltage is already at the rectified voltage, and the bridge can start steering charge into the C_{REC} immediately, thereby collecting all charge.

Moreover, the charge is collected at the maximum voltage V_{BD} across half cycles, maximizing the power the transducer can output.

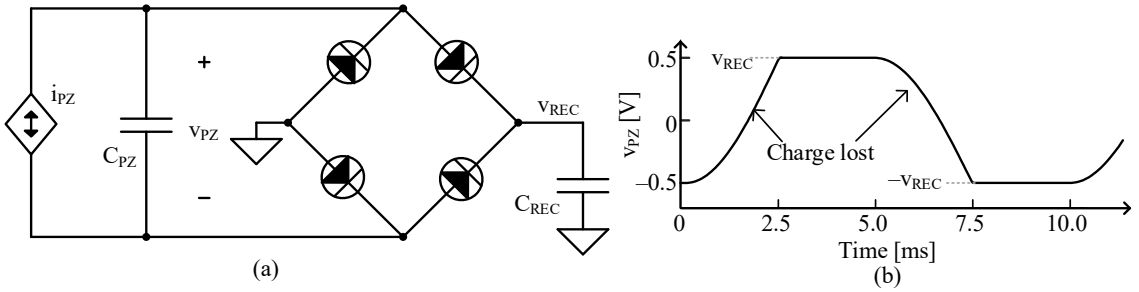

Figure 6-8. The (a) schematic and (b) piezoelectric voltage for diode bridge without an inductor.

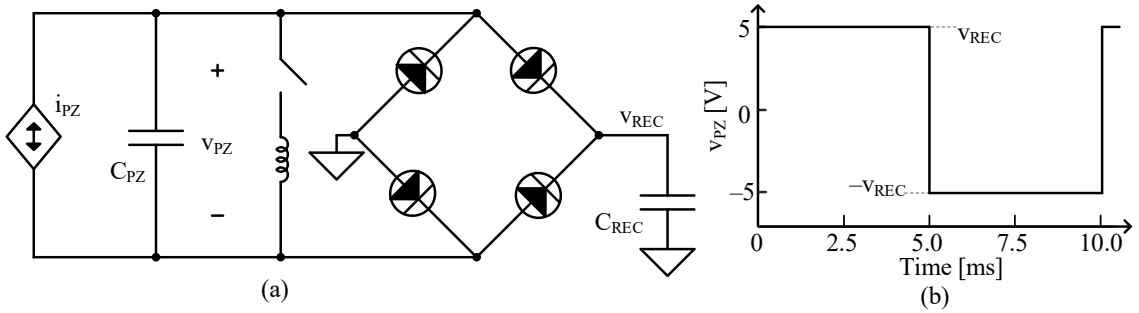

Figure 6-9. The (a) schematic and (b) piezoelectric voltage for recycling bridge with an inductor.

6.4.4. Optimal Symmetry

Both asymmetrical discharges and symmetrical discharges can draw the same power under the same peak-to-peak voltage. However, if the breakdown only limits the peak voltage of the system, symmetrical pre-charge can draw up to 2× power more than the asymmetrical counterpart. Asymmetrical discharges, where one current is higher than the other, and only one current charges the battery shown in Fig. 6-10(a), consume more power than symmetrical discharges, where both currents are equal and charge the battery, but lower

than the highest asymmetrical current shown in Fig. 6-10(b), because ohmic losses in battery transfers scale cubically with current, while the energy transferred scales quadratically. Therefore, the higher the current in one transfer, the more percentage of the energy is lost on the series equivalent resistance. The measurement result using the power stage in Fig. 4-18 shows that at maximum power point, symmetrical pre-charging outputs more power across the input range of the system, and can start output net power from a smaller vibration strength, as Figs. 4-25 and 4-26 show, which is new to the state of the art.

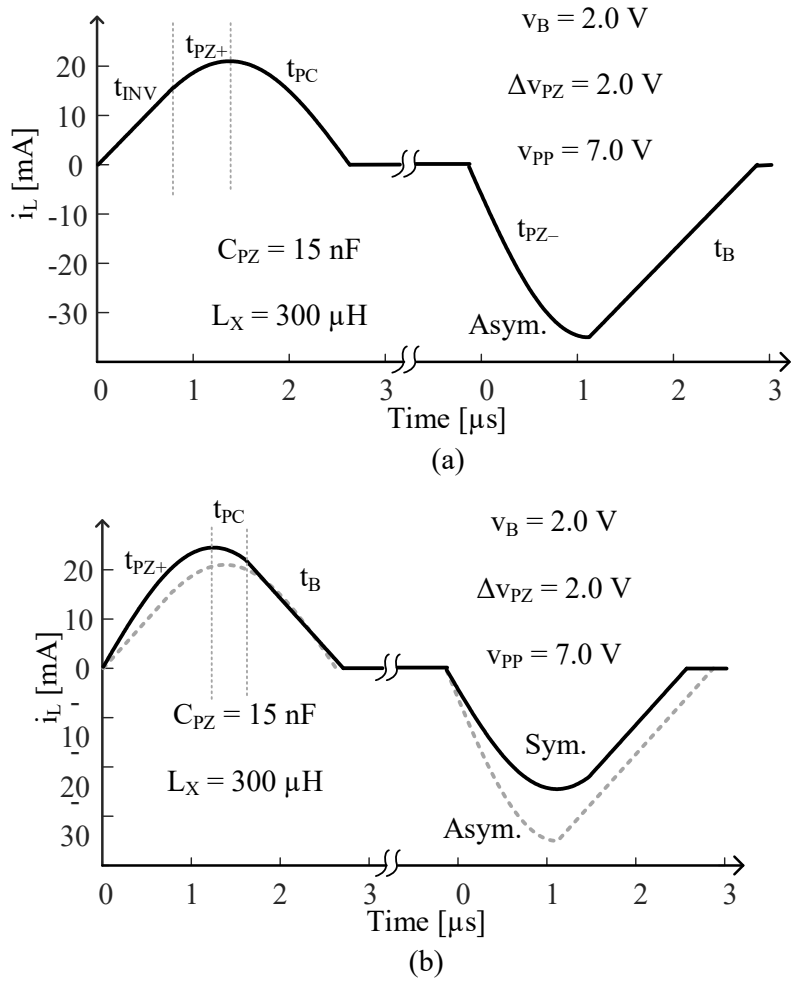

Figure 6-10. Inductor current for (a) asymmetrical pre-charge discharges and (b) symmetrical pre-charge discharges.

6.4.5. Optimal Transfers

Inductors deliver power indirectly when they receive and deliver all the energy the output receives, using Fig. 6-11(a) and (b). Direct transfers allow inductors to transfer more energy than the maximum energy it carries, by letting the inductor energize or drain directly from C_{PZ} to the battery, as Fig. 6-11(c) shows. This way, both inductor current and transfer time are lower, resulting in reduced ohmic loss. The detailed comparisons have been presented in Chapter 4, and the measurement results in Figs. 4-25 and 4-26 validate that direct transfers can output more power than indirect transfers across the input range of the system, and start output net power from a smaller vibration strength, and this is a new to the state of the art.

6.4.6. Optimal Design

MOS switches consume less ohmic power with higher widths (lower on resistance) and higher gate-charge power with higher widths (higher gate capacitance), so the total losses are lowest at the width that balances the two losses (when their first derivatives match), as shown in Fig. 6-12. For switched-inductors, since fewer coils in an inductor reduce inductance, which in turn increases current, and reduce resistance when constrained to small dimensions (3 x 3 x 1.5 mm^3), the switched-inductor are optimized by finding the inductance that induces the least total losses. This optimization process and application to piezoelectric chargers is new to the state of the art.

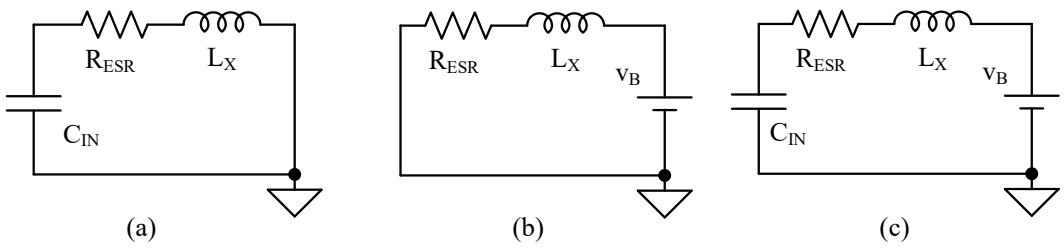

Figure 6-11. Circuit configuration for (a) indirect LC transfer, (b) indirect battery transfer, and (c) direct transfer.

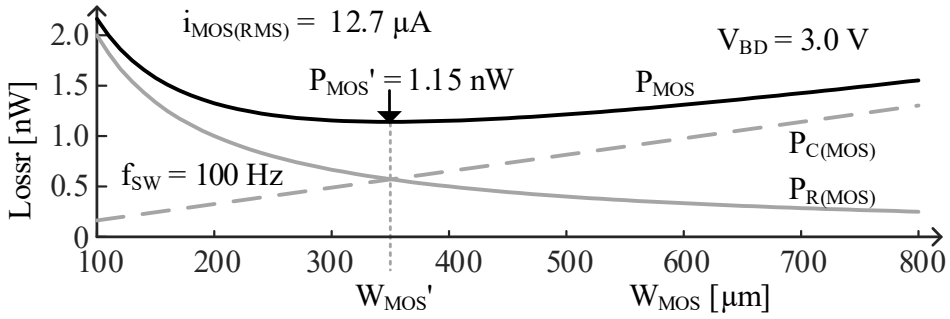

Figure 6-12. Optimization for a MOSFET switch.

6.4.7. Series Switched-Inductor Prototype

The prototype utilizes the conclusions that symmetrical discharges are better than asymmetrical discharges and that direct transfers are superior to indirect transfers, and follows the optimal design procedure to further the state of the art. The inductor L_X in Fig. 6-13 collects all the charge from C_{PZ} between half cycles, and directly pre-charges C_{PZ} in the opposite direction while charging the battery. The operation of the charger to pre-charge symmetrically is new to the state of the art, and can output 6.8× higher power than an ideal bridge can draw. However, the breakdown voltage limits the operation range, and the charger cannot handle vibrations that generates an open-circuit voltage higher than the breakdown voltage.

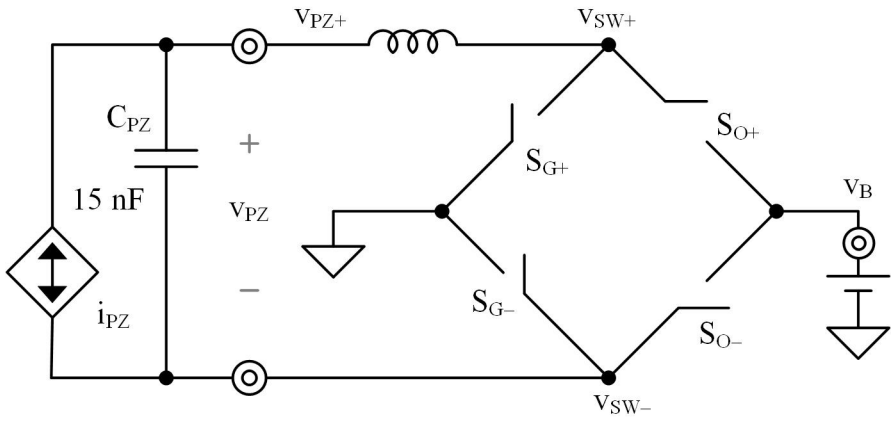

Figure 6-13. Schematic of series switched-inductor prototype.

6.4.8. Recycling Switched-Inductor Prototype

The prototype utilizes the conclusions that symmetrical discharges are better than asymmetrical discharges and that direct transfers are superior to indirect transfers, and follows the optimal design procedure to further the state of the art. Furthermore, the charger keeps piezoelectric voltage at the maximum power point throughout the half cycles with one inductor. The inductor L_X in Fig. 6-14 draws a portion of the energy from the piezoelectric capacitor to charge the battery whenever the piezoelectric voltage reaches the breakdown voltage, so that it can handle a vibration that generates higher open-circuit voltages than the breakdown limit. The same L_X collects all the charge from C_{PZ}, and recycles it back to C_{PZ} in the opposite direction between half cycles. The switches are controlled to maintain operation as well as tracking maximum power point. The only state of the art that can output the same output power requires 2 inductors with 2 stages [142], [144], or do not have a maximum power point tracking capability to output maximum power across a wide input range [145]–[148].

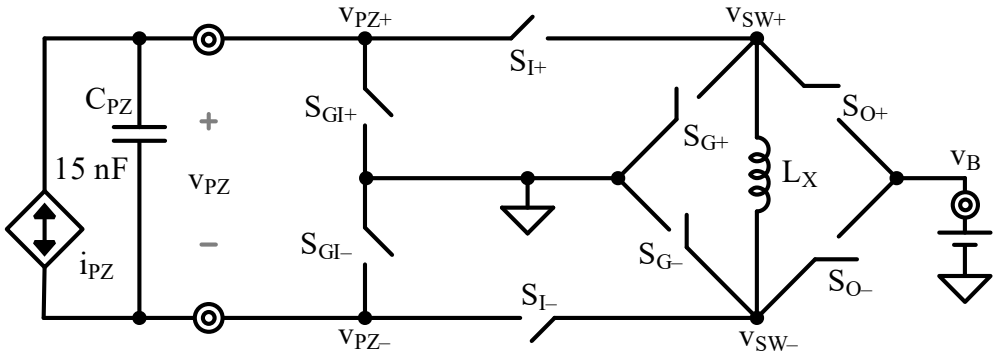

Figure 6-14. Schematics of recycling switched-inductor prototype.

6.4.9. Practical Applications

The basic concepts developed in this research to increase drawn power and reduce losses for piezoelectric energy-harvesting chargers can provide more output power to the battery to prolong lifetime and expand functionality for wireless microsystems. The embedded microsensors can collect information about their surrounding environment to save money in an industrial setting [15]–[18] or in a farm [16], [37]. The medical implants [23]–[25] can function for longer period to save lives. The proposed research can also be used to charge mobile electronics like cell phones, smart watches, or ear phones.

The two chargers that this research proposed, designed, built, and assessed, are tested with centimetre scale piezoelectric transducers that are commercially available, but the features can be migrated into a completely integrated millimetre scale package. This research can therefore be picked up by a future project that has already developed and tested a MEMS transducer, but would need a charger to maximize the power to charge the battery. Alternately, a power electronics engineer could look to build a MEMS device best

suited for the current charger, to complete a fully integrated solution for the wireless microsystems.

6.5. **Conclusions**

Piezoelectric transducers have separate positive and negative charger centers, which creates charge at their surface when under stress or strain. The charger would alternate if the transducer is under vibration, and piezoelectric chargers can collect the charge to transduce the kinect energy into electric domain. This research examines the drawn power and ohmic loss with respect of damping symmetry, and compares the ohmic loss between indirect transfers and direct transfers.

Symmetrical pre-charging chargers can draw more power than asymmetrical counterparts when the breakdown voltage only limits the peak voltage. Moreover, because symmetrical pre-charging recycles the energy at the end of a half cycle to pre-charge in the next half cycle, instead of getting assistance from the battery, it has lower ohmic loss. On the other hand, direct transfers allow the inductor to transfer more energy than it carries, therefore reducing transfer time and inductor current, and as a result, it has lower ohmic loss. Therefore, symmetrical pre-charging with direct transfers is the best synchronous discharges.

An optimally designed symmetrical pre-charging power stage that utilizes direct transfers with symmetrical pre-charging is proposed, designed, tested, and assessed. A second piezoelectric power stage, the recycling switched inductor bridge, is also proposed, designed, tested, and assessed. The recycling operation allows the charger to draw the maximum power possible from the transducer. The switched-inductor that charges the

battery allows the one-stage power stage to maintain maximum power-point across the range of the battery voltage. As a result, it outperforms all the state of the art, outputting 12× power compared with the maximum drawn power of the ideal diode bridge, and can output up to 76% of the theoretical maximum power a piezoelectric transducer can draw under breakdown limit. Although there is still room for improvement, i.e. integrated maximum power-point controller, cold start capability, and integrated piezoelectric charger system, this research makes the ultimate goal of powering wireless microsystems that save energy, money, and lives closer to reality.

REFERENCES

[1] R.J.M. Vullers, R. van Schaijk, H.J. Visser, J. Penders, and C. Van Hoof, "Energy harvesting for autonomous wireless sensor networks," *IEEE Solid-State Circuits Magazine*, vol. 2, issue 2, pp. 29–38, 2010.

[2] F. Goodarzy, E. Skafidas, and S. Bambini, "Feasibility of energy-autonomous wireless microsensors for biomedical applications: powering and communication," *IEEE Reviews in Biomedical Engineering*, vol. 8, pp. 17–29, August 2015.

[3] M. Belleville, H. Fanet, P. Fiorini, P. Nicole, M.J.M. Pelgrom, C. Piguet, R. Hahm, C. Van Hoof, R. Vullers, M. Tartagni, and E. Cantatore, "Energy autonomous sensor systems: towards a ubiquitous sensor technology," *Microelectronics Journal*, vol. 41, pp. 740–745, February 2010.

[4] D. Puccinelli and M. Haenggi, "Wireless sensor networks: applications and challenges of ubiquitous sensing," *IEEE Circuits and Systems Magazine*, vol. 3, no. 3, pp. 19–29, 2005.

[5] S Sudevalayam and P. Kulkarni, "Energy harvesting Sensor Nodes: Survey and Implications," *IEEE Communications Surveys & Tutorials*, vol. 13, no. 3, pp. 443-461, Third Quarter 2011.

[6] S. Mahmud, S. Ahmed and K. Shikder, "A Smart Home Automation and Metering System using Internet of Things (IoT)," *2019 International Conference on Robotics,Electrical and Signal Processing Techniques (ICREST)*, Dhaka, Bangladesh, 2019, pp. 451-454.

[7] M. Khan, B. N. Silva and K. Han, "Internet of Things Based Energy Aware Smart Home Control System," *IEEE Access*, vol. 4, pp. 7556-7566, 2016.

[8] T. Islam, S. C. Mukhopadhyay and N. K. Suryadevara, "Smart Sensors and Internet of Things: A Postgraduate Paper," *IEEE Sensors Journal*, vol. 17, no. 3, pp. 577-584, Feb, 2017.

[9] M. Alaab, A.A. Zaidan, B.B. Zaidan, M.Talalb, and M.L.M. Kiahb, "A review of smart home applications based on Internet of Things," *Journal of Network and Computer Applications*, vol. 97, pp. 48-65, Nov. 2017.

[10] B. Li and J. Yu, "Research and application on the smart home based on component technologies and Internet of Things," *Procedia Engineering*, vol. 15, pp. 2087-2092, 2011.

[11] A. Pantelopoulos and N. G. Bourbakis, "A Survey on Wearable Sensor-Based Systems for Health Monitoring and Prognosis," *IEEE Transactions on Systems, Man, and Cybernetics, Part C (Applications and Reviews)*, vol. 40, no. 1, pp. 1-12, Jan. 2010.

[12] D. Raskovic, T. Martin, and E. Jovanov, "Medical monitoring applications for wearable computing," *Computer Journal*, vol. 47, pp. 495–504, Apr. 2004.

[13] M.C. Domingo, "An overview of the internet of things for people with disabilities," *Journal of Network and Computer Applications*, vol. 35, no. 2, pp. 584–596, 2012.

[14] H. Alemdar and C. Ersoy, "Wireless sensor networks for healthcare: A survey," *Computer Network*, vol. 54, no. 15, pp. 2688–2710, 2010.

[15] L.D. Xu, W. He and S. Li, "Internet of Things in Industries: A Survey," *IEEE Transactions on Industrial Informatics*, vol. 10, no. 4, pp. 2233-2243, Nov. 2014.

[16] Z. Pang, Q. Chen, and W. Han, "Value-centric design of the internet-of-things solution for food supply chain: Value creation, sensor portfolio and information fusion," *Inf Syst Front*, vol. 17, pp. 289–319 2015

[17] Y. C. Zhang and J. Yu, "A study on the fire IOT development strategy," *Procedia Engineering*, vol. 52, pp. 314–319, 2013.

[18] L. D. Xu, W. He and S. Li, "Internet of Things in Industries: A Survey," *IEEE Transactions on Industrial Informatics*, vol. 10, no. 4, pp. 2233-2243, Nov. 2014.

[19] B. Ahlgren, M. Hidell and E. C. Ngai, "Internet of Things for Smart Cities: Interoperability and Open Data," *IEEE Internet Computing,* vol. 20, no. 6, pp. 52-56, Nov.-Dec. 2016.

[20] S. M. R. Islam, D. Kwak, M. H. Kabir, M. Hossain and K. Kwak, “The Internet of Things for Health Care: A Comprehensive Survey,” *IEEE Access*, vol. 3, pp. 678-708, 2015

[21] J. Yoo, L. Yan, S. Lee, Y. Kim, and H.J. Yoo, “A 5.2 mW self-configured wearable body sensor network controller and a 12 μW wirelessly powered sensor for a continuous health monitoring system,” *IEEE Journal of Solid-State Circuits*, vol. 45, no. 1, pp. 178–188, Jan. 2010.

[22] L.S.Y. Wong, S. Hossain, A. Ta, J. Edvinsson, D.H. Rivas, and H. Nääs, “A very low-power CMOS mixed-signal IC for implantable pacemaker applications,” *IEEE Journal of Solid-State Circuits*, vol. 39, no. 12, pp. 2446–2456, Dec. 2004.

[23] A.C.R. Grayson et al., “A BioMEMS review: MEMS technology for physiologically integrated devices," *in Proceedings of the IEEE*, vol. 92, no. 1, pp. 6-21, Jan. 2004

[24] D.A. La Van, T. McGuire, and R. Langer, “Small-scale systems for in vivo drug delivery,” *Nature Biotechnology*, vol. 21, no. 10, pp. 1184–1191, Oct. 2003.

[25] S. Smith, T.B. Tang, J.G. Terry, J.T.M. Stevenson, B.W. Flynn, H.M. Reekie, A.F. Murray, A.M. Gundlach, D. Renshaw, B. Dhillon, A. Ohtori, Y. Inoue, and A.J. Walton, “Development of a miniaturised drug delivery system with wireless power transfer and communication,” *IET Nanobiotechnol*ogy, vol. 1, no. 5, pp. 80–86, 2007.

[26] A.C.R. Grayson, I.S. Choi, B.M. Tyler, P.P. Wang, H. Brem, M.J. Cima, and R. Langer, “Multi-pulse drug delivery from a resorbable polymeric microchip device,” *Nature Materials*, vol. 2, pp. 767–772, Nov. 2003.

[27] P. Castillejo, J.-F. Martinez, J. Rodriguez-Molina, and A. Cuerva, “Integration of wearable devices in a wireless sensor network for an e-health application,” IEEE Wireless Commun., vol. 20, no. 4, pp. 38-49, Aug. 2013.

[28] B. Tan and O. Tian, ``Short paper: Using BSN for tele-health application in upper limb rehabilitation," *in Proc. IEEE World Forum Internet Things (WF-IoT)*, Mar. 2014, pp. 169170.

[29] G. Yang, L. Xie, M. Mäntysalo, X. Zhou, Z. Pang, L.D. Xu, S. Kao-Walter, Q. Chen, and L.R. Zheng, “A health-IoT platform based on the integration of

intelligent packaging, unobtrusive bio-sensor, and intelligent medicine box," *IEEE Transactions on Industrial Information*, vol. 10, no. 4, pp. 2180–2191, Nov. 2014.

[30] M. Flatscher, M. Dielacher, T. Herndl, T. Lentsch, R. Matischek, J. Prainsack, W. Pribyl, H. Theuss, and W. Weber, "A bulk acoustic wave (BAW) based transceiver for an in-tire-pressure monitoring sensor node," *IEEE Journal of Solid-State Circuits*, vol. 45, no. 1, pp. 167–177, Jan. 2010.

[31] Q. Zhu, R. Wang, Q. Chen, Y. Liu, and W. Qin, "IoT gateway: Bridging wireless sensor networks into internet of things," *in Proc. IEEE/IFIP 8th International Conference on Embedded Ubiquitous Computer (EUC)*, Hong Kong, China, Dec. 11–13, 2010, pp. 347–352.

[32] F. Xia, "Wireless sensor technologies and applications," *Sensors*, vol. 9, no. 11, pp. 8824–8830, 2009.

[33] M. Zhao, J. Li and Y. Yang, "A Framework of Joint Mobile Energy Replenishment and Data Gathering in Wireless Rechargeable Sensor Networks," *IEEE Transactions on Mobile Computing*, vol. 13, no. 12, pp. 2689-2705, Dec. 2014.

[34] A. Pantelopoulos and N.G. Bourbakis, "A survey on wearable sensor-based systems for health monitoring and prognosis," *IEEE Transactions on Systems, Man, and Cybernetics, Part C (Applications and Reviews)*, vol. 40, no. 1, pp. 1-12, Jan. 2010.

[35] S. Jeong and W. J. Chappell, "A city-wide smart wireless sewer sensor network using parasitic slot array antennas," *IEEE Antennas and Wireless Propagation Letters*, vol. 9, pp. 760-763, 2010.

[36] H. Zhou, B. Liu, and D. Wang, "Design and research of urban intelligent transportation system based on the internet of things," *Communication Computer Information Science*, vol. 312, pp. 572–580, 2012.

[37] T. Wark, P. Corke, P. Sikka, L. Klingbeil, Y. Guo. C. Crossman, P. Valencia, D. Swain, and G. Bishop-Hurley, "Transforming Agriculture through Pervasive Wireless Sensor Networks," *IEEE Pervasive Computing*, vol. 6, no. 2, pp. 50-57, April-June 2007.

[38] R. Sahai, S. Avadhanula, R. Groff, E. Steltz, R. Wood, R.S. Fearing, "Towards a 3g crawling robot through the integration of microrobot technologies," *in*

Proceedings of IEEE International Conference on Robotics and Automation, pp. 296–302, May 2006.

[39] J.A. Paradiso and T. Starner, "Energy scavenging for mobile and wireless electronics," *IEEE Pervasive Computing*, vol. 4, no. 1, pp. 18–27, 2005.

[40] R.J.M. Vullers, R. van Schaijk, I. Doms, C. van Hoof, and R. Mertens, "Micropower energy harvesting," *Solid-State Electronics*, vol. 53, no. 7, pp. 684–693, July 2009.

[41] M. Fojtik, D. Kim, G. Chen, Y. Lin, D. Fick, J. Park, M. Seok, M. Chen, Z. Foo, D. Blaauw, and D. Sylvester, "A Millimeter-Scale Energy-Autonomous Sensor System With Stacked Battery and Solar Cells," *IEEE Journal of Solid-State Circuits*, vol. 48, no. 3, pp. 801–813, Mar. 2013.

[42] N.J. Guilar, T.J. Kleeburg, A. Chen, D.R. Yankelevich, and R. Amirtharajah, "Integrated solar energy harvesting and storage," *IEEE Transactions on Very Large Scale Integration (VLSI) Systems*, vol. 17, no. 5, pp.627–637, May 2009.

[43] S.P. Beeby, M.J. Tudor, and N.M. White, "Energy Harvesting Vibration Sources for Microsystem Applications," *Measurement Science Technology,* vol. 17, pp. R175–195, Dec. 2006.

[44] G. Zhou, L. Huang, W. Li, and Z. Zhu, "Harvesting Ambient Environmental Energy for Wireless Sensor Networks: A Survey," *Journal of Sensors*, pp. 815467–815486, 2014.

[45] A.M. Sodagar, G.E. Perlin, Y. Yao, K.D. Wise, and K. Najafi, "An implantable microsystem for wireless multi-channel cortical recording," *in Proceedings of TRANSDUCERS 2007 - 2007 International Solid-State Sensors, Actuators and Microsystems Conference*, Lyon, 2007, pp. 69-72.

[46] G.E. Perlin and K.D. Wise, "An ultra compact integrated front end for wireless neural recording microsystems," *Journal of Microelectromechanical Systems*, vol. 19, no. 6, pp. 1409-1421, Dec. 2010.

[47] P. Cong, W.H. Ko, and D.J. Young, "Wireless batteryless implantable blood pressure monitoring microsystem for small laboratory animals," *IEEE Sensors Journal*, vol. 10, no. 2, pp. 243-254, Feb. 2010.

[48] H.N. Schwerdt, F.A. Miranda and J. Chae, "A fully passive wireless backscattering neurorecording microsystem embedded in dispersive human-head phantom medium," *IEEE Electron Device Letters*, vol. 33, no. 6, pp. 908-910, June 2012.

[49] M.M. Ahmadi and G.A. Jullien, "A Wireless-Implantable Microsystem for Continuous Blood Glucose Monitoring," *IEEE Transactions on Biomedical Circuits and Systems*, vol. 3, no. 3, pp. 169-180, June 2009.

[50] A.M. Sodagar, "Implantable biomedical microsystems: a new graduate course in biomedical circuits and systems," *IEEE Transactions on Education*, vol. 57, no. 1, pp. 48-53, Feb. 2014.

[51] F. Carrara and G. Palmisano, "High-efficiency reconfigurable RF transmitter for wireless sensor network applications," *in Proceedings of 2010 IEEE Radio Frequency Integrated Circuits Symposium*, Anaheim, CA, pp. 179-182, 2010.

[52] M. Stoopman, K. Philips and W. A. Serdijn, "An RF-powered DLL-based 2.4-ghz transmitter for autonomous wireless sensor nodes," *IEEE Transactions on Microwave Theory and Techniques*, vol. 65, no. 7, pp. 2399-2408, July 2017

[53] H. Saghlatoon, R. Mirzavand, M. M. Honari and P. Mousavi, "Sensor antenna transmitter system for material detection in wireless-sensor-node applications," *IEEE Sensors Journal*, vol. 18, no. 21, pp. 8812-8819, Nov. 2018.

[54] S. Roundy, P.K. Wright, and J. Rabaey, "A study of low level vibrations as a power source for wireless sensor nodes," *Computer Communication*, vol. 26, pp. 1131–1144, 2003.

[55] G.J. Sheu, S.M. Yang, and T. Lee, "Development of a low frequency electrostatic comb-drive energy harvester compatible to SoC design by CMOS process", *Sensors and Actuators A: Physical*, vol. 167, no. 1, pp. 70–76, 2011.

[56] S. Meninger, J.O. Mur-Miranda, R. Amirtharajah, A. Chandrakasan, and J.H. Lang, "Vibration-to-electric energy conversion," *IEEE Transactions on Very Large Scale Integration (VLSI) Systems*, vol. 9, no. 1, pp. 64-76, Feb. 2001.

[57] B. C. Yen and J. H. Lang, "A variable-capacitance vibration-to-electric energy harvester," *IEEE Transactions on Circuits and Systems I: Regular Papers*, vol. 53, no. 2, pp. 288-295, Feb. 2006.

[58] P. Miao, P.D. Mitcheson, A.S. Holmes, E.M. Yeatman, T.C. Green, and B.H. Stark, "MEMS inertial power generators for biomedical applications," *Microsystems Technology, vol. 12*, no. 10–11, pp. 1079–1083, Sept. 2006.

[59] M.E. Kiziroglou, C. He, and E.M. Yeatman, "Flexible substrate electrostatic energy harvester," *Electronic Letters*, vol. 46, no. 2, pp. 166–167, Jan. 2010.

[60] E.O. Torres and G.A. Rincón-Mora, "Self-tuning electrostatic energy-harvester," *IEEE Transactions on Circuits and Systems. II: Express Briefs*, vol. 57, no. 10, pp. 808–812, Oct. 2010.

[61] G. Despesse, J.J. Chaillout, T. Jager, F. Cardot, and A. Hoogerwerf, "Innovative structure for mechanical energy scavenging," *in Proceedings of International Conference on Solid-State Sensors, Actuators and Microsystems*, pp. 895–898, 2007.

[62] B. Bieske, G. Kropp and A. Rolapp, "Testing electrostatic energy harvesters: A new topology for accurate characterization," *in Proceedings of 2017 14th International Multi-Conference on Systems, Signals & Devices (SSD)*, Marrakech, 2017, pp. 331-336.

[63] A. Khaligh, P. Zeng and C. Zheng, "Kinetic energy harvesting using piezoelectric and electromagnetic technologies—state of the art," *IEEE Transactions on Industrial Electronics*, vol. 57, no. 3, pp. 850-860, March 2010.

[64] F. Khan, F. Sassani, and B. Stoeber, "Copper foil-type vibration-based electromagnetic energy harvester," *J. Micromechanical Microengineering*., vol. 20, pp. 125006-1–10, Nov. 2010.

[65] E.P. James, M.J. Tudor, S.P. Beeby, N.R. Harris, P. Glynne-Jones, J.N. Ross, and N.M. White, "An investigation of self-powered systems for condition monitoring applications," *Sensors and Actuators A: Physical,* vol. 110, pp. 171–176, Feb. 2004.

[66] Y. Tsunoda et al., "A small-size energy-harvesting electric power sensor for implementing existing electrical appliances into HEMS," *IEEE Sensors Journal*, vol. 16, no. 2, pp. 457-463, Jan.15, 2016.

[67] X. Liu, J. Qiu, H. Chen, X. Xu, Y. Wen, and P. Li, "Design and optimization of an electromagnetic vibration energy harvester using dual Halbach Arrays," *IEEE Transactions on Magnetics*, vol. 51, no. 11, pp. 1-4, Nov. 2015,

[68] Y. Sang, X. Huang, H. Liu, and P. Jin, "A vibration-based hybrid energy harvester for wireless sensor systems," *IEEE Transactions on Magnetics*, vol. 48, no. 11, pp. 4495-4498, Nov. 2012.

[69] S. Chamanian, S. Baghaee, H. Uluşan, Ö. Zorlu, E. Uysal-Biyikoglu and H. Külah, "Implementation of energy-neutral operation on vibration energy harvesting WSN," *IEEE Sensors Journal*, vol. 19, no. 8, pp. 3092-3099, April, 2019.

[70] D. Maurath, P. F. Becker, D. Spreemann and Y. Manoli, "Efficient energy harvesting with electromagnetic energy transducers using active low-voltage rectification and maximum power point tracking," *IEEE Journal of Solid-State Circuits*, vol. 47, no. 6, pp. 1369-1380, June 2012.

[71] K.A. Cook-Chennault, N. Thambi, and A.M. Sastry, "Powering MEMS portable devices– a review of non-regenerative and regenerative power supply systems with special emphasis on piezoelectric harvesting systems," *Smart Materials and Structures*, vol. 17, no. 4, p. 043001–043033, Aug. 2008.

[72] N.M. White, P. Glynne-Jones, and S.P. Beeby, "A novel thick-film piezoelectric micro-generator," *Smart Materials and Structures*, vol. 10, no. 4, pp. 850–852, Aug. 2001.

[73] A. Hajati and S.G. Kim, "Ultra-wide bandwidth piezoelectric energy harvesting," *Applied Physics Letter*, vol. 99, pp. 083105-1–3, Aug. 2011.

[74] E. Lee, J. Park, M. Yim, Y. Kim, and G. Yoona, "Characteristics of piezoelectric ZnO/AlN−stacked flexible nanogenerators for energy harvesting applications", *Applied Physics Letter*, vol. 106, pp. 023901, Jan. 2015.

[75] X. Lu, L. Hou, L. Zhang, G. Zhao, and Z.Y. Cheng, "Piezoelectric-excited membrane for liquids viscosity and mass density measurement", *Sensors and Actuators A: Physical*, vol. 261, pp. 196–201, July 2017.

[76] R. Ding, H. Liu, X. Zhang, J. Xiao, R. Kishor, H. Sun, B. Zhu, G. Chen, F. Gao, X. Feng, J. Chen, X. Chen, X. Sun, and Y. Zheng, "Flexible piezoelectric nanocomposite generators based on Formamidinium lead Halide Perovskite

nanoparticles," *Advanced Functional Materials*, vol. 26, no. 42, pp. 7708–7716, Nov. 2016.

[77] I. Jung, Y. Shin, S. Kim, J. Choi, and C. Kang, "Flexible piezoelectric polymer-based energy harvesting system for roadway applications," *Applied Energy*, vol. 197, pp. 222–229, July 2017.

[78] X.Y. Jiang, H.X. Zou, and W.M. Zhang, "Design and analysis of a multi-step piezoelectric energy harvester using buckled beam driven by magnetic excitation," *Energy Conversion and Management*, vol. 145, pp. 129–137, Aug. 2017.

[79] M.K. Gupta, J. Aneesh, R. Yadav, K.V. Adarsh, and S.W. Kim, "Highly efficient flexible piezoelectric nanogenerator and femtosecond two-photon absorption properties of nonlinear lithium niobate nanowires," *Journal of Applied Physics*, vol. 121, no. 17, pp. 175103-1–7, Apr. 2017.

[80] D. Yang, Y. Qiu, T. Wang, W. Song, Z. Wang, J. Xu, Q. Feng, Y. Zong, X. Sun, "Growth of 3D branched ZnO nanowire for DC-type piezoelectric nanogenerators," *Journal of Material Science Materials in Electronics*, vol. 27, no. 7, pp. 6708–6712, Mar. 2017.

[81] G. Szarka and B. Stark, "Review of Power Conditioning for Kinetic Energy Harvesting Systems," *IEEE Transactions on Power Electronics*, vol. 27, no. 2, pp. 803–815, 2012.

[82] A. Toprak and O. Tigli, "MEMS scale PVDF-TRFE-based piezoelectric energy harvesters," *Journal of Microelectromechanical Systems*, vol. 24, no. 6, pp. 1989-1997, Dec. 2015.

[83] K. Prashanthi, M. Naresh, V. Seena, T. Thundat, and V.R. Rao, "A novel photoplastic piezoelectric nanocomposite for MEMS applications," *Journal of Microelectromechanical Systems*, vol. 21, no. 2, pp. 259-261, Apr. 2012.

[84] N.G. Elvin, N. Lajnef, and A.A. Elvin, "Feasibility of structural monitoring with vibration powered sensors," *Smart Material Structures*, vol. 15, pp. 977–986, 2006.

[85] P. Glynn-Jones, S.P. Beeby, and N.M. White, "Towards a piezoelectric vibration-powered microgenerator," in *IEE Proceedings - Science, Measurement and Technology*, vol. 148, no. 2, pp. 68–72, Mar. 2001.

[86] H. Campanella, C. J. Camargo, J. Lopez Garcia, A. Daza, R. Urquiza and J. Esteve, "Thin-film piezoelectric MEMS transducer suitable for middle-ear audio prostheses," *Journal of Microelectromechanical Systems*, vol. 21, no. 6, pp. 1452-1463, Dec. 2012.

[87] O.M. Barham, M. Mirzaeimoghri, and D.L. DeVoe, "Piezoelectric disc transformer modeling utilizing extended Hamilton's principle*," IEEE Transactions on Power Electronics*, vol. 34, no. 7, pp. 6583-6592, July 2019.

[88] H.B. Fang, J.Q. Liu, Z.Y. Xu, L. Dong, L. Wang, D. Chen, B.C. Cai, and Y. Liu, "Fabrication and performance of MEMS-based piezoelectric power generator for vibration energy harvesting," *Microelectronics Journal*, vol. 37, pp. 1280–1284, 2006.

[89] J. C. Park, J. Y. Park and Y. Lee, "Modeling and characterization of piezoelectric d33-mode MEMS energy harvester," *Journal of Microelectromechanical Systems*, vol. 19, no. 5, pp. 1215-1222, Oct. 2010.

[90] T. Wang, R. Sawada, and C. Lee, "A piezoelectric micromachined ultrasonic transducer using piston-like membrane motion," *IEEE Electron Device Letters*, vol. 36, no. 9, pp. 957-959, Sept. 2015.

[91] M. Marzencki, Y. Ammar, and S. Basrour, "Integrated power harvesting system including a MEMS generator and a power management circuit," *in Proceedings of IEEE International Solid-State Sensors, Actuators, and Microsystems Conference*, pp. 887–890, June 2007.

[92] M. Marzencki, Y. Ammar, and S. Basrour, "Integrated power harvesting system including a MEMS generator and a power management circuit," *Sensors and Actuators A: Physical*, vol. 145-146, no. 1-2, pp. 363–370, July/Aug. 2008.

[93] B.-S. Lee, S.-C Lin, and W.-J. Wu, "Comparison of the piezoelectric MEMS generators with interdigital electrodes and laminated electrodes," *in Proceedings of SPIE-The International Society for Optical Engineering*, pp. 69331B-1–69331B-8, Mar. 2008.

[94] J. Lu, T. Sagawa. L. Zhang, H. Takagi, D.F. Wang, T. Itoh, and R. Maeda, "Piezoelectric MEMS devices and its application as bio-chemical sensors," *in Proceedings of the 8th Annual IEEE International Conference on Nano/Micro Engineered and Molecular Systems*, pp. 163-166, Suzhou, China, 2013.

[95] J. Lu, Y. Zhang, T. Itoh, and R. Maeda, "Design, fabrication, and integration of piezoelectric MEMS devices for applications in wireless sensor network," *in Proceedings of 2011 Symposium on Design, Test, Integration & Packaging of MEMS/MOEMS (DTIP),* Aix-en-Provence, 2011, pp. 217-221.

[96] S. Saadon and Y. Wahab, "From ambient vibrations to green energy source: MEMS piezoelectric energy harvester for low frequency application," *in Proceedings of 2015 IEEE Student Symposium in Biomedical Engineering & Sciences (ISSBES)*, pp. 59-63, Shah Alam, 2015.

[97] M. Renaud, K. Karakaya, T. Sterken, P. Fiorini, C. Van Hoof, and R. Puers, "Fabrication, modelling and characterization of MEMS piezoelectric vibration harvesters," *Sensors and Actuators A: Physical*, vol. 145–146, pp. 380–386, July-Aug. 2008.

[98] Y.B. Jeon, R. Sood, J.-h. Jeong, and S.-G. Kim, "MEMS power generator with transverse mode thin film PZT," *Sensors and Actuators A: Physical*, vol. 122, pp. 16–22, Feb. 2005.

[99] Lijun Gao, Shengyi Liu and R.A. Dougal, "Dynamic lithium-ion battery model for system simulation," *IEEE Transactions on Components and Packaging Technologies*, vol. 25, no. 3, pp. 495-505, Sept. 2002.

[100] Min Chen and G. A. Rincon-Mora, "Accurate electrical battery model capable of predicting runtime and I-V performance," *IEEE Transactions on Energy Conversion*, vol. 21, no. 2, pp. 504-511, June 2006.

[101] I. Shown, A. Ganguly, L.C. Chen, and K.H. Chen, "Conducting polymer-based flexible supercapacitor," *Energy Science and Engineering*, vol. 3, no. 1, pp. 2–26, January 2015.

[102] F. Baronti, G. Fantechi, R. Roncella, and R. Saletti, "High-efficiency digitally controlled charge equalizer for series-connected cells based on switching converter and super-capacitor," *IEEE Transactions on Industrial Informatics*, vol. 9, no. 2, pp. 1139-1147, May 2013.

[103] S. Buller, E. Karden, D. Kok and R. W. De Doncker, "Modeling the dynamic behavior of supercapacitors using impedance spectroscopy," *IEEE Transactions on Industry Applications*, vol. 38, no. 6, pp. 1622-1626, Nov.-Dec. 2002.

[104] E. Frackowiak, "Carbon materials for supercapacitor application," *Physical Chemistry Chemical Physics*, vol. 15, pp. 1774–1785, Mar. 2007.

[105] Y. Wang, Z. Shi, Y. Huang, Y. Ma, C. Wang, M. Chen, and Y. Chen, "Supercapacitor Devices Based on Graphene Materials," *Journal of Physical Chemistry*, vol. 113, no. 30, pp. 13103–13107, July 2009.

[106] D. P. Dubal, O. Ayyad, V. Ruiz, and P. Gómez-Romero, "Hybrid energy storage: the merging of battery and supercapacitor chemistries," *Chemical Society Reviews*, vol. 7, pp. 1777 – 1790, Jan. 2015.

[107] J. Li, F. Li, Z. Xu, and S. Zhang, "Multilayer lead-free ceramic capacitors with ultrahigh energy density and efficiency," Advanced Materials, vol. 30, no. 32, pp. 1802155. Aug. 2018.

[108] G.K. Ottman, H.F. Hofmann, A.C. Bhatt, and G.A. Lesieutre, "Adaptive piezoelectric energy harvesting circuit for wireless remote power supply," *IEEE Transactions on Power Electronics*, vol. 17, no. 5, pp. 669–676, Sept. 2002.

[109] L. Chao, C.Y. Tsui, and W.H. Ki, "A batteryless vibration-based energy harvesting system for ultra low power ubiquitous applications," *in Proceedings of IEEE International Symposium of Circuits and Systems*, pp. 1349–1352, 2007.

[110] L. Chao, C.Y. Tsui, and W.H. Ki, "Vibration energy scavenging system with maximum power tracking for micropower applications," *IEEE Transactions on Very Large Scale Integration (VLSI) Systems*, vol. 19, no. 11, pp. 2109–2119, Nov. 2011.

[111] T. Hehn, F. Hagedorn, D. Maurath, D. Marinkovic, I. Kuehne, A. Frey, and Y. Manoli, "A fully autonomous integrated interface circuit for piezoelectric harvesters," *IEEE Journal on Solid-State Circuits*, vol. 47, no. 9, pp. 2185–2198, Sep. 2012.

[112] J. Sankman and D. Ma, "A 12-μW to 1.1-mW AIM Piezoelectric Energy Harvester for Time-Varying Vibrations With 450-nA IQ," *IEEE Transactions on Power Electronics*, vol. 30, no. 2, pp. 632-643, Feb. 2015.

[113] K. A. Singh, R. Kumar and R. J. Weber, "A Broadband Bistable Piezoelectric Energy Harvester With Nonlinear High-Power Extraction," *IEEE Transactions on Power Electronics*, vol. 30, no. 12, pp. 6763-6774, Dec. 2015.

[114] Y. Liu, G. Tian, Y. Wang, J. Lin, Q. Zhang, and H.F. Hofmann, "Active piezoelectric energy harvesting: general principle and experimental demonstration," *Journal of Intelligent Material Systems and Structures*, vol. 20, no. 5, pp. 575–585, May 2009.

[115] Y. Sun, N.H. Hieu, C.-J. Jeong, and S.-G. Lee, "An integrated high-performance active rectifier for piezoelectric vibration energy harvesting system," *IEEE Transactions on Power Electronics*, vol. 27, no. 2, pp. 623–627, Feb. 2012.

[116] P. Midya, K. Haddad, and M. Miller, "Buck or boost tracking power converter," *IEEE Power Electronics Letters*, vol. 2, no. 4, pp. 131-134, Dec. 2004.

[117] P. Liu and C. Chang, "CCM noninverting buck–boost converter with fast duty-cycle calculation control for line transient improvement," *IEEE Transactions on Power Electronics*, vol. 33, no. 6, pp. 5097-5107, June 2018.

[118] A.A. Blanco and G.A. Rincón-Mora, "Compact fast-waking light/heat-harvesting 0.18- um cmos switched-inductor charger*," IEEE Transactions on Circuits and Systems I: Regular Papers*, vol. 65, no. 6, pp. 2024-2034, June 2018.

[119] K. K. Afridi, M. Chen, and D. J. Perreault, "Enhanced Bipolar Stacked Switched Capacitor Energy Buffers," *IEEE Transactions on Industry Applications*, vol. 50, no. 2, pp. 1141-1149, March-April 2014.

[120] S. Ben-Yaakov, "On the influence of switch resistances on switched-capacitor converter losses," *IEEE Transactions on Industrial Electronics*, vol. 59, no. 1, pp. 638-640, Jan. 2012.

[121] C. Peters, J. Handwerker, F. Henrici, M. Ortmanns, and Y. Manoli, "Experimental results on power efficient single-poly floating gate rectifiers," *IEEE International Symposium on Circuits and Systems*, pp. 1097–1100, Taipei, May 2009.

[122] T. Umeda, H. Yoshida, S. Sekine, Y. Fujita, T. Suzuki, and S. Otaka, "A 950-MHz rectifier circuit for sensor network tags with 10-m distance," *IEEE Journal Solid-State Circuits*, vol. 41, no. 1, pp. 35–41, Jan. 2006.

[123] S. Guo and H. Lee, "An efficiency-enhanced CMOS rectifier with unbalanced-biased comparators for transcutaneous-powered high-current implants," *IEEE Journal Solid-State Circuits*, vol. 44, no. 6, pp. 1796–1804, June 2009.

[124] O. Lazaro and G.A. Rincón-Mora, "180-nm CMOS wideband capacitor-free inductively coupled power receiver and charger," *IEEE Journal Solid-State Circuits*, vol. 48, no. 11, pp. 2839–2849, Nov. 2013.

[125] G.K. Ottman, H.F. Hofmann, and G.A. Lesieutre, "Optimized piezoelectric energy harvesting circuit using step-down converter in discontinuous conduction mode," *IEEE Transactions on Power Electronics*, vol. 18, no. 2, pp. 696–703, Mar. 2003.

[126] A. Tabesh and L.C. Grechette, "A Low-Power Stand-Alone Adaptive Circuit for Harvesting Energy from a Piezoelectric Micropower Generator," *IEEE Transactions on Industrial Electronics*, vol. 57, no. 3, pp. 840–849, Mar. 2010.

[127] T.T. Le, J. Han, A. Von Jouanne, K. Mayaram, and T.S. Fiez, "Piezoelectric micro-power generation interface circuits," *IEEE Journal Solid-State Circuits*, vol. 41, no. 6, pp. 1411–1420, Jun. 2006.

[128] H. Lee and M. Ghovanloo, "An adaptive reconfigurable active voltage doubler/rectifier for extended-range inductive power transmission," *IEEE Transactions on Circuits and Systems II: Express Briefs*, vol. 59, no. 8, pp. 481-485, Aug. 2012, doi: 10.1109/TCSII.2012.2204840.

[129] D. Kwon and G.A. Rincón-Mora, "A 2-um BiCMOS Rectifier-Free AC-DC Piezoelectric Energy Harvester-Charger IC," *IEEE Transactions on Biomedical Circuits Systems*, vol. 4, no. 6, pp.400–409, Dec. 2010.

[130] I.M. Darmayuda, Y. Gao, M.T. Tan, S.J. Cheng, Y. Zheng, M. Je, and C.H. Heng, "A Self-Powered Power Conditioning IC for Piezoelectric Energy Harvesting from Short-Duration Vibrations", *IEEE Trans. Circuits Syst. II, Exp. Briefs*, vol. 59, no. 9, pp. 578–582, Sep. 2012.

[131] D. Kwon, G.A. Rincón-Mora, and E.O. Torres, "Harvesting Ambient Kinetic Energy with Switched-Inductor Converters," *IEEE Trans. on Circuits and Systems I*, vol. 58, no. 7, pp. 1551–1560, July 2011.

[132] L. Wu, X. Do, S. Lee, and D.S. Ha, "A self-powered and optimal SSHI circuit integrated with an active rectifier for piezoelectric energy harvesting," *IEEE Transactions on Circuits and Systems I: Regular Papers*, vol. 64, no. 3, pp. 537-549, March 2017.

[133] S. Yang and G.A. Rincón-Mora, "Energy harvesting piezoelectric-powered CMOS switched-inductor bridge," *IEEE Transactions on Power Electronics*, vol. 34, no. 7, pp. 6489–6497, July 2019.

[134] J. Dicken, P.D. Mitcheson, I. Stoianov, and E.M. Yeatman, "Increased power output from piezoelectric energy harvesters by pre-biasing," in *Proc. PowerMEMS*, pp. 75–78, Dec. 2009.

[135] J. Dicken, P.D. Mitcheson, I. Stoianov, and E.M. Yearman, "Power-extraction circuits for piezoelectric energy harvesters in miniature and low-power applications," *IEEE Trans. on Power Electronics*, vol. 27, no. 11, pp. 4514–4529, Nov. 2012.

[136] S. Lu, F. Boussaid, "A highly efficient P-SSHI rectifier for piezoelectri energy harvesting," *IEEE Transactions on Power Electronics*, vol. 30, no. 10, pp. 5364–5369, Oct. 2015.

[137] M. Renaud, K. Karakaya, T. Sterken, P. Fiorini, C. Van Hoof, and R. Puers, "Fabrication, modelling and characterization of MEMS piezoelectric vibration harvesters," *Sensors and Actuators A: Physical*, vol. 145–146, pp. 380–386, July-Aug. 2008.

[138] K.S. Yoon, S.W. Hong, and G.H. Cho, "Double pile-up resonance energy harvesting circuit for piezoelectric and thermoelectric materials," *IEEE Journal of Solid-State Circuits*, vol. 53, no. 4, pp. 1049–1060, Apr. 2018.

[139] G.A. Rincón-Mora and S. Yang, "Tiny piezoelectric harvesters: Principles, constraints, and power conversion," *IEEE Transactions on Circuits and Systems I: Regular Papers*, vol. 63, no. 5, pp. 639–649, May 2016.

[140] D. Kwon and G.A. Rincón-Mora, "A single-Inductor 0.35 um CMOS Energy-Investing Piezoelectric Harvester," *IEEE Journal Solid-State Circuits*, vol. 49, no. 10, Oct. 2014.

[141] E. Lefeuvre, A. Badel, C. Richard, L. Petit, and D. Guyomar, "A comparison between several vibration-powered piezoelectric generators for standalone systems," *Sensors Actuators A*, vol. 126, pp. 405–416, 2006.

[142] A. Badel, A. Benayad, E. Lefeuvre, L. Lebrun, C. Richard, and D. Guyomar, "Single crystals and nonlinear process for outstanding vibration-powered electrical

generators," *IEEE Transactions on Ultrasonics, Ferroelectronics, and Frequency Control*, vol. 53, no. 4, pp. 673–684, Apr. 2006.

[143] D. Guyomar, G. Sebald, S. Pruvost, and M. Lallart, "Energy harvesting from ambient vibrations and heat," *Journal of Intelligent Material Systems and Structures*, vol. 20, pp. 609–624, Mar. 2009.

[144] Y.K. Ramadass and A.P. Chandrakasan, "An efficient piezoelectric energy harvesting interface circuit using a bias-flip rectifier and shared inductor," *IEEE Journal Solid-State Circuits*, vol. 45, no. 1, pp. 189–204, Jan. 2010.

[145] S. Du, Y. Jia, C.D. Do, and A.A. Seshia, "An efficient SSHI interface with increased input range for piezoelectric energy harvesting under variable conditions," *IEEE Journal Solid-State Circuits*, vol. 51, no. 11, pp. 2729–2742, Nov. 2016.

[146] D.A. Sanchez, J. Leicht, F. Hagedorn, E. Jodka, E. Fazel, and Y. Manoli, "A parallel-SSHI rectifier for piezoelectric energy harvesting of periodic and shock excitations," *IEEE J. Solid-State Circuits*, vol. 51, no. 12, pp. 2867–2879, Dec. 2016.

[147] S. Javvaji, V. Singhal, V. Menezes, R. Chauhan, and Shanthi Pavan, "Analysis and design of a multi-step bias-flip rectifier for piezoelectric energy harvesting," *IEEE J. Solid-State Circuits*, vol. 54, no. 9, pp. 2590–2600, Sept. 2019.

[148] S. Du, Y. Jia, C. Zhao, G.A.J. Amararunta, and A.A. Seshia, "A nail-size piezoelectric energy harvesting system integrating a MEMS transducer and a CMOS SSHI circuit," *IEEE Sensor Journal*, vol. 20, no. 1, pp. 277–285, Jan. 2020.

[149] S. Li, A. Roy, and B.H. Calhoun, "A piezoelectric energy-harvesting system with parallel-SSHI rectifier and integrated maximum-power-point tracking," *IEEE Solid-State Circuit Letters.*, vol. 2, no. 12, pp. 301–304, Dec. 2019.

[150] A. M. Eltamaly and K. E. Addoweesh, "A Novel Self-Power SSHI Circuit for Piezoelectric Energy Harvester," in IEEE Transactions on Power Electronics, vol. 32, no. 10, pp. 7663-7673, Oct. 2017.

[151] S. Yang and G.A. Rincón-Mora, "Least lossy piezoelectric energy-harvesting charger," *in Proceedings of 2019 IEEE 62nd International Midwest Symposium on Circuits and Systems (MWSCAS)*, Dallas, TX, USA, 2019, pp. 275-278.

[152] X. Xiao, X. Huang and Q. Kang, “A hill-climbing-method-based maximum-power-point-tracking strategy for direct-drive wave energy converters,” *IEEE Transactions on Industrial Electronics*, vol. 63, no. 1, pp. 257-267, Jan. 2016.

[153] J. K. Udavalakshmi and M. S. Sheik, “Comparative study of perturb & observe and look-up table maximum power point tracking techniques using MATLABISimulink,” *in Proceedings of 2018 International Conference on Current Trends towards Converging Technologies (ICCTCT)*, Coimbatore, 2018, pp. 1-5.

[154] S.Du, G.A.J. Amaratunga, and A.A. Seshia, “A Cold-Startup SSHI Rectifier for Piezoelectric Energy Harvesters With Increased Open-Circuit Voltage,” *IEEE Transactions on Power Electronics*, vol. 34, no. 1, pp. 263-274, Jan. 2019.

[155] A. A. Blanco and G. A. Rincón-Mora, "Energy-harvesting microsensors: Low-energy task schedule & fast drought-recovery design," *in Proceedings of 2016 IEEE 59th International Midwest Symposium on Circuits and Systems (MWSCAS)*, Abu Dhabi, 2016, pp. 1-4.

[156] E. Blokhina, A. El Aroudi, E. Alarcon, and D. Galayko, “Nonlinearity in Energy Harvesting Systems: Micro- and Nanoscale Applications,” Springer, 2016.

[157] J. Dicken, P. D. Mitcheson, I. Stoianov, and Eric M. Yeatman, “Power-extraction circuits for piezoelectric energyharvesters in miniature and low-power applications,” *IEEE Transactions on Power Electronics*, vol. 27, no. 11, pp. 4514–4539, Nov. 2012.

[158] Y.C. Shu and I.C. Chen, “Analysis of power output for piezoelectric energy harvesting systems,” Smart Materials and Structures, vol. 15, no. 6, pp. 1499–1512, December 2006.

VITA

Siyu Yang

Siyu Yang received his Bachelor of Science degree from Tsinghua University, Beijing, China, in 2013. He has been pursuing a Ph. D degree at Georgia Institute of Technology since August, 2013, and he joined Georgia Tech Analog, Power, and Energy IC's Lab under the guidance of Professor Gabriel A. Rincón-Mora in January, 2015. He completed an internship with Texas Instruments in Dallas, Texas, from May to August in 2018. He is now working full time as a Sr. PMIC Engineer at Samsung Semiconductor Inc. in San Jose, California.